GEOMETRIC PHASE IN QUANTUM COMPUTATION

by

JT Thomas
A Dissertation
Submitted to the
Graduate Faculty
of
George Mason University
in Partial Fulfillment of
The Requirements for the Degree
of
Doctor of Philosophy
Physics

Committee:

	Dr. Ming Tian, Dissertation Director
	Dr. Neil Goldman, Committee Member
	Dr. Marco Lanzagorta, Committee Member
	Dr. Erhai Zhao, Committee Member
	Dr. Maria Dworzecka, Acting Department Chair
	Dr. Donna M. Fox, Associate Dean, Office of Student Affairs & Special Programs, College of Science
	Dr. Peggy Agouris, Dean, College of Science
Date: 4-15-2016	Spring Semester 2016 George Mason University Fairfax, VA

Geometric Phase in Quantum Computation

A Dissertation submitted in partial fulfillment of the requirements for the degree of Doctor of Philosophy at George Mason University

by

JT Thomas
Master of Science
George Mason University, 1996

Director: Ming Tian, Professor
Department of Physics

Spring Semester 2016
George Mason University
Fairfax, VA

DEDICATION

This is dedicated to my family: Anne Thomas, C.E. Sandy Thomas, and Sandy R. Thomas.

ACKNOWLEDGEMENTS

I would like to thank all my teachers and professors for helping me to learn this material; my advisor Dr. Ming Tian for guiding and assisting me in my research over several years; committee members for teaching me in their courses and guiding me while on this committee; Fenwick Library staff and Ms. Sally Evans for much assistance on this manuscript; our program director, Dr. Paul So for keeping me on track to graduation; my son Sandy for sharing his computer expertise; group members Dr. Karen Sauer, Dr. David Prescott, Colin Cattanach, Devin Vega and Pamela Rambow for many discussions; my fellow students/physicists Dr. Tanu Luke, Dr. Mahmoud Lababidi and many others for their assistance; and friends and family for all their sacrifice, support and encouragement during this dissertation work.

TABLE OF CONTENTS

LIST OF TABLES

LIST OF FIGURES

LIST OF ABBREVIATIONS AND SYMBOLS

AA ... Aharonov-Anandan phase
DP ... dynamic phase
GP ... geometric phase
H ... Hamiltonian
n_1 ... first rotation axis
n_{E1} ... first endpoint
NMR ... nuclear magnetic resonance
QC ... quantum computation
QD ... quantum dot
QED ... cavity quantum electrodynamics
SQUID ... superconducting quantum interference device
TP ... total phase
U ... unitary operator (rotation matrix)
x ... axis along first endpoint
x,y,z ... lab frame coordinates
x' ... axis bisecting the segment's associated geodesic
y' ... rotation axis of geodesic
β_1 ... angle amount of first segment on great circle (or associated geodesic)
β_1' ... angle amount of first segment off great circle
β_2 ... angle amount of geodesic associated with second segment
β_2' ... angle amount of second segment
Δ ... detuning
Θ ... solid angle
θ_L ... laser phase in lab frame
τ ... time duration of the rotation
φ_1 ... angle of first rotation axis from x'-axis
φ_2 ... angle of second rotation axis from x'-axis
ψ ... qubit wavefunction
Ω ... Rabi vector
Ω_0 ... Rabi frequency

ABSTRACT

GEOMETRIC PHASE IN QUANTUM COMPUTATION

JT Thomas, Ph.D.

George Mason University, 2016

Dissertation Director: Dr. Ming Tian

A fundamental challenge of quantum computation is being able to scale up a large number of high fidelity quantum gates while noise and error are affecting the gate's physical control parameters. This dissertation focuses on the fidelity of single-qubit quantum gates constructed by a change in quantum geometric phase, while the control parameters are affected by random noise and systematic error. A unified model of geometric quantum computation is developed, in which a qubit state is controlled by a composite Hamiltonian, resulting in a multiple-segment rotation of the quantum state and allowing characterization of evolution paths depending on the associated geometric and dynamic phase. The fidelity of the quantum gates in the presence of different noise error is compared for purely geometric, hybrid (having both geometric and dynamic phase), and conventional dynamic quantum gates built on single Hamiltonians. Results showed hybrid quantum gates had the highest fidelities, followed by geometric gates, and conventional dynamic gates had the lowest fidelities. In addition, there was indication in

some cases higher fidelities result from gates created from a larger number of segments in the quantum state rotation. These results can be understood by the relation of the control parameters with the evolution path geometry. By translating between control parameters, our model can be applied to different systems for quantum computation, including: the laser manipulation of a two-level atom, laser manipulation of trapped ions, nuclear magnetic resonance, polarization states of photons, superconducting qubits in cavity QED, and quantum dots.

CHAPTER 1- INTRODUCTION

Quantum computation enables exponentially faster algorithms than classical computation, however, the fundamental challenge is being able to scale up. This includes the ability to perform a large number of high fidelity quantum gate operations within the coherence time of the qubit state, while noise is affecting the gate's physical control parameters. This dissertation focuses on the fidelity of quantum gates constructed by a change in quantum geometric phase, while the control parameters are affected by random and systematic noise.

1.1 Geometric quantum gates

Standard dynamic quantum gates are constructed by a control Hamiltonian driving evolution of the qubit state. The performance of such a gate depends on both the Hamiltonian and the evolution path, which is highly susceptible to noise affecting the control Hamiltonian. An alternative approach is to utilize the change of quantum geometric phase in a qubit state, which depends only on the area subtended by the evolution path on the Bloch sphere (Figure 1), and is therefore suspected to naturally be less affected by certain types of noise.

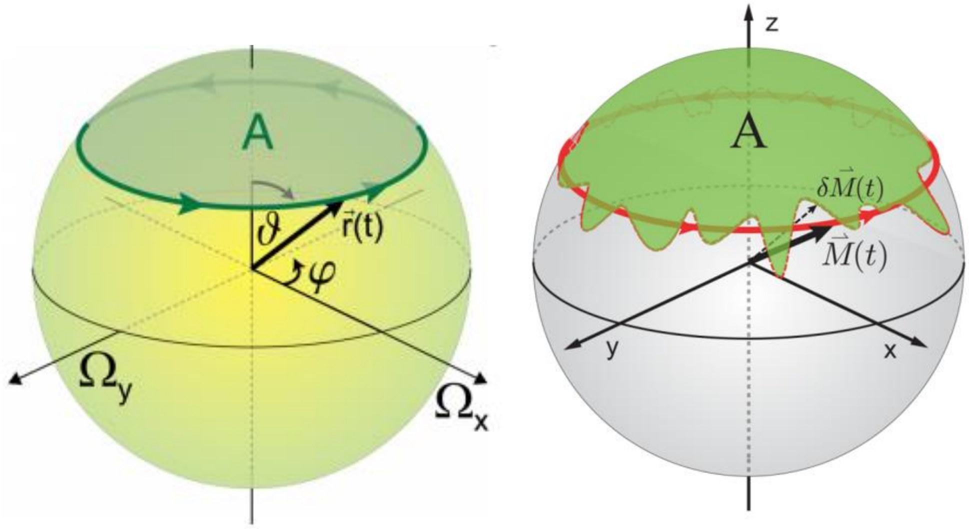

Figure 1- A quantum gate based on geometric phase: a) the geometric phase of the gate depends only on the area A subtended by the evolution path; b) noise affecting the evolution path causes it to jitter, but the area A should be preserved (from Filipp 2014).

The use of geometric phase change in specially designed Hamiltonians for quantum gates has been researched in most major physical qubit systems, including solid state atoms, nuclear magnetic resonance (NMR) systems, optical systems, trapped ions/atoms, quantum dots, and superconducting qubits. However, there is a lack of either experimental or theoretical proof of performance improvements in using geometric gates instead of dynamics gates in the presence of noise. In order to solve this problem, a systematic study of all possible geometric evolution paths and gate-driving Hamiltonians is needed.

One complication to this study is that a geometric path is usually driven by a composite Hamiltonian, which means searching a parameter space much larger than that of a single Hamiltonian. Research specific to the six physical systems listed above has also generated system-specific control parameters and formalism to describe geometric gates and qubit evolution paths, making it difficult to study the intrinsic common properties of the geometric phase in different quantum systems. The unified model presented here focuses on these common geometric phase properties that are the foundation for design, analysis, and optimization of geometric quantum gates.

The main objective of this dissertation is to develop a unified theoretical model for quantum state manipulation in any general 2-level qubit through parametrization of general driving Hamiltonians and their associated evolution operators. This model can be used in designing and analyzing a set of universal quantum gates that are sufficient for quantum computation. These quantum gates and their characteristics apply to any two-level qubit systems.

Importance of the problem

This thesis focuses on three important aspects of the unified formalism for geometric phase and geometric quantum computing (GQC): the fundamental study of quantum physics; design of a quantum gate for GQC; and evaluation of robustness of gates and improvement of gate performance.

Geometric phase is a general property of the evolution of quantum systems. A unified formalism allows different physical systems to be analyzed on the same platform. The common properties of the quantum state evolution and the driving Hamiltonian can be summarized while the differences between the systems can be compared. The evolution of any 2-level system can be described by a vector evolving in a 2-dimensional Hilbert space (Bloch or Poincare sphere). The Hamiltonian can be defined by control parameters that drive the state vector's evolution.

Based on understanding of the state evolution, the quantum gate for a certain manipulation of the qubit can be designed using the control parameters in the Hamiltonian. A set of universal gates and the corresponding driving Hamiltonians will be designed by purely geometric phase change. A unified formalism will meet the need to quickly translate between the variables of the different systems so that the existing designs and experimental implementations in different types of qubits will be analyzed and used to develop efficient robust quantum gates that are applicable in other qubit systems.

Different qubit systems used in GQC should share some common advantages based on intrinsic fault tolerance that results from the global nature of geometric phase. However, some quantum gates may work better in certain systems due to the different realization of the driving Hamiltonian with system-specified physical variables. A unified formalism will make it possible to compare the differences between systems and find the advantages and disadvantages of particular systems for geometric quantum computation. With a unified formalism, a generalized design and optimization can be more quickly applied to various qubit systems.

An additional aspect of our study involved composite paths that were hybrid (part dynamic, part geometric). Besides studying the unique property of geometric paths, our model also allows us to explore these hybrid paths and their associated quantum gates.

1.2 Overview of the field

Our main thesis is the question of whether geometric gates have higher fidelity under environmental noise than standard dynamic or hybrid gates; we also compare whether composite rotation gates have higher fidelity than the standard direct, single rotation gates. It is often stated in the literature that quantum gates built on geometric phase are not as sensitive to random noise, since the gate depends only on the solid angle subtended by the evolution path on the Bloch sphere, which should remain roughly the same. However, this assumption has not yet been proven.

Zhu –Zanardi work.

Zhu-Zanardi (ZZ) (2005) gives support for the above assumption of geometric quantum gates, by finding higher fidelities on geometric gates than dynamic gates, when control parameters were varied to evolve between the two different types of gates. In the ZZ scheme, a single completed loop direct rotation is made (see section 2.8 for definition of direct rotations). The ZZ paths are a special (1-segment) case of our N-segments (composite rotations) work.

ZZ use an NMR Hamiltonian:

$$\boldsymbol{H} = \frac{\mathbf{1}}{\mathbf{2}}(\boldsymbol{\omega_0}\mathbf{cos}\,\boldsymbol{\omega}\,\boldsymbol{\sigma_x} + \boldsymbol{\omega_0}\mathbf{sin}\,\boldsymbol{\omega}\ \ \boldsymbol{\sigma_y} + \boldsymbol{\omega_1}\boldsymbol{\sigma_z})$$

where their control parameters are related to our model's lab frame control parameters $(\Omega_0,\ \varphi_L, \Delta)$ by:

$$\omega_0 = -\Omega_0, \quad \omega = \varphi_L\,, \quad \omega_1 = \Delta$$

The control parameters ω_0 and ω_1 are directly proportional to an external controllable rotating magnetic field B_0 and a constant magnetic field B_1 in the z-direction. ZZ apply a random percentage noise multiplying the control parameters ω_0 and ω_1.

Blais-Tremblay

On the other hand, Blais-Tremblay (2003) provide evidence against the assumption of greater fidelity with geometric quantum gates. However, in their work, the geometric gates are created by three-segment rotations and compared with the conventional dynamic gates created from just a single rotation. The first and last segments of the geometric gates are in the same direction, making this equivalent to a two-segment rotation if the same noise is put on these segments. The geometric gate paths are also restricted to lie on great circles, so that the hybrid paths (containing both geometric and dynamic phases) of our work are not considered.

ETH Zurich

The Quantum Device Lab at ETH Zurich have experimentally compared geometric gates based on Berry's phase (adiabatic, cyclic geometric phase) with dynamic gates and found an advantage to geometric gates (Berger 2013). The ETH Zurich team used a microwave-driven superconducting two-level qubit, with noise modeled by producing fluctuations of the control field. The noise-induced dephasing was measured with a geometric contribution that only depended on how much the noise distorted the path; the dynamic phase gates are path dependent and more affected by dephasing. In contrast to this work, our work uses nonadiabatic geometric phase.

1.3 Methods

Research method

The main problem of our research was formulating a unified formalism of geometric quantum computation on the Bloch sphere. This involved first studying each of the main 2-level systems used in GQC research, and finding the qubits, Hamiltonian, equation of motion, and control variables used in each system. A general notation of variables has been chosen from the Bloch equation. A table has been made to translate between this general formalism and the qubits, Hamiltonian, equation of motion, and control variables used in each of the GQC approaches.

Dynamic phase elimination

An important issue in the construction of geometric quantum gates is the elimination of the dynamic phase. This can be done in several ways, such as using the spin echo technique, which involves traversing the evolution in the opposite direction, so that the dynamic phases of the two segments cancel, whereas the geometric phases add. Another method of handling the dynamic phase is to use the "unconventional GQC" scheme (Zhu & Wang 2003), where instead of eliminating the dynamic phase, the dynamic phase is kept proportional to the geometric phase.

The focus of this thesis for elimination of the dynamic phase will be to use evolutions that stay on the great circles of the Bloch sphere. This has the advantage of using fewer rotations than the spin echo technique, and also seems to be the most straightforward realization of geometric quantum gates.

Construction of evolution paths

Our work first defined a generic two-level quantum particle as the physical qubit of the unified formalism. The generic control Hamiltonian was parameterized, so that it can be modeled as a dipole moment in an effective field. In the next step we designed cyclic paths for a universal set of single qubit quantum gates on the Bloch sphere. The idea is to specify a general cyclic path, so that by varying the control parameters, any geometric phase can result, and thus any single qubit quantum gate can be constructed. The next step of our study analyzed the fidelity of the gates against systematic and random errors in the control parameters. Using this study of the fidelity of the gates, the geometric paths were optimized for high fidelity gate operation. Finally, the general model has been applied to existing physical qubit systems, to specify and analyze the control parameters in each specific system.

N-segment method

We then extended our research to calculate the geometric and dynamic phases of 3, 4, 10 and N segments. We calculated the geometric phase for N segments by using the geometric phase formula for a spherical polygon and our 2-segment geometric phase equations for the wedge each segment makes with its associated geodesic. This also generalized our 2-segment rotations to rotation axes in any direction, by using the same wedges and associated geodesic, and setting the spherical polygon to 0. Finally, we calculated the dynamic phase for N segments by considering the general Hamiltonian for each segment rotation, and how it operates on the qubit state along the x-axis.

CHAPTER 2- QUBIT THEORY

2.1 Introduction

This chapter explains the basic qubit theory of quantum information underlying our work, including descriptions of qubit basis states, and how they are represented on the Bloch and Poincare spheres; Pauli spin matrices, and how they are used to build the evolution matrix and Hamiltonian H; and how the control parameters measured in the lab are used to design the Hamiltonians. We briefly discuss how a universal set of gates can be made. We show how this theory is applied to the notation of the 6 physical systems considered here. We present general formulas for calculating the geometric and dynamic phases of rotations, and use this to define direct and composite rotations, which are compared later in our work. We describe the way noise is put on the control parameters of the Hamiltonian, in order to measure the fidelity of our designed quantum gates. Finally, this chapter introduces the application of our model to several other physical systems.

2.2 Qubits on the Bloch sphere

A quantum state is completely defined (up to a global phase) by two angles: the polar angle α and the azimuth angle β (see Figure 2). From our orthogonal basis states, defined as:

$$|0> = \begin{pmatrix} 1 \\ 0 \end{pmatrix},\ |1> = \begin{pmatrix} 0 \\ 1 \end{pmatrix} \quad \textbf{(1)}$$

the most general qubit state can be written as a superposition:

$$|\psi> = \cos\frac{\alpha}{2}\ |0> \ + e^{i\beta}\sin\frac{\alpha}{2}\ \ |1> \tag{1}$$

or in matrix form

$$|\psi> = \begin{pmatrix} \cos\frac{\alpha}{2} \\ e^{i\beta}\sin\frac{\alpha}{2} \end{pmatrix} \tag{2}$$

The Bloch sphere is a two-dimensional unit sphere that represents all possible states $|\psi>$ of the qubit. The north and south poles of the Bloch sphere are taken to represent the orthogonal states $|0>$ and $|1>$ respectively (for example, spin up and spin down states); these usually form the computational basis states. Any two vectors pointing in opposite directions represent a pair of orthogonal basis states; for example,

$$|\psi> = \frac{1}{\sqrt{2}}(|0> +|1>) \tag{4}$$

pointing along the positive x-axis, and

$$|\psi> = \frac{1}{\sqrt{2}}(|0> -|1>) \tag{5}$$

along the negative x-axis. Each point on the Bloch sphere represents a distinct superposition of the computational basis states $|0>$ and $|1>$.

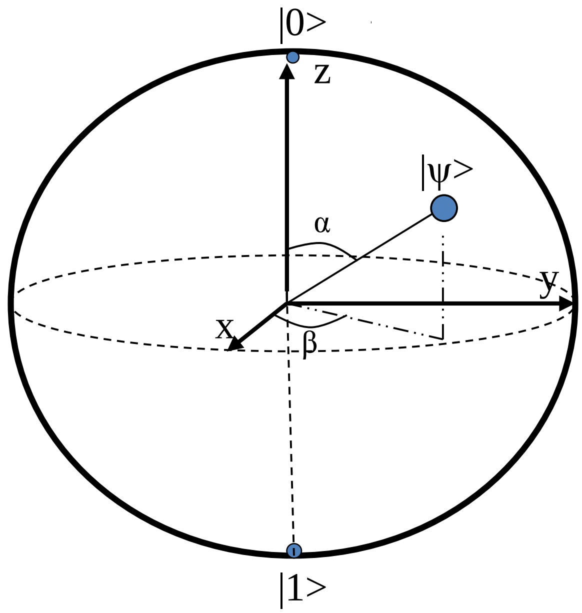

Figure 2- Bloch sphere with polar angle α and azimuth angle β locating the state (or Bloch vector) |ψ>.

The Bloch and Poincare spheres are similar, except that the poles of the Bloch sphere are represented by up and down states, whereas the Poincare sphere's poles are defined by right and left polarizations of light beams.

2.3 Quantum gates and Pauli matrices

A quantum gate acting on the qubit state of Figure 2 will cause it to rotate to another position on the Bloch sphere. For instance, the Pauli spin matrices operate on the qubit basis states (defined in equation 1) as follows:

$$\sigma_x|0> = |1>, \quad \sigma_y|0> = i|1>, \quad \sigma_z|0> = |0>$$

$$\sigma_x|1> = |0>, \quad \sigma_y|1> = -i|0>, \quad \sigma_z|1> = -|1> \qquad \textbf{(6)}$$

where

$$\sigma_x = \begin{pmatrix} 0 & 1 \\ 1 & 0 \end{pmatrix}, \quad \sigma_y = \begin{pmatrix} 0 & -i \\ i & 0 \end{pmatrix}, \quad \sigma_z = \begin{pmatrix} 1 & 0 \\ 0 & -1 \end{pmatrix} \qquad \textbf{(7)}$$

More complicated gates can be made from combinations of these Pauli matrices.

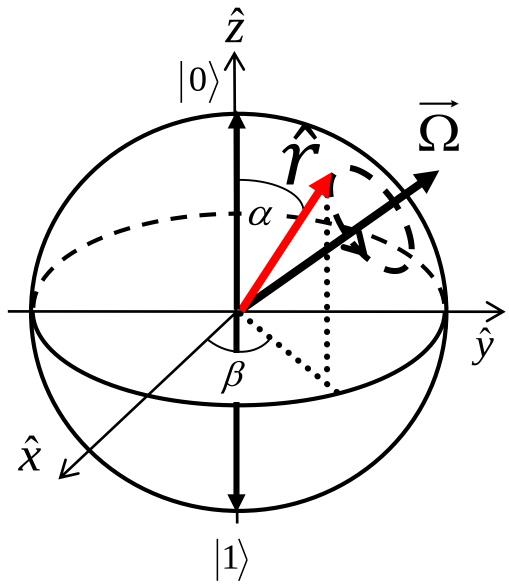

Figure 3- Rotation of Bloch vector $\hat{r}$ around the Rabi vector $\vec{\Omega}$ on the Bloch sphere.

A quantum gate can also be considered a rotation around a rotation axis (see Figure 3). The quantum state is represented by a Bloch vector $\vec{r}$ pointing to the position (θ,φ) on the Bloch sphere; during the operation of the quantum gate, this state is rotated around the Rabi vector $\vec{\Omega}$. In Cartesian coordinates, $\vec{r}$ is given by

$$\vec{r} = (\sin\theta\cos\varphi, \sin\theta\sin\varphi, \cos\theta) \quad \textbf{(8)}$$

The Bloch vector satisfies the Bloch equation:

$$\frac{d\vec{r}}{dt} = \vec{\Omega} \times \vec{r} \tag{9}$$

where the Rabi vector is $\vec{\Omega} = (-\Omega_0 \cos\varphi_L, -\Omega_0 \sin\varphi_L, \Delta)$, which is a function of the measurable control parameters Ω_0, φ_L, and Δ. For instance, in a 2-level atom, these control parameters are the Rabi frequency (Ω_0), phase of the laser (φ_L), and laser detuning (Δ).

2.4 Evolution operator

A quantum gate acting on a qubit changes the orientation of the Bloch vector of Figure 3. This is equivalent to a rotation around a given axis $\hat{n}$ by a given angle θ, made by a rotation operator U(θ,φ):

$$U = e^{i\alpha} R_n(\theta) = e^{i\alpha} \exp\left\{-i\frac{\theta}{2}\hat{n}\cdot\vec{\sigma}\right\} \tag{10}$$

$$= e^{i\alpha}\left[\cos\frac{\theta}{2} I - i\sin\frac{\theta}{2}(n_x\sigma_x + n_y\sigma_y + n_z\sigma_z)\right] \tag{11}$$

where $\hat{n} = (n_x, n_y, n_z)$ is the rotation axis, $\vec{\sigma} = (\sigma_x, \sigma_y, \sigma_z)$ are the Pauli matrices, I is the identity matrix, θ is the rotation angle, and α is any real number making up a global phase.

Any rotation around an arbitrary axis can be made by rotations around two non-parallel axes in the x-y plane, where the rotation axis is defined by angle φ in $\vec{n} = (\cos\varphi, \sin\varphi, 0)$. The operator simplifies to:

$$U(\theta,\varphi) = \cos\frac{\theta}{2} I - i \cdot \sin\frac{\theta}{2}\left(\cos\varphi\sigma_X + \sin\varphi\sigma_Y\right)$$
$$= \begin{pmatrix} \cos\frac{\theta}{2} & -ie^{-i\varphi}\sin\frac{\theta}{2} \\ -ie^{i\varphi}\sin\frac{\theta}{2} & \cos\frac{\theta}{2} \end{pmatrix} \quad \textbf{(12)}$$

These operators with controllable variables θ and φ are sufficient for achieving a universal set of single qubit gates.

The basic rotation operator can be made through pure geometric phase change. For a given pair of angles (θ,φ), eigenstates can be defined, such as:

$$\left|+\right\rangle_\varphi = \frac{1}{\sqrt{2}}\begin{pmatrix} 1 \\ e^{i\varphi} \end{pmatrix}, \qquad \left|-\right\rangle_\varphi = \frac{1}{\sqrt{2}}\begin{pmatrix} 1 \\ -e^{i\varphi} \end{pmatrix} \quad \textbf{(13)}$$

which are represented by a pair of basis vectors parallel to the rotation axis (see Figure 4). The rotation operator drives the basis state $\left|+\right\rangle_\varphi$ around loop A. Every segment of the loop is on a geodesic and the solid angle enclosed by the loop is the desired rotation angle θ. The basis state $\left|+\right\rangle_\varphi$ gains a geometric phase $-\frac{\theta}{2}$ and turns into $e^{-i\theta/2}\left|+\right\rangle_\varphi$. The basis state $\left|-\right\rangle_\varphi$ with corresponding loop B is driven by the same rotation operator and gains an opposite phase to become $e^{i\theta/2}\left|-\right\rangle_\varphi$.

Under this operation a qubit in an arbitrary initial state $|\psi\rangle = \begin{pmatrix} c_0 \\ c_1 \end{pmatrix}$ turns into

$$\begin{pmatrix} \cos\frac{\theta}{2}c_1 - ie^{-i\varphi}\sin\frac{\theta}{2}c_0 \\ -ie^{i\varphi}\sin\frac{\theta}{2}c_1 + \cos\frac{\theta}{2}c_0 \end{pmatrix} \quad \textbf{(14)}$$

This is equivalent to applying a rotation operator in equation 12 to the initial state. On this geometric path the rotation operator is equivalent to

$$U(\theta,\varphi) = U(\pi/2, \varphi+\pi/2)U(-\pi, \varphi+\pi/2+\theta/2)U(\pi/2, \varphi+\pi/2) \quad \textbf{(15)}$$

where the three consecutive rotations on the right hand side are the geometric rotations.

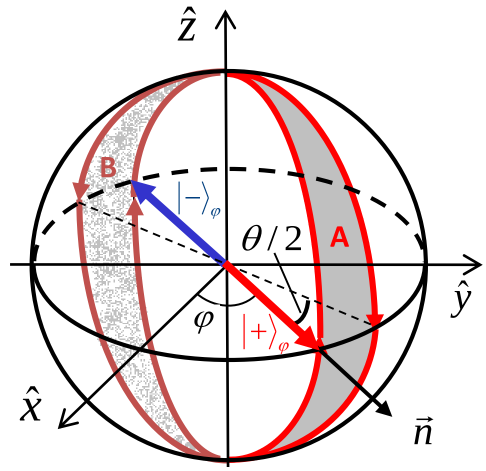

Figure 4- Effect of a geometric rotation U(θ,φ) on orthogonal states {|+>,|->}: |+> follows path A and |-> follows path B, with rotation angle θ and rotation axis $\hat{n}$.

2.5 Hamiltonian and control parameters

In order to design the rotation operator U, a Hamiltonian is first designed by choosing the values of the physical lab control parameters, which in the 2-level atom system are: Rabi frequency (Ω_0), laser phase (φ_L), and laser detuning (Δ). The most general Hamiltonian is:

$$H = \frac{1}{2}(-\Omega_0 \cos\varphi_L \sigma_x - \Omega_0 \sin\varphi_L \sigma_y + \Delta\sigma_z) = \frac{1}{2}\vec{\Omega}\cdot\vec{\sigma} \quad \textbf{(16)}$$

where the $\vec{\sigma}$ are the Pauli matrices. The Rabi vector $\vec{\Omega}$ determines the direction of the rotation axis by:

$$\hat{n} = \frac{\vec{\Omega}}{|\Omega_n|} = \frac{1}{|\Omega_n|}\{-\Omega_0 \cos\varphi_L, -\Omega_0 \sin\varphi_L, \Delta\} \tag{17}$$

where the Rabi vector amplitude is $|\Omega_n| = \sqrt{(\Omega_0)^2 + \Delta^2}$.

The rotation operator U is then derived from the Schrodinger equation:

$$i\hbar\frac{\partial\psi}{\partial t} = H\psi \tag{18}$$

Solving for the wavefunction, we have:

$$\psi(t) = e^{-\frac{i}{\hbar}H(t-t_0)}\psi_0 \tag{19}$$

Therefore the rotation operator is

$$U = e^{-\frac{i}{\hbar}H\tau} \tag{20}$$

where the Hamiltonian is constant over that segment. Setting $\tau = 1$ and $\hbar = 1$, each segment's rotation operator is

$$U = e^{-\frac{i}{2}\vec{\Omega}\cdot\vec{\sigma}} = e^{-\frac{i}{2}|\Omega|\hat{n}\cdot\vec{\sigma}}$$

The rotation angle β' is related to the rotation duration and the amplitude of the Rabi vector by:

$$\beta' = |\Omega|\tau \tag{21}$$

so that the rotation operator becomes:

$$U = \exp\left\{-i\,\frac{\beta'}{2}\bar{\sigma}\cdot\hat{n}\right\} \tag{22}$$

where β' is the angle amount of rotation around the $\hat{n}$-axis.

The control parameters defined by the Hamiltonian are varied in our work to design paths for rotations on the Bloch sphere, representing the operation of quantum gates. For a 2-segment rotation, our control parameters are the Rabi frequency Ω_0, the lab frame phase φ_L, and the detuning Δ of the first segment's Hamiltonian, and the rotated frame control parameter φ_2, which is the angle between the bisector of the geodesic between the two endpoints of the two segments and the second rotation axis. For N segments, there are 3N-2 control parameters to vary to create all possible paths.

2.6 Universal set of gates

A universal set of gates can be made from a single qubit gate capable of any phase, such as the single qubit rotation operator in equation 11, and an entangled two qubit gate such as a CNOT or a controlled phase gate (Ekert 2000). These two types of gates can be achieved through pure geometric phase change. Our work focuses on single qubit gates, but the methods can be extended to two qubit gates as in Zhu & Zanardi (2005).

For each of the different physical systems used to implement geometric quantum gates, the actual control parameters/physical variables are different. For instance, in NMR, the geometric quantum gates are controlled by the magnitude of the magnetic field; in quantum dots, one of the control parameters is the energy band gap. There are many other different physical variables that are used as control parameters, taking all the different physical systems into account.

2.7 Six physical systems for qubit construction

This section describes how the notations of the 6 physical systems under consideration here fit in with the theory described above. We first describe how the qubits are made in each system, what the control parameters are, and how they relate to the control parameters of our model.

Laser manipulation of two-level atom

The two-level atom consists of an atom with two energy levels. By using laser pulses, the state of the system can be put into a superposition of the ground and excited state.

Geometric quantum computation can be realized by using a two-level atom driven by a laser field (Tian 2004). In this system, the qubit

$$|\psi> = c_0|0> + c_1|1> \tag{23}$$

is formed with an atom by superimposing its two energy levels, a ground state $|0>$ and an excited state $|1>$. A laser tuned near the atomic resonant frequency manipulates the state of the atom. The control Hamiltonian for the driving laser pulse is

$$H = \hbar\begin{pmatrix} 0 & -\frac{\Omega_0}{2}e^{i\varphi} \\ -\frac{\Omega_0}{2}e^{-i\varphi} & 0 \end{pmatrix} \tag{24}$$

where Ω_0 is the Rabi frequency for an on-resonance laser, tuned in resonance with an atom of atomic resonant frequency ω_0; and φ is the phase of the laser, given by the laser electric field:

$$E(t) = \Omega_0(\omega_0\, t + \varphi) \tag{25}$$

From this an equation can be found that constrains the Rabi frequency, the laser phase, and the coefficients of the state vector.

The control parameters of this system are the Rabi vector **Ω**, consisting of a Rabi frequency Ω_0, the phase φ, and the frequency detuning Δ of the laser field. From the amplitude of the Rabi vector $\Omega = \sqrt{\Omega_0^2 + \Delta^2}$ and the time duration τ of the laser pulse, we can derive the pulse area, θ:

$$\theta = \Omega\, \tau \tag{26}$$

An operation on the Bloch sphere is then completely defined by the laser field. The geometric phase in this system can be observed using a stimulated photon echo pulse. Two driving pulses with a relative phase between them create a geometric phase that creates a phase shift on the photon echo pulse.

Laser manipulation of trapped ions

This section is similar to the previous, except the qubits are now formed from trapped ions. A proposal for using trapped ions is given by Duan(2001); see also Lemmer (2013).

In trapped ion systems, a set of ions is confined in a linear Pauli trap and manipulated by a laser. A scheme for nonadiabatic geometric quantum gates utilizing ion traps is described in Li & Cen (2003). The qubits are made from ions with two energy levels, |0> and |1>, separated by energy $\hbar\omega_0$. The laser field used to selectively address the states is given by $\mathbf{E}(\mathbf{z}) = \mathbf{E_0} \cos(\mathbf{k} \cdot \mathbf{z} - \omega_L t + \varphi)$, with wave vector **k**, the ion's center of mass coordinate **z**, laser frequency ω_L, and laser phase φ.

The Hamiltonian for a single qubit gate is

$$H = \tfrac{1}{2}\,\omega_0\,\sigma_z + \omega[\sigma^{+}\exp\{-i\omega_L t + i\varphi\} + \sigma^{-}\exp\{i\omega_L t - i\varphi\}] \quad \textbf{(27)}$$

where ω = Rabi frequency, and σ^{+} is defined as |0> <1| ; σ^{-} = |1> <0|; and σ_z = |1> <1| - |0> <0|. For two-qubit gates, there is an extra exponential term involving phonon creation/annihilation operators.

The Hamiltonian for each ion in the rotating frame (which has angular velocity $\omega_L \hat{e}_z$) is

$$H_R = \Omega \cdot \sigma \quad \textbf{(28)}$$

where $\sigma = \{\sigma_x, \sigma_y, \sigma_z\}$ are the Pauli matrices and the effective magnetic field is $\Omega = \{\omega \cos\varphi, \omega \sin\varphi, \tfrac{1}{2}(\omega_0 - \omega_L)\}$.

During operation of the one-qubit gate, the state is rotated around the effective magnetic field Ω. The state is kept perpendicular to Ω on the Bloch sphere, so that there is no dynamic phase.

As an example, a state initially in the |+> state (pointing along the y-axis on the Bloch sphere, to point A in Figure 5) is hit by a π-pulse with laser frequency φ set to 0, and effective magnetic field $\Omega_1 = (\omega, 0, \tfrac{1}{2}(\omega_0 - \omega_L))$. This causes the state to rotate to |-> (along the negative y-axis) to point B in Figure 5, along the path ACB. Another π-pulse hits the ion with laser frequency φ set to π, and effective magnetic field $\Omega_2 = (-\omega, 0, \tfrac{1}{2}(\omega_0 - \omega_L))$. This causes the state to rotate back to |+> along the path BDA.

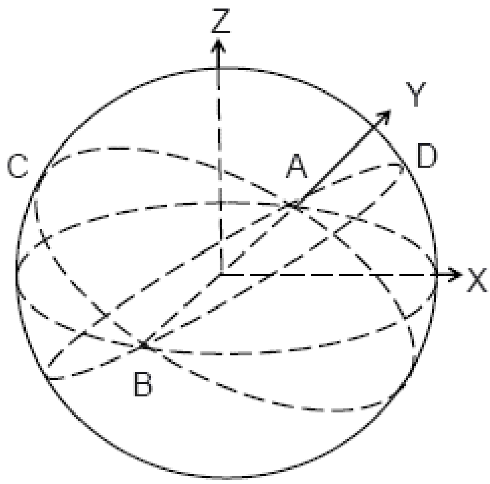

Figure 5- Evolution of the state vector on the Bloch sphere, keeping perpendicular to the effective magnetic field. From Li & Cen (2003).

After this cyclic evolution, the |+> state acquires a geometric phase factor of exp{iγ} while the |-> state acquires the geometric phase factor exp{-iγ}. The nonadiabatic (AA) phase is

$$\gamma = 4 \arctan [2\, \omega/(\omega_0 - \omega_L)] \tag{29}$$

Under this same gate, the states |0> and |1> rotate to

$$|0\rangle \rightarrow \cos\gamma|0\rangle + \sin\gamma|1\rangle$$

$$|1\rangle \rightarrow \cos\gamma|1\rangle - \sin\gamma|0\rangle \tag{30}$$

and any arbitrary single qubit rotation can be made with this gate.

Nuclear magnetic resonance

The qubits in nuclear magnetic resonance (NMR) are built from precessing spins in a rotating magnetic field. There is a constant magnetic field in the z direction which creates the split two energy levels, and defines the resonant frequency ω_0. Another magnetic field rotates in the x-y plane with frequency ω. At resonance, these two frequencies match.

The qubit in nuclear magnetic resonance (NMR) is built from the two spin states of a spin ½ particle, with spin the state |0> representing spin aligned with an external magnetic field, and |1> aligned against. The driving force is a rotating magnetic field in the x-y plane.

In nonadiabatic GQC in NMR, parameters are varied in the Hamiltonian instead of using rotating operations. The magnetic field is initially in the x-z plane, with polar angle θ, and rotates with frequency ω in the x-y plane. The Hamiltonian in this case is given by

$$\mathbf{12}(\boldsymbol{\omega 0 \cos \omega}\ \boldsymbol{\sigma x} + \boldsymbol{\omega 0 \sin \omega}\ \boldsymbol{\sigma y} + \boldsymbol{\omega 1 \sigma z}) \tag{31}$$

where the control parameters are related to our model by

$$\omega_0 = -\frac{g\mu B_0}{\hbar} = -\Omega_0, \quad \omega = \varphi_L, \quad \omega_1 = -\frac{g\mu B_1}{\hbar} = \Delta \tag{32}$$

and g is the gyromagnetic factor; μ is the Bohr magneton.

Photon polarization/optical systems

In optical systems, qubits are created from the polarization of photons. In an optical geometric phase experiment, unitary transformations are made on the polarization state of photons (Simon 1988). The polarization of a plane light wave in the z direction is determined by the complex-valued electric fields E_x and E_y, which form the polarization vector **E**. The ratio E_x/E_y gives the projection space of polarization states. This space is the same as S^2, the Poincare sphere (see Figure 6). The qubits for an optical geometric gate are made from superpositions of orthogonal polarization states.

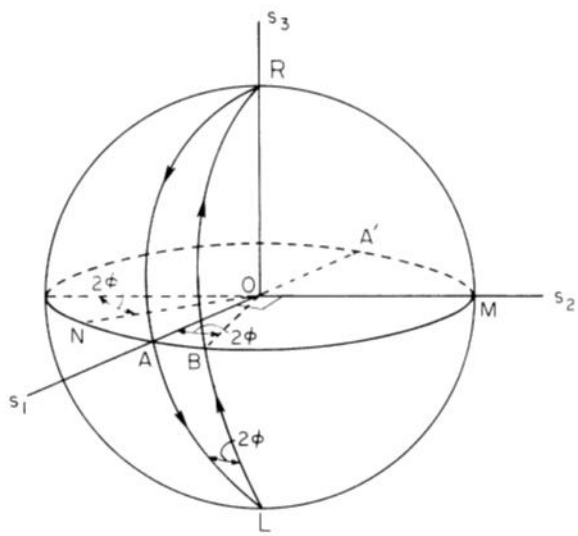

Figure 6- Polarization states on the Poincare sphere. (From Wang & Wu 2007).

The Poincare sphere contains all the possible polarization states. The poles represent the states R and L, for the right- and left- circularized polarization states. A and A' represent the linear x- and y- polarizations. The unitary transformations in this experiment are 2x2 matrices, acting as rotations on the Poincare sphere. Quarter-wave plates produce the rotations shown in Figure 6: the first $\pi/2$ rotation around the axis OM, and the second $\pi/2$ rotation around the axis ON.

The basic experimental setup is a Michelson interferometer. Light from one arm of the interferometer is used as a reference beam, to be recombined with light from the other arm where a geometric phase occurs by using quarter wave plates. In Figure 7, the geometric phase can be varied by rotating the second quarter wave plate (QWP2). The half wave plate HWP1 controls whether the incident beam is linearly polarized in the x- or y-directions.

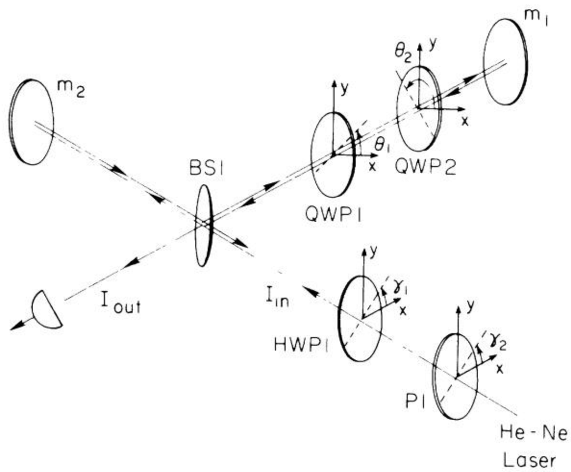

Figure 7- Experimental setup for observation of geometric phase in a Michelson interferometer. (From Wang & Wu 2007)

The circuit shown in Figure 6 is traversed as ALBRA, by making the first quarter wave plate (QWP1) in arm m1 with the slow axis fixed at $\theta = \pi/4$. After traversing QWP1, the light, which was linearly polarized in the x-direction (so that its state was at A on the Poincare sphere), is now left circularly polarized (at the point L on the Poincare sphere). The second quarter wave plate, QWP2, is set to the angle $\theta = 3\pi/4 + \varphi$, with respect to the x-axis. The light emerges from QWP2 at state B. It then hits the mirror and reflects back into QWP2 in the opposite direction, taking the state to R. After going through QWP1 again, it is back to state A.

The solid angle subtended by this circuit is 4φ, where 2φ is the angle between points A and B. The Berry phase, or Pancharatnam phase in this case, is ½ the solid angle, or equal to 2φ. The Berry phase is -2φ for y-direction linearly polarized incident light, and the circuit in Figure 6 is flipped to the opposite side of the Poincare sphere. The evolution of the polarization vector **E** is given by

$$\lambda \frac{dE}{dz} = iJ(z)E \tag{33}$$

where λ is the wavelength of the laser and J(z) is the evolution matrix:

$$J_{\theta}(z) = \begin{pmatrix} n+\varepsilon\cos 2\theta & \varepsilon\sin 2\theta \\ \varepsilon\sin 2\theta & n-\varepsilon\cos 2\theta \end{pmatrix} \tag{34}$$

The angle θ is the angle that the birefringent plate's slow axis makes with the x-axis, and n+ ε and n- ε are the refractive indices for the slow and fast axes. Equation 33 is similar to the Schrodinger equation, and the matrix J(z) is analogous to the Hamiltonian for this system.

The control parameters for the optical geometric phase of this system are the angle θ, set by QWP1; the orientation of HWP1 in determining the incident light beam polarization; the refractive indices of the birefringent plates (which can be controlled by the thickness of the plates); and the wavelength λ of the laser.

Other optical geometric quantum computer schemes include an optical holonomic quantum computer (Pachos 2000). This proposal uses quantum optics devices such as interferometers for two qubit interactions, and displacing and squeezing devices, which achieve the one qubit rotations. The degenerate space of the Hamiltonian eigenstates needed for the holonomic quantum computation scheme is constructed from two dimensional degenerate spaces of laser beams.

Superconducting qubits in cavity QED

This section describes the different superconducting qubits that can be created in cavity/circuit QED using Josephson tunnel junctions.

Geometric quantum gates have been proposed using superconducting phase qubits (Peng 2007). In this system, the qubit is formed from a Hamiltonian with 2 non-degenerate, orthogonal energy states. The Hamiltonian is a product of the Pauli spin matrices and the magnetic field B.

A superconducting Josephson junction nanocircuit has been proposed to observe adiabatic geometric phase in a 2-level system in the Falci scheme (Falci 2000). This scheme uses a Josephson junction nanocircuit made of a superconducting electron box formed by an asymmetric SQUID, with a magnetic flux Φ and applied gate voltage V_x.

For the Falci scheme, Josephson couplings E_{J1} and E_{J2} of the junctions are much smaller than the charging energy E_{ch}. The temperature is kept much smaller than the couplings. This is called the charging regime.

The Hamiltonian is

$$H(t) = E_{ch}(n - n_x)^2 - E_J(\Phi)\cos(\theta - \alpha) \quad \textbf{(35)}$$

where

$$E_J(\Phi) = \sqrt{(E_{J1} - E_{J2})^2 + 4E_{J1}E_{J2}\cos^2\left(\pi\frac{\Phi}{\Phi_0}\right)} \quad \textbf{(36)}$$

$$\tan\alpha = \frac{E_{J1} - E_{J2}}{E_{J1} + E_{J2}}\tan\left(\pi\frac{\Phi}{\Phi_0}\right) \quad \textbf{(37)}$$

and $\Phi_0 = \frac{h}{2e}$ is the superconducting quantum of flux; n is the number of Cooper pairs; θ is the phase difference across the junction. The phase shift α(Φ) can be controlled in the asymmetric SQUID. Other control parameters in the Hamiltonian are the applied gate voltage V_x, which controls the offset charge $2en_x$; and the magnetic flux Φ controls the coupling $E_J(\Phi)$.

The quantum gates of the Falci scheme are based on charge qubits. The two charge eigenstates n = 0, 1 create the basis {|0>,|1>}.

This system can be seen to be analogous to a spin in a magnetic field by using the effective Hamiltonian

$$H_B = -\frac{1}{2}B\cdot\sigma \quad \textbf{(38)}$$

where

$$B = (E_J\cos\alpha, -E_J\sin\alpha, E_{ch}(1-2n_x)) \quad \textbf{(39)}$$

and σ are the Pauli matrices. Charging the system causes it to be coupled to the effective magnetic field in the z direction. The Josephson junction coupling terms determine the projection on the x-y plane.

To execute the closed loop that produces the geometric phase, the parameters given by the applied gate voltage V_x and the magnetic flux Φ are varied. This drives the Hamiltonian H_B around a closed loop in the parameter space given by {B}. The geometric phase obtained is the Berry phase $\gamma_B(\Phi_{M,}\, n_{xm})$, proportional to the solid angle enclosed around the degeneracy B= 0. The offset charge n_x (proportional to the applied gate voltage V_x) is varied from n_{xm} to ½. The magnetic flux is varied from 0 to Φ. Varying these two parameters makes a closed loop in an n_x-Φ diagram: n_x is first varied from n_{xm} to 1/2, while keeping Φ at 0; then Φ is varied from 0 to Φ_M, while keeping n_x at ½; n_x is then varied back to n_{xm} while keeping Φ constant. The circuit is then completed by taking Φ back to 0, while keeping n_x constant.

Quantum dots

Quantum dots are made of semiconductor nanocrystals, which can be entangled to form qubits. Voltages applied to the leads of quantum dots controls the number of electrons in the quantum dot. Quantum information is stored in the spin states of single-electron quantum dots (Kloeffel & Loss, 2012).

Quantum dots are another candidate for geometric quantum computation (Pei 2010). In quantum dot gates, small voltages are applied to the leads, so that the current through the quantum dot is controlled. There can also be optical control of the quantum dot, in which an oscillating magnetic field is generated by radio-frequency pulses. This enables measurements of a single electron’s spin.

The rotation angle of the geometric rotation in this system depends on the ratio of the Rabi frequency to the detuning. When this ratio goes to infinity, then the rotation angle is π, and there is no dynamical phase contribution for this geometric rotation. Other rotation angles lead to both a dynamical phase and a geometric phase.

One approach of nonadiabatic geometric quantum computation using quantum dots is given by the Yang-Zhu-Wang (YZW) scheme (Kai-Yu 2003). N quantum dots are irradiated by laser light, with charges on each dot. An exciton can be produced by a dot, and there can be interdot exchange of excitons. A qubit is made from the basis states {|0>,|1>}, where |0> is the state without an exciton, and |1> is the single exciton state. For a single qubit gate, the Hamiltonian consists of creation (and annihilation) operators for electrons $c_i^+(c_i)$ and holes $h_i^+(h_i)$:

$$H(t) = \frac{\varepsilon}{2}\sum_{i=1}^{N}\left(c_i^+ c_i - h_i h_i^+\right) + E(t)\sum_{i=1}^{N}\left(c_i^+ h_i^+\right) + E^*(t)\sum_{i=1}^{N}\left(h_i c_i\right) \qquad \textbf{(40)}$$

where ε is the energy band gap of the semiconductor dot, E(t) is the laser shape , and N is the number of quantum dots.

This Hamiltonian can be written in terms of quasi-spin operators J, by making the definitions $J_{i+} = c_i^+ h_i^+$, $J_{i-} = h_i c_i$, $J_{iZ} = \frac{1}{2}\left(c_i^+ c_i - h_i h_i^+\right)$:

$$H(t) = \varepsilon J_Z + E(t) J_+ + E^*(t) J_- \qquad \textbf{(41)}$$

for a single quantum dot.

The incident laser pulse shape E(t) is given in terms of amplitude A and frequency ω : E(t) = A exp(iωt). The single qubit Hamiltonian becomes a function of this amplitude A and frequency ω, the energy band gap ε of the semiconductor dots, and a set of X,Y,Z quasi-Pauli operators:

$$H(t) = \frac{\varepsilon}{2} Z + A\cos(\omega t) X + A\sin(\omega t) Y \qquad \textbf{(42)}$$

where {X = $J_+ + J_-$, Y = i(-$J_+ + J_{-}$), Z = 2 J_z}.

On the unit Bloch sphere, the incident laser pulse is the rotation field, and the semiconductor energy gap is the constant z-direction field. Two orthogonal states $|\psi_{\pm}>$ evolve cyclically, and are a function of just the three parameters: laser amplitude A, laser frequency ω, and energy band gap ε. These three parameters are combined into the symbol

$$\chi = \text{atan}\ (2A/(\varepsilon-\omega)) \tag{43}$$

so that the two orthogonal states become:

$$\begin{aligned} |\psi_+ > &= \cos\frac{\chi}{2}|0> + \sin\frac{\chi}{2}|1> \\ |\psi_- > &= -\sin\frac{\chi}{2}|0> + \cos\frac{\chi}{2}|1> \end{aligned} \tag{44}$$

The evolution operator acting on the two orthogonal states is

$$U(\tau)|\psi_{\pm}> = e^{\pm i\gamma}|\psi_{\pm}> \tag{45}$$

after an amount of cyclic time $\tau = 2\pi/\omega$, so that the first orthogonal state, $|\psi_+>$ acquires a $+\gamma$ phase, and the $|\psi_->$ orthogonal states acquires a $-\gamma$ phase after that time τ.

For an initial state

$$|\Psi_i> = a_+|\psi_+> + a_-|\psi_-> \tag{46}$$

the final state is $|\Psi_f> = U(\chi,\gamma)\ |\Psi_i>$, where the evolution operator is

$$U(\chi,\gamma) = \begin{pmatrix} e^{i\gamma}\cos^2\frac{\chi}{2} + e^{-i\gamma}\sin^2\frac{\chi}{2} & i\sin\chi\sin\gamma \\ i\sin\chi\sin\gamma & e^{i\gamma}\sin^2\frac{\chi}{2} + e^{-i\gamma}\cos^2\frac{\chi}{2} \end{pmatrix} \tag{47}$$

From this evolution operator, any single qubit geometric quantum gate can be constructed, by controlling the three control variables in χ (equation 43).

2.8 Geometric and dynamic phases

Geometric phases in the quantum state of a system occur for any evolution of the state; this evolution is represented by a path in Hilbert space (Abdumalikov 2013) (or as a path on the Bloch sphere). Geometric phase depends only on the solid angle subtended on the Bloch sphere, and for Abelian geometric phases, it is a real number.

When a Bloch vector makes a closed loop on the Bloch sphere, the geometric phase for any two-level system is:

$$GP = -\Theta/2 \tag{48}$$

where Θ is the solid angle enclosed by the curve that the Bloch vector traces out on the Bloch sphere.

The dynamic phase can be set to vanish if the evolution path of the Bloch vector **r** is kept perpendicular to the Rabi vector **Ω**. The dynamic phase is

$$DP = -\frac{1}{\hbar}\int_0^T < \psi(t=0)\left|U^{\dagger}HU\right|\psi(t=0) > dt \tag{49}$$

which is a function of the Hamiltonian H, evolution operator U, the wavefunction ψ, and the time taken for the evolution. The total phase acquired by the quantum state after a cyclical evolution is just the sum of the above geometric and dynamic phases.

2.9 Direct rotations versus composite (N-segment) rotations

In later chapters we present comparisons of direct (single) rotations versus composite (N-segment, with N > 1) rotations. A direct rotation is represented here by a single rotation of the quantum state around the x-axis of the Bloch sphere by an angle θ:

$$U_{direct}(\theta) = e^{-i\frac{\theta}{2}\sigma_x} \tag{50}$$

The total phase of this rotation is -θ/2. Most standard quantum gate operations that do not consider geometric phase are direct rotations. When a direct rotation gate operates on the initial state of equation 4, which points in the x direction, there is no evolution path on the Bloch sphere; the state is just rotated at the x-axis point (see Figure 8). There is no solid angle subtended, and therefore no geometric phase: this gate is therefore a purely dynamic gate.

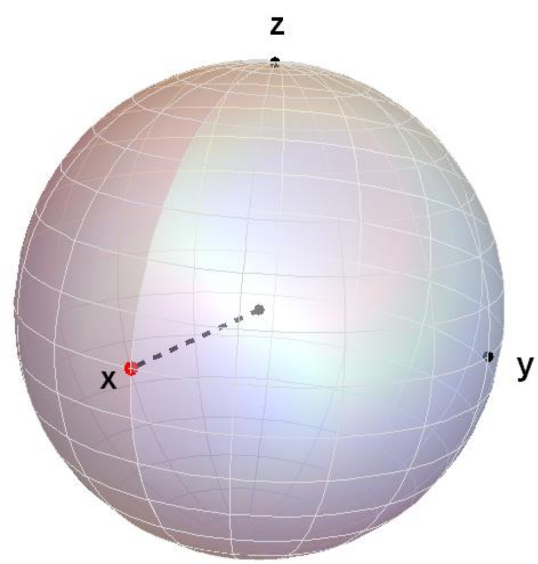

Figure 8- Direct rotation around the x-axis, with initial state on x-axis.

In contrast, a composite rotation is made up of N segments or rotations, which form a closed loop on the Bloch sphere. An example of a composite rotation is:

$$U_{composite} = R_y(\pi)R_z(\pi) \tag{51}$$

This gate is made by starting from the initial state of equation (4) on the x-axis, rotating around the z-axis by π, so that the second endpoint is at the negative x-axis, and then rotating around the y-axis by π to return to the x-axis (see Figure 26a). This makes a 2-segment geometric gate of geometric phase – π/2; the angle between the segments is $\frac{\pi}{2}$ = -GP. This is equivalent to the above direct rotation gate if $\theta = \pi$ there.

2.10 Geometric, dynamic and hybrid gates

Geometric gates have evolution paths only on geodesics, so that the dynamic phase vanishes, and there is only a geometric phase. Dynamic gates have no enclosed area on the Bloch sphere, so that the geometric phase vanishes, and there is only a dynamic phase. The direct rotations of the previous section are an example of dynamic gates. Hybrid gates have both a geometric and a dynamic phase.

2.11 Noise model

The control parameters that define our quantum gate designs are affected by both systematic and random error. These types of noise can affect the fidelity of the designed quantum gates.

Our phase noise is based on the phase diffusion model (Scully 1997), where there is a Gaussian noise distribution on the phase of the laser (our control parameter θ_L). Noise is put on θ_L on each of N time steps, in a random walk: taking the previous value and adding a random value from the interval $\pm\frac{0.01}{\sqrt{N}}$ to find the current value of the phase. Figure 9 shows that the phase noise we used formed a Gaussian distribution.

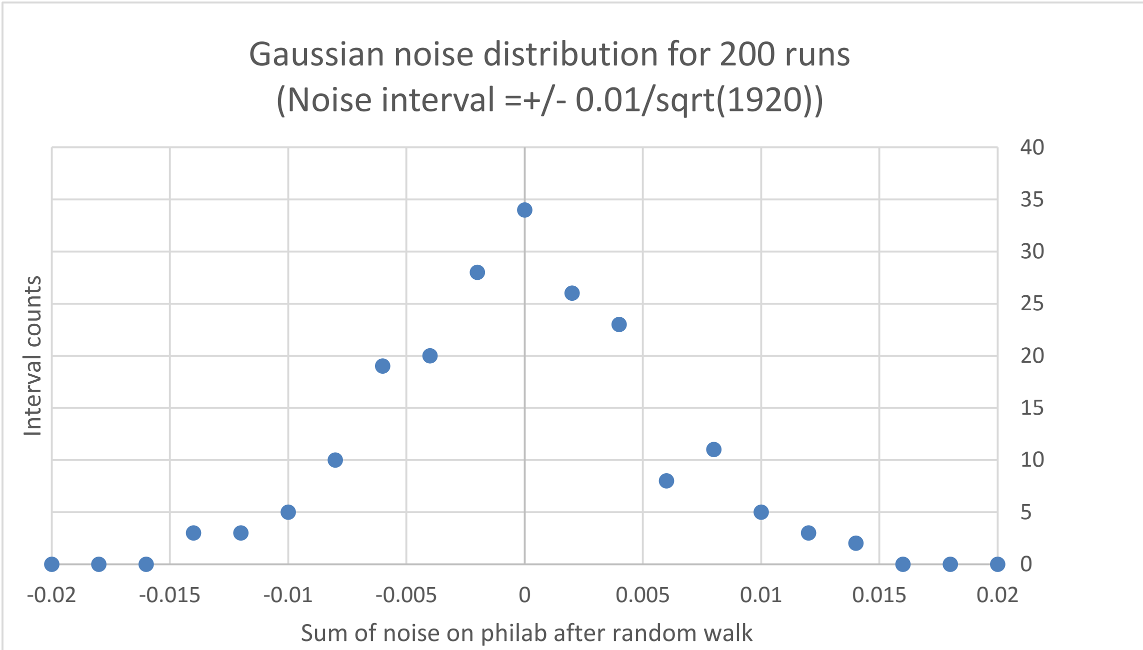

Figure 9-Gaussian noise distribution for random noise on the laser phase θ_L, for N = 1920

Noise on the Rabi frequency control parameter is modeled as a random percentage noise of the ideal value. For instance, for a 10% random noise, a random number between 0.9 and 1.1 is multiplied with the ideal Rabi frequency value at each of N time steps.

Systematic error was applied to the designed quantum gates by applying the same types of noise, but in one single time step for each segment of the rotation.

2.12 Fidelity and error rate

The fidelity F of the paths is found by taking the trace of the ideal evolution matrix U (calculated from the ideal control parameters) multiplied by the noisy U matrix (= V), calculated with noise added to the control parameters (Thomas et. al. 2011):

$$F = \frac{1}{2} Tr|VU^{\dagger}| \tag{52}$$

Each of the paths are divided into N time steps, where noise is applied. The fidelity for each path is averaged over 200 runs. Error rate is defined as 1- F.

2.13 Application of our unified model to the six physical systems

In this section, our unified model developed from the N-segments work is applied by translating our control parameters into the control parameters of each of the six physical systems studied here for creating qubits (see Table 1).

Table 1 – Translation of unified model's control parameters to system control parameters

System	Ω_0	φ_L	Δ
2-Level Atom	Rabi frequency of laser	Phase of the laser	Laser detuning
Trapped Ions	Ω =Rabi frequency of laser	Φ = laser phase	ω_0-ω_L where ω_0 = resonant frequency; ω_L = laser frequency
NMR	$-\omega_0 = \frac{g\mu B_0}{\hbar}$ Proportional to the strength of the rotating B field	φ where phase φ usually set to 0.	$\omega_1 - \omega$ where ω = frequency of rotating B field; constant z-direction B field given by $\omega_1 = -\frac{g\mu B_1}{\hbar}$
Photons	$-\varepsilon$ sin 2θ where $n\pm\varepsilon$ = refractive index of slow/fast axis; θ = angle of birefringent plate's slow axis to x-axis	---	εcos 2θ
Cavity QED: charge qubits	E_J = coupling energy	-α = - phase shift (eq. 37)	$-E_{CH}$ (1-2n_x) where E_{CH} = charging energy; offset charge = $n_x = V_x/2e$; V_x = applied gate voltage
Quantum Dots	-A A=amplitude of laser pulse	φ = laser phase	ε /2 ε = energy band gap of semiconductor dots

CHAPTER 3- THEORY OF N-SEGMENT PATHS

For a closed loop of N segments or rotations, we are always left with a spherical polygon formed by the geodesics between endpoints of segments, plus the associated wedges formed by the evolution path and its associated geodesic (see Figure 10 for an N = 3 example).

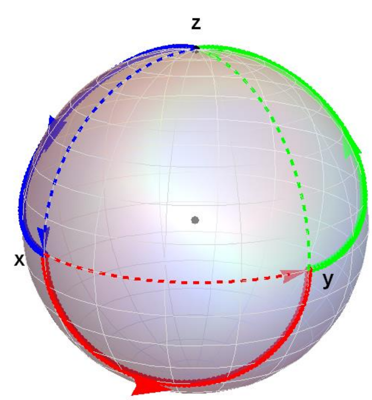

Figure 10- N= 3-segment path, with evolution paths (solid lines with arrows), and their associated geodesics (dashed lines).

We consider fidelity results for special cases of two- and three-segment rotations, as well as quantum gate operations that can be considered N rotations of the qubit state around N axes, creating a closed loop on the Bloch sphere. In each case, the geometric phase of the N-segments path is a sum of the geometric phase of the wedge made by each segment and the geodesic (great circle) between the two endpoints of that segment, plus a geometric phase from the N polygon created from the geodesics between endpoints.

In the N segment case, we have N rotations given by 3N – 2 lab frame control parameters: Ω_0 , Ω_{02} ,…. $\Omega_{0(N-1)}$; φ_L ,φ_{L2} ,…$\varphi_{L(N-1)}$; Δ, Δ_2, …$\Delta_{(N-1)}$; and φ_N. The geometric phase is again a sum of the geometric phase contributions from each segment's wedge, plus a geometric phase from the N-sided polygon formed by each of the segments' associated geodesics:

$$GP = GP_1 + GP_2 +\ldots+ GP_N + GP_{N\text{-polygon}} \tag{53}$$

where $GP_{N\text{-polygon}} = -\frac{1}{2}\,\Omega_{N\text{-polygon}}$, and the solid angle is:

$$\Omega_{N\text{-polygon}} = (\text{Angle } 1) + (\text{Angle } 2) +\ldots.+ (\text{Angle } N) -(N-2)\pi \tag{54}$$

where Angle 1 is the N-polygon's angle associated with endpoint #1, etc; these angles are found from the tangents to the great circles.

3.1 Two-segment paths

This section calculates the geometric, dynamic and total phase for all closed paths on the Bloch sphere made of two segments, each lying on conic circles. By creating a set of all possible rotations, showing that we can vary the total phase interval to coincide with all possible rotation angles of the state vector, and varying the control parameters to create purely dynamic or purely geometric phases, we then are able to compare the fidelity of geometric phase and dynamic phase under noise. We consider the case of the first segment lying on a great circle, and the more general case of non-great circle paths.

We first show we can find a set of paths with total phase continuously varying for a π interval, and that we can maximize the GP while simultaneously minimizing the DP (and vice versa) over this same set of paths for each value of the total phase, by varying the control parameters (in the first case, for the first segment on the great circle, these control parameters are: the angle amount of the first rotation and the angle between the rotation axes).

The reason for the requirement of a π interval total phase is as follows: a unitary operator U for a rotation of the state vector by angle β around a rotation axis $\hat{n}$ is:

$$U_n(\beta) = e^{-i\frac{\beta}{2}\sigma_n} \tag{55}$$

Or in matrix form, for the case that $\sigma_n = \sigma_z$:

$$U_z(\beta) = \begin{pmatrix} e^{-i\frac{\beta}{2}} & 0 \\ 0 & e^{i\frac{\beta}{2}} \end{pmatrix} \tag{56}$$

so that basis vectors along the rotation (z) axis:

$$|n_+ >= \begin{pmatrix} 1 \\ 0 \end{pmatrix}, \qquad |n_- >= \begin{pmatrix} 0 \\ 1 \end{pmatrix} \tag{57}$$

become

$$U_n(\beta)|n_+ >= e^{-i\frac{\beta}{2}}|n_+ > \ , \qquad U_n(\beta)|n_- >= e^{i\frac{\beta}{2}}|n_- > \tag{58}$$

after rotation. In this case, the total phase TP = β/2 = GP + DP where GP = geometric phase and DP = dynamic phase. For example, a segment that makes a complete great circle will have a dynamic phase that vanishes, and the geometric phase is minus one half the solid angle: GP = -π; the total phase TP = -π = β/2. To cover any state vector rotation

β between 0 and 2π, the total phase must be able to vary between 0 and π for the paths selected.

The first segment is assumed to be a rotation on the great circle (we later consider the case of non-great circle paths), in the x-z plane (so that α = (angle from x-axis) = 0 in prior calculations), and symmetrical about the equator (so that the angle from the z-axis to the initial state position is equal to the angle from the negative z-axis to the final state position after the first rotation). Therefore, the first rotation axis is the y-axis. The total angle subtended by the first rotation is β_1. Therefore, the angle made from the initial state position to the x-axis is $\beta_1/2$, and the angle from the z-axis to the initial state position is $\pi/2 - \beta_1/2$.

Our first control parameter is β_1, and it can vary between 0 and 2π, these two extreme values being no first rotation at all. At values close to $\beta_1=0$, the first rotation will be just above the x-axis, and the first rotation will be very slight, ending just below the x-axis; at values close to $\beta_1= 2\pi$, the initial state position is just above the negative x-axis, and the first rotation goes almost all the way around the great circle in the x-z plane, to end just below the negative x-axis.

The second segment closes the loop, and is a rotation about an axis that makes an angle of φ_2 from the x-axis, assumed to be CCW from the x-axis if looking down the z-axis. This angle φ_2 can vary from 0 to 2π, where a value of 0 or 2π would mean that the second axis of rotation was along the x-axis. Our two control parameters are then β_1 and φ_2.

There are two easy ways to make all possible paths: If we fix β_1, then the angle to the second rotation axis, φ_2 can be varied along the equator to get all possible paths for that value of β_1, and we can make graphs of the phases for all values of β_1. Similarly, we can fix φ_2 and vary β_1, making graphs of phases for all values of φ_2. Alternatively, we can make a 3D map of the phases over both control parameters.

For the case of the first segment on a non-great circle path, there is an extra control parameter: the angle φ_1 from the x-axis to the axis of rotation for the first segment. The angle amount β_1' rotated around the 1^{st} axis (φ_1 from the x-axis) is already given by endpoints defined by β_1 (angle amount if you stayed on great circle of x-z plane). Our set of control parameters are then φ_1, φ_2 and β_1.

3.2 Geometry of the two segments

For the first rotation, if we look down the negative y-axis, we see an arc with radius r (see Figure 11). Taking the top half (above the x-y equator) of the arc, the angle the arc subtends is $\beta_1/2$. We can construct a triangle by dropping a dotted line from the initial state position down to the x-axis, kept perpendicular to the z-axis. The length of this dotted line is labeled “z”. From the geometry, we have

$$sin\frac{\beta_1}{2} = \frac{z}{r} = z \tag{59}$$

$$cos\frac{\beta_1}{2} = \frac{d_1}{r} = d_1 \tag{60}$$

using r = 1 for a unit Bloch sphere.

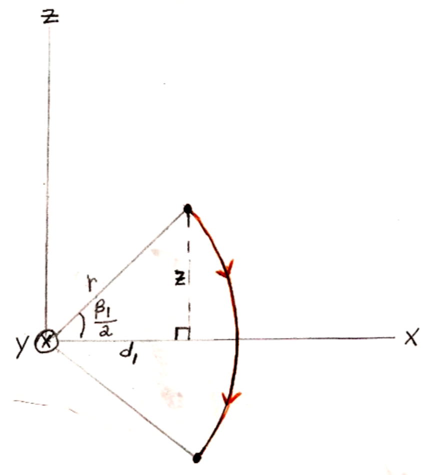

Figure 11- First rotation segment (orange line) around the y-axis (into the paper), by the angle β_1. The distance d_1 is from the origin to the perpendicular dotted line; d_1 measures the minimum distance along the x-axis; the dotted line measures the maximum height z.

Now to close the loop, the second rotation will be an arc on the Bloch sphere, around an axis of rotation called the x”-axis (see Figure 12-Figure 14).

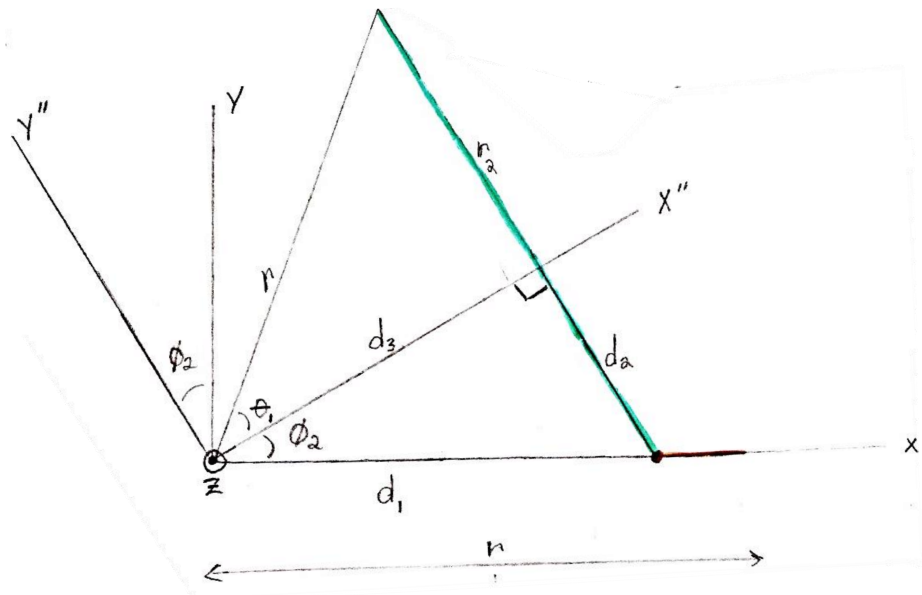

Figure 12- Both rotations (first rotation = orange line; second rotation = green line). Both lines are traversed in both directions. The orange dot is the initial (and final) state position on the Bloch sphere; directly behind it would be the final state position of the first rotation segment.

From the geometry of Figure 12, we have

$$\cos\varphi_2 = \frac{d_3}{d_1}, \quad \sin\varphi_2 = \frac{d_2}{d_1}, \quad \cos\theta_1 = \frac{d_3}{r} = d_3, \quad \sin\theta_1 = \frac{r_2}{r} = r_2 \qquad \textbf{(61)}$$

Using equation (60) for d_1, this becomes:

$$d_3 = \cos(\beta_1/2)\cos\varphi_2 \qquad \textbf{(62)}$$

$$d_2 = \cos(\beta_1/2)\sin\varphi_2 \qquad \textbf{(63)}$$

So that the cone half apex angle θ_1 is given by:

$\cos\theta_1 = \cos(\beta_1/2)\cos\varphi_2$

$r_2 = \sin\theta_1$

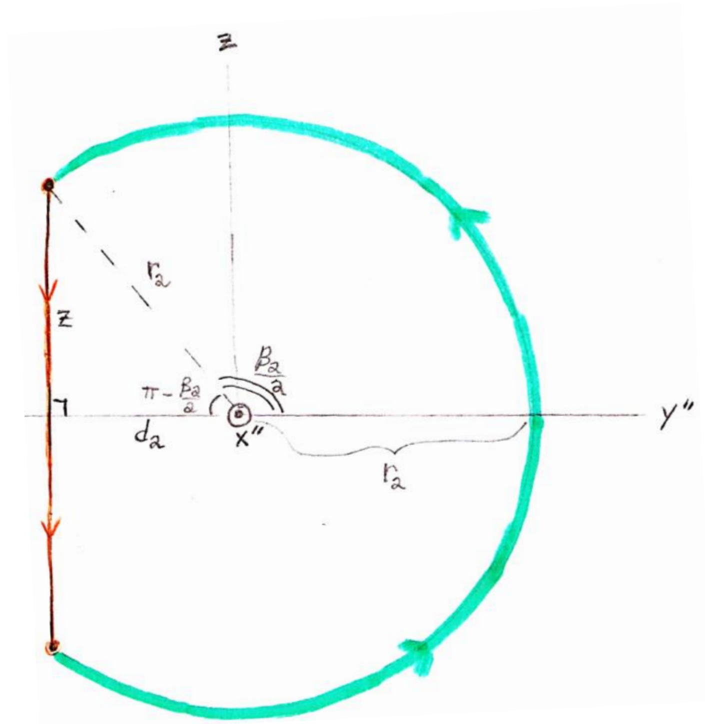

Figure 13- Both rotations seen looking down the x”-axis (second axis of rotation).

From Figure 13, we can define β_2 (the angle of rotation around the second axis of rotation) in terms of the two main control parameters (β_1 and φ_2). Let $\alpha = (\pi - \beta_2/2)$; from figure 3, $\beta_2 = 2\pi - 2\alpha = 2(\pi - \alpha)$. From the geometry of Figure 12Figure 13, we find that

$$\cos\alpha = \frac{r}{r_2}\cos\frac{\beta_1}{2}\sin\varphi_2\,, \qquad \sin\alpha = \frac{r}{r_2}\sin\frac{\beta_1}{2} \tag{64}$$

$$\tan\alpha = \sin\alpha / \cos\alpha = \sin(\beta_1/2) / (\cos(\beta_1/2)\sin\varphi_2)$$

or

$$\alpha = \arctan[\tan(\beta_1/2) / \sin\varphi_2]$$

and we can solve for β_2, the angle amount of the second rotation. Using $\beta_2 = 2(\pi - \alpha)$:

$$\beta_2 = 2(\pi - \arctan[\tan(\beta_1/2) / \sin\varphi_2]) \tag{65}$$

Also from Figure 13, we can determine r_2 by the Pythagorean theorem:

$$r_2^2 = d_2^2 + z^2$$

Substituting in prior equations, we have

$$\sin\theta_1 = \sqrt{cos^2\frac{\beta_1}{2}sin^2\varphi_2 + sin^2\frac{\beta_1}{2}} \qquad \textbf{(66)}$$

The above equations have been calculated with the assumption that the following ranges hold: $0 < \beta_1 < \pi$, $0 \leq \varphi_2 \leq \pi/2$, $0 < \theta_1 < \pi/2$.

3.3 Calculation of geometric phase (first segment on great circle)

The geometric phase (GP) is minus one half the solid angle:

$$GP = -\frac{\Omega}{2} \qquad \textbf{(67)}$$

To calculate the solid angle, we follow Mazonka (2011); see also appendix. We want to calculate the solid angle that the cone associated with the second rotation segment makes, but only up to the great circle on the x-z plane that the first rotation segment lies on (see Figure 14).

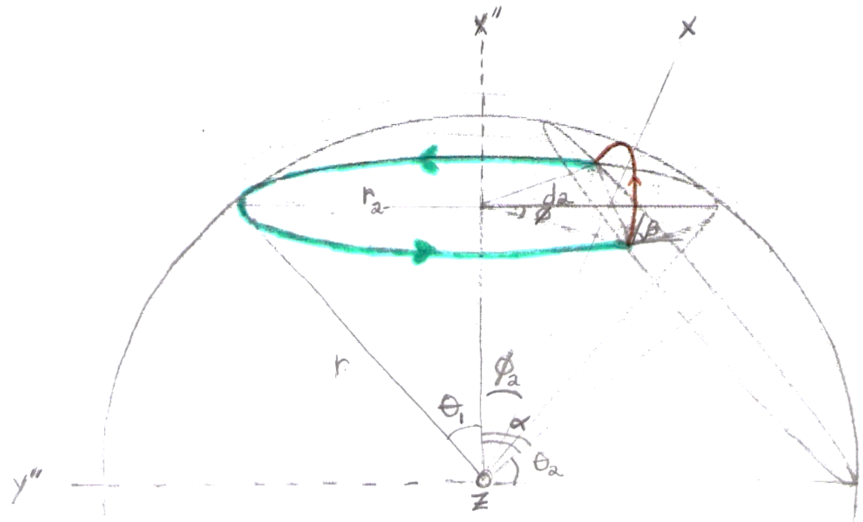

Figure 14- Both rotation segments, with the first segment (orange line) on a great circle in the x-z plane. The second rotation segment (green line) is part of the first cone; this cone makes an angle θ_1 with the x"-axis; the first rotation segment is along the plane of intersection of this cone with another cone making an angle of θ_2 with its axis. (Figure adapted from Mazonka 2011).

Variables of Figure 14 :

θ_1= half of apex angle of the 1st cone, associated with the second rotation segment.

θ_2 = half of apex angle of the 2nd cone, which provides the 2 intersection points where the 2nd cone intersects with the 1st cone.

φ_2 = angle between the x and x" axes (2 rotation axes).

φ = angle between the d_2 segment and the initial state position of the orange (1st) segment.

α = angle between the axes of the two cones.

β = angle between the tangent to the great circle and the tangent to the second rotation segment.

r_2 = radius of the circle for the cone associated with the second rotation segment.

d_2 = segment distance from the center of the 1^{st} cone (of the second rotation segment) to the midpoint of the line connecting the two endpoints of the great circle (first rotation segment); this midpoint lies on the x-axis.

Solid angle of a conical surface

The solid angle of a general conical surface is then

$$\boldsymbol{\Omega = 2\pi - \sum_i \delta_i - \oint dl\sqrt{\vec{u}^2 - (\vec{s}\cdot\vec{u})^2}} \qquad \textbf{(68)}$$

(see Mazonka 2011 and appendix A for a proof of this). This assumes that the solid angle subtended would be 2π (equivalent to a cone subtending one hemisphere) if there were no sharp turns or cut off sections from a cone. The last two terms are corrections cut off from this.

3.4 Calculation of geometric phase (non-great circle paths)

In this case, we keep the initial point and the endpoint of the first segment the same (in the x-z plane). The second segment is the same (makes rotation of angle amount β_2 around axis making an angle φ_2 to the x-axis), but the first segment now is another conic curve of angle amount β_1' that rotates around an axis that makes an angle φ_1 to the x-axis (β_1, without the prime, still represents the angle amount between the initial point and first segment endpoint (points 1 and 2), if we stayed on a great circle).

Summary of geometric phase calculations for all segment paths

The equations for calculating the geometric phase acquired by the quantum state after evolving along the two-segment paths are listed below, given the range of the three main rotated frame control parameters φ_1, β_1, and φ_2. This is a set of 16 equations

(equations 73-88)) if β_2 and $\beta_1{}'$ are used, where their values depend on the range of the three main control parameters:

For $0 < \beta_1 \leq \pi,\ \ 0 \leq \varphi_1 \leq \pi$ and $\pi \leq \beta_1 < 2\pi,\ \ \pi \leq \varphi_1 \leq 2\pi$:

$$\beta_1{}' = \left| 2\ tan^{-1}\left(\frac{tan\frac{\beta_1}{2}}{sin\,\varphi_1}\right)\right| \tag{69}$$

For $0 < \beta_1 \leq \pi,\ \ \pi \leq \varphi_1 \leq 2\pi$ and $\pi \leq \beta_1 < 2\pi,\ \ 0 \leq \varphi_1 \leq \pi$:

$$\beta_1{}' = 2\left\{\pi - \left| tan^{-1}\left(\frac{tan\frac{\beta_1}{2}}{sin\,\varphi_1}\right)\right|\right\} \tag{70}$$

For $0 < \beta_1 \leq \pi,\ \ 0 \leq \varphi_2 \leq \pi$ and $\pi \leq \beta_1 < 2\pi,\ \ \pi \leq \varphi_2 \leq 2\pi$:

$$\beta_2 = 2\left\{\pi - \left| tan^{-1}\left(\frac{tan\frac{\beta_1}{2}}{sin\,\varphi_2}\right)\right|\right\} \tag{71}$$

For $0 < \beta_1 \leq \pi,\ \ \pi \leq \varphi_2 \leq 2\pi$ and $\leq \beta_1 < 2\pi,\ \ 0 \leq \varphi_2 \leq \pi$:

$$\beta_2 = \left| 2\ tan^{-1}\left(\frac{tan\frac{\beta_1}{2}}{sin\,\varphi_2}\right)\right| \tag{72}$$

The geometric phase equations are then:

For $0 \leq \varphi_1 \leq \frac{\pi}{2},\ \ 0 < \beta_1 < 2\pi,\ 0 \leq \varphi_2 \leq \frac{\pi}{2}$:

$$GP = -cos^{-1}\left(\frac{sin\,\varphi_1}{\sqrt{1 - cos^2\frac{\beta_1}{2}cos^2\varphi_1}}\right) + \frac{\beta_1{}'}{2}cos\frac{\beta_1}{2}cos\,\varphi_1 +$$

$$-\pi + cos^{-1}\left(\frac{sin\,\varphi_2}{\sqrt{1 - cos^2\frac{\beta_1}{2}cos^2\varphi_2}}\right) + \frac{\beta_2}{2}cos\frac{\beta_1}{2}cos\,\varphi_2 \tag{73}$$

For $0 \leq \varphi_1 \leq \frac{\pi}{2},\ \ 0 < \beta_1 < 2\pi,\ \ \frac{\pi}{2} \leq \varphi_2 \leq \pi$:

$$GP = -cos^{-1}\left(\frac{sin\,\varphi_1}{\sqrt{1 - cos^2\frac{\beta_1}{2}cos^2\varphi_1}}\right) + \frac{\beta_1{}'}{2}cos\frac{\beta_1}{2}cos\,\varphi_1 +$$

$$-\pi - cos^{-1}\left(\frac{sin\,\varphi_2}{\sqrt{1 - cos^2\frac{\beta_1}{2}cos^2\varphi_2}}\right) + \frac{\beta_2}{2}cos\frac{\beta_1}{2}cos\,\varphi_2 \qquad \textbf{(74)}$$

For $0 \leq \varphi_1 \leq \frac{\pi}{2}, \quad 0 < \beta_1 < 2\pi, \ \pi \leq \varphi_2 \leq \frac{3\pi}{2}$ with condition $\varphi_2 < \varphi_1 - \pi$:

$$GP = -cos^{-1}\left(\frac{sin\,\varphi_1}{\sqrt{1 - cos^2\frac{\beta_1}{2}cos^2\varphi_1}}\right) + \frac{\beta_1{}'}{2}cos\frac{\beta_1}{2}cos\,\varphi_1 +$$

$$-2\pi + cos^{-1}\left(\frac{-\,sin\,\varphi_2}{\sqrt{1 - cos^2\frac{\beta_1}{2}cos^2\varphi_2}}\right) + \frac{\beta_2}{2}cos\frac{\beta_1}{2}cos\,\varphi_2 \qquad \textbf{(75)}$$

(add 2π if $\varphi_2 > \varphi_1 - \pi$).

For $0 \leq \varphi_1 \leq \frac{\pi}{2}, \quad 0 < \beta_1 < 2\pi, \quad \frac{3\pi}{2} \leq \varphi_2 \leq 2\pi$:

$$GP = -cos^{-1}\left(\frac{sin\,\varphi_1}{\sqrt{1 - cos^2\frac{\beta_1}{2}cos^2\varphi_1}}\right) + \frac{\beta_1{}'}{2}cos\frac{\beta_1}{2}cos\,\varphi_1 +$$

$$-cos^{-1}\left(\frac{-\,sin\,\varphi_2}{\sqrt{1 - cos^2\frac{\beta_1}{2}cos^2\varphi_2}}\right) + \frac{\beta_2}{2}cos\frac{\beta_1}{2}cos\,\varphi_2 \qquad \textbf{(76)}$$

For $\frac{\pi}{2} \leq \varphi_1 \leq \pi, \quad 0 < \beta_1 < 2\pi, \ 0 \leq \varphi_2 \leq \frac{\pi}{2}$:

$$GP = cos^{-1}\left(\frac{sin\,\varphi_1}{\sqrt{1 - cos^2\frac{\beta_1}{2}cos^2\varphi_1}}\right) + \frac{\beta_1{}'}{2}cos\frac{\beta_1}{2}cos\,\varphi_1 +$$

$$-\pi + cos^{-1}\left(\frac{sin\,\varphi_2}{\sqrt{1-cos^2\frac{\beta_1}{2}cos^2\varphi_2}}\right) + \frac{\beta_2}{2}cos\frac{\beta_1}{2}cos\,\varphi_2 \qquad \textbf{(77)}$$

For $\frac{\pi}{2} \le \varphi_1 \le \pi, \quad 0 < \beta_1 < 2\pi, \quad \frac{\pi}{2} \le \varphi_2 \le \pi$:

$$GP = cos^{-1}\left(\frac{sin\,\varphi_1}{\sqrt{1-cos^2\frac{\beta_1}{2}cos^2\varphi_1}}\right) + \frac{\beta_1{}'}{2}cos\frac{\beta_1}{2}cos\,\varphi_1 +$$

$$-\pi - cos^{-1}\left(\frac{sin\,\varphi_2}{\sqrt{1-cos^2\frac{\beta_1}{2}cos^2\varphi_2}}\right) + \frac{\beta_2}{2}cos\frac{\beta_1}{2}cos\,\varphi_2 \qquad \textbf{(78)}$$

For $\frac{\pi}{2} \le \varphi_1 \le \pi, \quad 0 < \beta_1 < 2\pi, \quad \pi \le \varphi_2 \le \frac{3\pi}{2}$:

$$GP = cos^{-1}\left(\frac{sin\,\varphi_1}{\sqrt{1-cos^2\frac{\beta_1}{2}cos^2\varphi_1}}\right) + \frac{\beta_1{}'}{2}cos\frac{\beta_1}{2}cos\,\varphi_1 +$$

$$-2\pi + cos^{-1}\left(\frac{-\,sin\,\varphi_2}{\sqrt{1-cos^2\frac{\beta_1}{2}cos^2\varphi_2}}\right) + \frac{\beta_2}{2}cos\frac{\beta_1}{2}cos\,\varphi_2 \qquad \textbf{(79)}$$

For $\frac{\pi}{2} \le \varphi_1 \le \pi, \quad 0 < \beta_1 < 2\pi, \quad \frac{3\pi}{2} \le \varphi_2 \le 2\pi$ with condition $\varphi_2 < \varphi_1 - \pi$:

$$GP = cos^{-1}\left(\frac{sin\,\varphi_1}{\sqrt{1-cos^2\frac{\beta_1}{2}cos^2\varphi_1}}\right) + \frac{\beta_1{}'}{2}cos\frac{\beta_1}{2}cos\,\varphi_1 +$$

$$-2\pi - cos^{-1}\left(\frac{-\,sin\,\varphi_2}{\sqrt{1-cos^2\frac{\beta_1}{2}cos^2\varphi_2}}\right) + \frac{\beta_2}{2}cos\frac{\beta_1}{2}cos\,\varphi_2 \qquad \textbf{(80)}$$

(add 2π if $\varphi_2 > \varphi_1 - \pi$).

For $\pi \le \varphi_1 \le \frac{3\pi}{2}, \quad 0 < \beta_1 < 2\pi, \quad 0 \le \varphi_2 \le \frac{\pi}{2}$ with condition $\varphi_2 < \varphi_1 - \pi$:

$$GP = -cos^{-1}\left(\frac{-\sin\varphi_1}{\sqrt{1-cos^2\frac{\beta_1}{2}cos^2\varphi_1}}\right) + \frac{\beta_1{}'}{2}cos\frac{\beta_1}{2}cos\,\varphi_1$$

$$-2\pi + cos^{-1}\left(\frac{\sin\varphi_2}{\sqrt{1-cos^2\frac{\beta_1}{2}cos^2\varphi_2}}\right) + \frac{\beta_2}{2}cos\frac{\beta_1}{2}cos\,\varphi_2 \qquad \textbf{(81)}$$

(add 2π if $\varphi_2 > \varphi_1 - \pi$).

For $\leq \varphi_1 \leq \frac{3\pi}{2}$, $0 < \beta_1 < 2\pi$, $\frac{\pi}{2} \leq \varphi_2 \leq \pi$:

$$GP = -cos^{-1}\left(\frac{-\sin\varphi_1}{\sqrt{1-cos^2\frac{\beta_1}{2}cos^2\varphi_1}}\right) + \frac{\beta_1{}'}{2}cos\frac{\beta_1}{2}cos\,\varphi_1$$

$$-cos^{-1}\left(\frac{\sin\varphi_2}{\sqrt{1-cos^2\frac{\beta_1}{2}cos^2\varphi_2}}\right) + \frac{\beta_2}{2}cos\frac{\beta_1}{2}cos\,\varphi_2 \qquad \textbf{(82)}$$

For $\leq \varphi_1 \leq \frac{3\pi}{2}$, $0 < \beta_1 < 2\pi$, $\pi \leq \varphi_2 \leq \frac{3\pi}{2}$:

$$GP = -cos^{-1}\left(\frac{-\sin\varphi_1}{\sqrt{1-cos^2\frac{\beta_1}{2}cos^2\varphi_1}}\right) + \frac{\beta_1{}'}{2}cos\frac{\beta_1}{2}cos\,\varphi_1$$

$$-\pi + cos^{-1}\left(\frac{-\sin\varphi_2}{\sqrt{1-cos^2\frac{\beta_1}{2}cos^2\varphi_2}}\right) + \frac{\beta_2}{2}cos\frac{\beta_1}{2}cos\,\varphi_2 \qquad \textbf{(83)}$$

For $\pi \leq \varphi_1 \leq \frac{3\pi}{2}$, $0 < \beta_1 < 2\pi$, $\frac{3\pi}{2} \leq \varphi_2 \leq 2\pi$:

$$GP = -cos^{-1}\left(\frac{-\sin\varphi_1}{\sqrt{1-cos^2\frac{\beta_1}{2}cos^2\varphi_1}}\right) + \frac{\beta_1{}'}{2}cos\frac{\beta_1}{2}cos\,\varphi_1$$

$$-\pi - cos^{-1}\left(\frac{-\sin\varphi_2}{\sqrt{1-cos^2\frac{\beta_1}{2}cos^2\varphi_2}}\right) + \frac{\beta_2}{2}cos\frac{\beta_1}{2}cos\,\varphi_2 \qquad \textbf{(84)}$$

For $\frac{3\pi}{2} \leq \varphi_1 \leq 2\pi, \quad 0 < \beta_1 < 2\pi, \quad 0 \leq \varphi_2 \leq \frac{\pi}{2}$:

$$GP = cos^{-1}\left(\frac{-\sin\varphi_1}{\sqrt{1-cos^2\frac{\beta_1}{2}cos^2\varphi_1}}\right) + \frac{\beta_1{}'}{2}cos\frac{\beta_1}{2}cos\,\varphi_1$$

$$-2\pi + cos^{-1}\left(\frac{\sin\varphi_2}{\sqrt{1-cos^2\frac{\beta_1}{2}cos^2\varphi_2}}\right) + \frac{\beta_2}{2}cos\frac{\beta_1}{2}cos\,\varphi_2 \qquad \textbf{(85)}$$

For $\frac{3\pi}{2} \leq \varphi_1 \leq 2\pi, \quad 0 < \beta_1 < 2\pi, \ \frac{\pi}{2} \leq \varphi_2 \leq \pi$, and $\varphi_2 < \varphi_1 - \pi$:

$$GP = cos^{-1}\left(\frac{-\sin\varphi_1}{\sqrt{1-cos^2\frac{\beta_1}{2}cos^2\varphi_1}}\right) + \frac{\beta_1{}'}{2}cos\frac{\beta_1}{2}cos\,\varphi_1$$

$$-2\pi - cos^{-1}\left(\frac{\sin\varphi_2}{\sqrt{1-cos^2\frac{\beta_1}{2}cos^2\varphi_2}}\right) + \frac{\beta_2}{2}cos\frac{\beta_1}{2}cos\,\varphi_2 \qquad \textbf{(86)}$$

(add 2π to above if $\varphi_2 > \varphi_1 - \pi$)

For $\frac{3\pi}{2} \leq \varphi_1 \leq 2\pi, \quad 0 < \beta_1 < 2\pi, \ \pi \leq \varphi_2 \leq \frac{3\pi}{2}$:

$$GP = cos^{-1}\left(\frac{-\sin\varphi_1}{\sqrt{1-cos^2\frac{\beta_1}{2}cos^2\varphi_1}}\right) + \frac{\beta_1{}'}{2}cos\frac{\beta_1}{2}cos\,\varphi_1$$

$$-\pi + cos^{-1}\left(\frac{-\sin\varphi_2}{\sqrt{1-cos^2\frac{\beta_1}{2}cos^2\varphi_2}}\right) + \frac{\beta_2}{2}cos\frac{\beta_1}{2}cos\,\varphi_2 \qquad \textbf{(87)}$$

For $\frac{3\pi}{2} \leq \varphi_1 \leq 2\pi, \quad 0 < \beta_1 < 2\pi, \quad \frac{3\pi}{2} \leq \varphi_2 \leq 2\pi$:

$$GP = cos^{-1}\left(\frac{-\sin \varphi_1}{\sqrt{1 - cos^2 \frac{\beta_1}{2} cos^2 \varphi_1}}\right) + \frac{\beta_1{}'}{2} cos \frac{\beta_1}{2} cos\ \varphi_1 - \pi$$

$$-cos^{-1}\left(\frac{-\sin \varphi_2}{\sqrt{1 - cos^2 \frac{\beta_1}{2} cos^2 \varphi_2}}\right) + \frac{\beta_2}{2} cos \frac{\beta_1}{2} cos\ \varphi_2 \quad \textbf{(88)}$$

3.5 Calculation of dynamic phase

General case: rotation axes in any direction

For our most general paths, we assume the two rotation axes can be anywhere on the Bloch sphere. We also assume our initial (and final) endpoint of our path is on the x-axis, so that the initial basis states are along the ± x-axis:

$$|\psi_+(t = 0) > = \frac{1}{\sqrt{2}}(|0 > +|1 >) \quad \textbf{(89)}$$

$$|\psi_-(t = 0) > = \frac{1}{\sqrt{2}}(|0 > -|1 >) \quad \textbf{(90)}$$

since the most general qubit is

$$|\psi_+(t = 0) > = \sin\frac{\theta}{2}|0 > +e^{-i\alpha}\cos\frac{\theta}{2}|1 > \quad \textbf{(91)}$$

The initial basis states |+> and |-> can be defined in the x-y plane by:

$$| +>_0 = \frac{1}{\sqrt{2}}(|0 > +e^{-i\alpha}|1 >) \quad \textbf{(92)}$$

$$| ->_0 = \frac{1}{\sqrt{2}}(|0 > -e^{-i\alpha}|1 >) \quad \textbf{(93)}$$

where α is the angle to the x-axis and the polar basis states are chosen as

$$|0 > = \begin{pmatrix}0\\1\end{pmatrix}, \qquad |1 > = \begin{pmatrix}1\\0\end{pmatrix} \quad \textbf{(94)}$$

Here |0> points along the south pole of the Bloch sphere, and |1> along the north pole. (This is in contrast to how |0> is usually represented as the north pole, and usually there is a + sign in the exponential above).

The dynamic phase for the |+> basis state is:

$$DP_+ = -\int_0^{t_1} < \psi_+(t=0)\left|U_1{}^{t*} H_1 U_1\right|\psi_+(t=0) > dt +$$

$$-\int_{t_1}^{T} < \psi_+(t_1)\left|U_2{}^{t*} H_2 U_2\right|\psi_+(t_1) > dt \qquad \textbf{(95)}$$

for both rotation segments.

Each segment's rotation operator is

$$U_n = \exp\left\{-i\,\frac{\beta_n'}{2}\bar{\sigma}\cdot\hat{n}\right\} \qquad \textbf{(96)}$$

where β_n' is the angle amount of rotation around the $\hat{n}$-axis.

The rotation angle β_n' is related to the rotation duration and the Rabi frequency by:

$$\beta_n' = |\Omega_n|\tau \qquad \textbf{(95)}$$

In particular, for the first segment, $\beta_1' = |\Omega_1|\tau$, and the rotation operator is:

$$U_1 = \exp\{-i\,H_1\tau\} = \exp\{-i\,H_1\frac{\beta_1'}{|\Omega_1|}\} \qquad \textbf{(96)}$$

The Hamiltonians for the two segments are:

$$H_1 = \frac{1}{2}(-\Omega_0\cos\varphi_L\sigma_x - \Omega_0\sin\varphi_L\sigma_y + \Delta\sigma_z) = \frac{1}{2}\vec{\Omega}_1\cdot\sigma_n \qquad \textbf{(97)}$$

$$H_2 = \frac{1}{2}(-\Omega_{02}\cos\varphi_{L2}\sigma_x - \Omega_{02}\sin\varphi_{L2}\sigma_y + \Delta_2\sigma_z) = \frac{1}{2}\vec{\Omega}_2\cdot\sigma_n \qquad \textbf{(98)}$$

so that the two evolution operators are:

$$U_1 = \exp\{-i\frac{\beta_1'}{2}(-\frac{\Omega_0}{|\Omega_1|}\cos\varphi_L\sigma_x - \frac{\Omega_0}{|\Omega_1|}\sin\varphi_L\sigma_y + \frac{\Delta}{|\Omega_1|}\sigma_z)\} \qquad \textbf{(99)}$$

$$U_2 = \exp\{-i\frac{\beta_2'}{2}(-\frac{\Omega_{02}}{|\Omega_2|}\cos\varphi_{L2}\sigma_x - \frac{\Omega_{02}}{|\Omega_2|}\sin\varphi_{L2}\sigma_y + \frac{\Delta_2}{|\Omega_2|}\sigma_z)\} \quad \textbf{(100)}$$

where $|\Omega_1| = \sqrt{(\Omega_0)^2 + \Delta^2}$ and$|\Omega_2| = \sqrt{(\Omega_{02})^2 + (\Delta_2)^2}$.

The dynamic phase for the first segment is:

$$DP_+(1) = -\int_0^{t1} < \psi_+(t=0)|U_1^{t*}H_1U_1|\psi_+(t=0) > dt \quad \textbf{(101)}$$

$$= -\int_0^{t1} < \psi_+(t=0)|H_1|\psi_+(t=0) > dt \quad \textbf{(102)}$$

since U and H commute. The dynamic phase for the first segment becomes:

$$DP_+(1) = \frac{\beta_1'\Omega_0}{2|\Omega_1|}\cos\varphi_L \quad \textbf{(103)}$$

$$= \frac{\Omega_0}{2}\cos\varphi_L \quad \textbf{(104)}$$

on setting τ = 1.

The dynamic phase for the second segment is:

$$DP_+(2) = -\int_{t1}^{T} < \psi_+(t_1)|U_2^{t*}H_2U_2|\psi_+(t_1) > dt \quad \textbf{(105)}$$

$$= -\int_{t1}^{T} < \psi_+(t_1)|H_2|\psi_+(t_1) > dt \quad \textbf{(106)}$$

where the state is:

$$\mathrm{U_1|\psi_+(t = 0) > = |\psi_+(t_1) > =}$$

$$= \frac{1}{\sqrt{2}}[\{\cos\frac{\beta_1'}{2} + isin\frac{\beta_1'}{2}\frac{\Omega_0}{|\Omega_1|}\mathrm{e}^{i\varphi_L} + isin\frac{\beta_1'}{2}\frac{\Delta}{|\Omega_1|}\}|0>$$

$$+\{\cos\frac{\beta_1'}{2} + isin\frac{\beta_1'}{2}\frac{\Omega_0}{|\Omega_1|}\mathrm{e}^{-i\varphi_L} - isin\frac{\beta_1'}{2}\frac{\Delta}{|\Omega_1|}\}|1>] \quad \textbf{(107)}$$

This state can also be found from the known coordinates of the second endpoint:

$$n_{E2} = (n_{E2x}, n_{E2y}, n_{E2z}) = (\cos\alpha\ \sin\theta, \sin\alpha\sin\theta, \cos\theta) \quad \textbf{(108)}$$

Where the polar and azimuthal angles θ and α define the general qubit state:

$$|\psi_+(\mathrm{t}_1)>=\sin\frac{\theta}{2}|0>+e^{-i\alpha}\cos\frac{\theta}{2}|1>=C_0|0>+C_1|1> \quad \textbf{(109)}$$

$$DP_+(2)=-\int_{t1}^{T}<\psi_+(t_1)|H_2|\psi_+(t_1)>dt \quad \textbf{(110)}$$

$$=\Omega_{02}C_0\{Re\,(C_1)\cos\varphi_{L2}-Im(C_1)\sin\varphi_{L2}\}+\frac{\Delta_2}{2}\{(C_0)^2-C_1^*C_1\} \quad \textbf{(111)}$$

on setting the time interval to 1, and using the fact C_0 is a real coefficient. The total dynamic phase for the loop is:

$$DP_+=DP_+(1)+DP_+(2) \quad \textbf{(112)}$$

Special case #1: first segment on great circle & rotation axes in x-y plane

The basis states are taken to lie along the direction to the initial state position which is in the x-z plane. For a first segment on the great circle, we can assume the first rotation segment is in the x-z plane, so (α=φ=0):

$$|\psi_+(t=0)>=\sin\frac{\theta}{2}\;|0>\;+\;\cos\frac{\theta}{2}\;|1> \quad \textbf{(113)}$$

$$|\psi_-(t=0)>=\sin\frac{\theta}{2}\;|0>\;-\;\cos\frac{\theta}{2}\;|1> \quad \textbf{(114)}$$

Here θ measures the angle from the z-axis, and $\frac{\theta}{2}=\frac{\pi}{4}-\frac{\beta_1}{4}$, where β_1 measures the angle along the geodesic between the two endpoints.

Each segment's rotation operator is given by equation 96:

$$U_n=\exp\left\{-i\,\frac{\beta_n}{2}\bar{\sigma}\cdot\hat{n}\right\} \quad \textbf{(115)}$$

since in this special case, the evolution path is on the geodesic, so that $\beta_n=\beta_n'$.

For rotation axes in the x-y plane, there is no detuning, so that Δ = 0, and $|\Omega|=\Omega_0$, and

$$\bar{\sigma}\cdot\hat{n}=-\left(\cos\varphi_L\sigma_x+\sin\varphi_L\sigma_y\right) \quad \textbf{(116)}$$

using the lab frame control parameter φ_L. The first segment rotation axis is along the y-axis, so that $\varphi_1 = \pi/2$, so this element of the evolution operator becomes $\sigma \cdot n = -\sigma_y$. The first rotation operator is then

$$\mathrm{U}_1 = \exp\{\mathrm{i}\frac{\beta_1}{2}\sigma_y\} \text{ (lab frame)} \tag{117}$$

in the lab frame (a rotation about the negative y-axis); but in the rotated frame (where the first segment is in the x-z plane) the rotation axis is: $\hat{n}_1 = (\cos\varphi_1, \sin\varphi_1, 0)$ and the evolution operator is:

$$\mathrm{U}_1 = \exp\{-\mathrm{i}\frac{\beta_1}{2}\sigma_y\} \text{ (rotated frame)} \tag{118}$$

Therefore the first Hamiltonian is

$$H_1 = \frac{1}{2}\Omega_0\sigma_y \tag{119}$$

in the rotated frame, since $\mathrm{U}_1 = \exp\{-iH\,t\}$.

The second segment has angle: $\beta_2' = |\Omega_2|\tau$. Assuming the second segment axis is also in the x-y plane, the second Hamiltonian is

$$H_2 = \frac{1}{2}\Omega_{02}(\cos\varphi_2\,\sigma_x + \sin\varphi_2\,\sigma_y) \tag{120}$$

With this, the second rotation operator becomes

$$\mathrm{U}_2 = \exp\{-\mathrm{i}\frac{\beta_2'}{2}(\cos\varphi_2\sigma_x + \sin\varphi_2\sigma_y)\} \tag{121}$$

in the rotated frame.

The first term is a rotation on the great circle, so the dynamic phase there is zero: $DP_+(1) = 0$. The dynamic phase for the second segment is:

$$DP_+(2) = -\int_{t1}^{T} < \psi_+(t_1)|U_2^{t*}H_2U_2|\psi_+(t_1) > dt = -\int_{t1}^{T}\frac{\Omega_{02}}{2}cos\varphi_2\cos\frac{\beta_1}{2}dt$$

$$= -\frac{\beta_2'}{2}\cos\frac{\beta_1}{2}cos\varphi_2 \tag{122}$$

using $\beta_2' = |\Omega_2|\tau$.

Special case #2: non- great circle first segment & rotation axes in x-y plane

For non-great circle paths, our initial and final endpoints of the first segment are the same (we can assume they lie in the x-z plane). But instead of following the great circle between them, the first segment is a rotation around an axis an angle φ_1 from the x-axis. We use the same initial states as above (equations 113-114).

For the special case of the first rotation axis in x-y plane, the Hamiltonian for the first segment is:

$$H_1 = \frac{\Omega_0}{2}(cos\varphi_1\sigma_x + sin\varphi_1\sigma_y) \tag{123}$$

This is a constant Hamiltonian that commutes with the U operators (which cancel), so that the dynamic phase of the first segment is:

$$DP_+(1) = -\int_0^{t_1} < \psi_+(t=0)|U_1^{\,t} * H_1U_1|\psi_+(t=0) > dt$$

$$= -\frac{\Omega_0}{2}\int_0^{t_1}(sin\gamma < 0| + \ cos\gamma < 1|)\left(cos\varphi_1\sigma_x + sin\varphi_1\sigma_y\right)(sin\gamma|0> + cos\gamma|1>)dt$$

$$DP_+(1) = -\frac{\beta_1'}{2}\cos\frac{\beta_1}{2}\cos\varphi_1 \tag{124}$$

using $\sin(2\gamma) = \sin(\frac{\pi}{2} - \frac{\beta_1}{2}) = \cos\frac{\beta_1}{2}$.

For the second segment, we have

$$H_2 = \frac{\Omega_{02}}{2}(cos\varphi_2\sigma_x + sin\varphi_2\sigma_y) \tag{125}$$

The dynamic phase for the second segment is

$$DP_+(2) = -\int_{t_1}^{T} < \psi_+(t_1)\left|U_2{}^{t*}H_2U_2\right|\psi_+(t_1) > dt$$

$$= -\frac{\beta_2'}{2}\cos\frac{\beta_1}{2}\cos\varphi_2 \quad \textbf{(126)}$$

Our final equations for the dynamic phase in the special case of non-great circle paths (keeping rotation axes in x-y plane):

$$DP_+(1) = -\frac{\beta_1{}'}{2}cos\frac{\beta_1}{2}cos\varphi_1 \quad \textbf{(127)}$$

$$DP_+(2) = -\frac{\beta_2'}{2}\cos\frac{\beta_1}{2}cos\varphi_2 \quad \textbf{(128)}$$

for the first and second segments, respectively. The total dynamic phase of the evolution path is:

$$DP_+ = DP_+(1) + DP_+(2) = -\frac{1}{2}cos\frac{\beta_1}{2}(\beta_1'cos\varphi_1 + \beta_2'\, cos\varphi_2) \quad \textbf{(129)}$$

where $\beta_1$is the angle of rotation for the geodesic between the two endpoints of each segment, and $\beta_1'$and β_2' are the angles of rotation for the two segments (evolution paths).

3.6 Total phase (first segment on a great circle)

The total phase is a sum of the geometric and dynamic phases:

$$TP_+ = GP_+ + DP_+ \quad \textbf{(130)}$$

The exact form of this equation depends on the quadrant each control parameter is in. Since the geometric phase is equal to minus half the solid angle, its range is (-2π, 0]. We use a range of total phase from [-π, 0], so that the dynamic phase range is [-π, 2π), but the range of the dynamic phase for a particular value of total phase (TP) is [TP, TP + π).

CHAPTER 4- THREE-SEGMENT PATHS

In this chapter, we consider quantum gate operations that can be considered 3 rotations of the qubit state around 3 axes, creating a closed loop on the Bloch sphere. In the three segment case, the 3N-2 lab frame control parameters are: Ω_0 ,φ_L ,Δ, Ω_{02} ,φ_{L2} ,Δ_2, and φ_3. The geometric phase is the sum of the geometric phases of the wedge each segment makes with its associated geodesic, plus a geometric phase from the spherical triangle made by the three unique geodesics between the three endpoints (see Figure 10).

The first endpoint (starting point of first segment) is constrained to be on the lab frame x-axis:

$$\hat{n}_{E1} = (1,0,0) \qquad \textbf{(131)}$$

since in general we can always rotate the first endpoint there. The second and third endpoints can be anywhere (except we exclude points 1, 2, and 3 coinciding, i.e. all β and β' angles are prevented from being 0); the fourth endpoint (after the third rotation) must close the loop by coinciding with the first endpoint (starting point). With three segments, there is the possibility that segments cross each other, and the geometric phase can be zero if equal areas are traversed in opposite directions (resulting in dynamic gates; see Figure 47).

4.1 First segment

The Rabi vector amplitude for the first segment is equal to the angle amount of the first rotation:

$$|\Omega_1| = \sqrt{(\Omega_0)^2 + \Delta^2} = \beta_1' \tag{132}$$

where we have used $\beta_1' = |\Omega_1|\,\tau$, setting $\tau = 1$. The ranges are: $0 < \beta_1' < 2\pi$; and $0 \leq \varphi_L < 2\pi$.

The Rabi vector is

$$\bar{\Omega}_1 = (-\Omega_0 \cos\varphi_L, -\Omega_0 \sin\varphi_L, \Delta) \tag{133}$$

The first axis of rotation is

$$\hat{n}_1 = \frac{1}{|\Omega|}(-\Omega_0 \cos\varphi_L, -\Omega_0 \sin\varphi_L, \Delta) \tag{134}$$

This axis becomes $\hat{n}_1' = (\cos\varphi_1, \sin\varphi_1, 0)$ in the primed (rotated) frame.

The first segment U matrix is:

$$U_1 = \exp\{-i\,\frac{\beta_1'}{2}\vec{\sigma}\cdot\hat{n}\} \tag{135}$$

$$= \cos\frac{\beta_1'}{2}\, I - i\frac{1}{\beta_1'}\sin\frac{\beta_1'}{2}\{-\Omega_0\cos\varphi_L\,\sigma_x - \Omega_0\sin\varphi_L\,\sigma_y + \Delta\sigma_z\} \tag{136}$$

$$= \begin{pmatrix} \cos\frac{\beta_1'}{2} - i\frac{\Delta}{\beta_1'}\sin\frac{\beta_1'}{2} & i\frac{\Omega_0}{\beta_1'}\sin\frac{\beta_1'}{2}e^{-i\varphi_L} \\ i\frac{\Omega_0}{\beta_1'}\sin\frac{\beta_1'}{2}e^{i\varphi_L} & \cos\frac{\beta_1'}{2} + i\frac{\Delta}{\beta_1'}\sin\frac{\beta_1'}{2} \end{pmatrix} \tag{137}$$

We can divide β_1' into smaller segments and put noise on the lab frame parameters to calculate the fidelity from the U matrix above. We need to now calculate β_1 and φ_1 in order to calculate the geometric phase due to the first segment's wedge.

The direction of the second endpoint of the first segment, n_{E2} is:

$$\hat{n}_{E2} = R_{n1}(\beta_1')\, \hat{n}_{E1} = R_{n1}(\beta_1')\,(1,0,0) \quad \textbf{(138)}$$

where

$$R_{n1}(\beta_1') =$$

$$\begin{bmatrix} \cos\beta_1' + n_{1x}^2(1-cos\beta_1') & n_{1x}n_{1y}(1-cos\beta_1') - n_{1z}sin(\beta_1') & n_{1x}n_{1z}(1-cos\beta_1') + n_{1y}sin(\beta_1') \\ n_{1x}n_{1y}(1-cos\beta_1') + n_{1z}sin(\beta_1') & \cos\beta_1' + n_{1y}^2(1-cos\beta_1') & n_{1y}n_{1z}(1-cos\beta_1') - n_{1x}sin(\beta_1') \\ n_{1x}n_{1z}(1-cos\beta_1') - n_{1y}sin(\beta_1') & n_{1z}n_{1y}(1-cos\beta_1') + n_{1x}sin(\beta_1') & \cos\beta_1' + n_{1z}^2(1-cos\beta_1') \end{bmatrix}$$

(139)

as given by the Rodrigues rotation formula. The components of the second endpoint are found from the above.

Two endpoints define a unique geodesic (great circle segment) between them, which subtend an angle β_1 given by:

$$\cos\beta_1 = \hat{n}_{E1}\cdot\hat{n}_{E2} = n_{E2x} = \cos\beta_1' + \left(\frac{\Omega_0\cos\varphi_L}{\beta_1'}\right)^2 (1-cos\beta_1') \quad \textbf{(140)}$$

so that

$$\beta_1 = cos^{-1}\left[\cos\beta_1' + \left(\frac{\Omega_0\cos\varphi_L}{\beta_1'}\right)^2 (1-cos\beta_1')\right]$$

$$= cos^{-1} n_{E2x} \quad \textbf{(141)}$$

The above angle returns a value between 0 and π, taking the geodesic between the first two endpoints. A rotation of half of this angle from $\hat{n}_{E1}$ along the great circle towards $\hat{n}_{E2}$ is the direction of the x'-axis, which in the lab frame coordinates is:

$$\hat{x}' = R_{n_{gc}}\left(\frac{\beta_1}{2}\right)\hat{n}_{E1} \quad \textbf{(142)}$$

where $\hat{n}_{gc} = \frac{\hat{n}_{E1}\times\hat{n}_{E2}}{sin\beta_1} = \hat{y}' = \frac{1}{sin\beta_1}\left(0, -n_{E2z}, n_{E2y}\right)$ is the normal to the great circle formed by the first two endpoints. The resulting equations for x' blow up in the antipodal case.

Antipodal case

For the antipodal case, the two endpoints of the first segment are opposite:

$$\hat{n}_{E2} = (-1,0,0) \quad \textbf{(143)}$$

in lab frame (xyz) coordinates. The rotation angles are:

$$\beta_1 = \beta_1' = \pi \quad \textbf{(144)}$$

(although there are many non-antipodal cases where $\beta_1' = \pi$, if $\beta_1 = \pi$, then the endpoints are necessarily antipodal). The geodesic is chosen to coincide with the evolution path, so that:

$$\hat{y}' = \hat{n}_1 \quad \textbf{(145)}$$

The x'-axis will be in the y-z plane, pointing halfway along the geodesic; the z'-axis will coincide with the lab frame's x-axis. From x = y x z:

$$\hat{x}' = \hat{n}_1 \times \hat{n}_{E1} = (0, n_{1z}, -n_{1y}) \quad \textbf{(146)}$$

The angle between x' and n_1 is given by $\cos\varphi_1 = \hat{x}' \cdot \hat{n}_1 = 0$, or:

$$\varphi_1 = \frac{\pi}{2} \quad \textbf{(147)}$$

for the antipodal case.

General case (non-antipodal)

Now to find the rotated frame control parameter φ_1, we find the angle between x' and

$\hat{n}_1 = \frac{1}{\beta_1'}(-\Omega_0\cos\varphi_L, -\Omega_0\sin\varphi_L, \Delta)$:

$$\cos\varphi_1 = x'_x n_{1x} + x'_y n_{1y} + x'_z n_{1z} \quad \textbf{(148)}$$

or

$$\cos\varphi_1 = \frac{-\Omega_0\cos\varphi_L}{\beta_1'}\{cos\frac{\beta_1}{2} + \left[\frac{(\Omega_0)^2\sin^2\varphi_L+\Delta^2}{(\beta_1')^2}\right]\frac{sin\frac{\beta_1}{2}}{sin\beta_1}\left(1 - cos\beta_1'\right)\} \quad \textbf{(149)}$$

The above equation blows up if $\beta_1 = \pi$ (antipodal case), besides for the $\beta_1' = 0$ (no first segment rotation) that should also be avoided. To find sin φ_1, we solve for the z'-axis:

$$\hat{z}' = \hat{x}' \times \hat{y}' = (cos\frac{\beta_1}{2}, \mathrm{n}_{E2y}\frac{sin\frac{\beta_1}{2}}{sin\beta_1}, \mathrm{n}_{E2z}\frac{sin\frac{\beta_1}{2}}{sin\beta_1}) \times \frac{1}{sin\beta_1}(0, -\mathrm{n}_{E2z}, \mathrm{n}_{E2y}) \quad \textbf{(150)}$$

$$\hat{z}' \sin\varphi_1$$

$$= \left(\mathrm{n}_{E2y}\frac{sin\frac{\beta_1}{2}}{sin\beta_1}n_{1z} - \mathrm{n}_{E2z}\frac{sin\frac{\beta_1}{2}}{sin\beta_1}n_{1y}, n_{1x}\mathrm{n}_{E2z}\frac{sin\frac{\beta_1}{2}}{sin\beta_1} - cos\frac{\beta_1}{2}n_{1z}, cos\frac{\beta_1}{2}n_{1y} - n_{1x}\mathrm{n}_{E2y}\frac{sin\frac{\beta_1}{2}}{sin\beta_1}\right)$$

(151)

From these components we have 3 equations to solve for sin φ_1. From the first equation for sin φ_1 (which works in all but the antipodal case) and the equation for cos φ_1, we can find the value of φ_1: let cos $\varphi_1 = \chi$; if sin $\varphi_1 \geq 0$, then $\varphi_1 = \cos^{-1}\chi$; else $\varphi_1 = 2\pi - \cos^{-1}\chi$. This keeps φ_1 in the full range $[0,2\pi)$. This gives all the quantities needed to calculate the geometric phase of the first segment wedge.

4.2 Second segment

The basic form of the equations for the second segment match the first segment equations. The second segment's U matrix is:

$$U_2 = \begin{pmatrix} \cos\frac{\beta_2'}{2} - i\frac{\Delta_2}{\beta_2'}\sin\frac{\beta_2'}{2} & i\frac{\Omega_0}{\beta_2'}\sin\frac{\beta_2'}{2}e^{-i\varphi_{L2}} \\ i\frac{\Omega_{02}}{\beta_2'}\sin\frac{\beta_2'}{2}e^{i\varphi_{L2}} & \cos\frac{\beta_2'}{2} + i\frac{\Delta_2}{\beta_2'}\sin\frac{\beta_2'}{2} \end{pmatrix} \quad \textbf{(152)}$$

The second segment Rabi vector amplitude is equal to the angle amount of the second rotation:

$$|\Omega_2| = \sqrt{(\Omega_{02})^2 + \Delta_2{}^2} = \beta_2' \quad \textbf{(153)}$$

where we have used $\beta_2' = |\Omega_2|\tau$, setting $\tau = 1$. The second axis of rotation is

$$\hat{n}_2 = \frac{1}{|\Omega_2|}(-\Omega_{02}\cos \varphi_{L2}, -\Omega_{02}\sin \varphi_{L2}, \Delta_2) \quad \textbf{(154)}$$

This axis becomes $\hat{n}_2$' = (cos φ_2, sin $\varphi_{2,}$ 0) in the primed (rotated) frame.

The direction of the third endpoint is:

$$\hat{n}_{E3} = R_{n2}(\beta_2')\, \hat{n}_{E2} \quad \textbf{(155)}$$

Antipodal case

For the antipodal case, the two endpoints of the second segment are opposite:

$$\hat{n}_{E3} = -\hat{n}_{E2} \quad \textbf{(156)}$$

in lab frame (xyz) coordinates. The rotation angles are:

$$\beta_2 = \beta_2' = \pi \quad \textbf{(157)}$$

(although there are many non-antipodal cases where $\beta_1' = \pi$, if $\beta_2 = \pi$, then the endpoints are necessarily antipodal). The geodesic is chosen to coincide with the evolution path, so that:

$$\hat{y}'' = \hat{n}_2 \quad \textbf{(158)}$$

The x''-axis will be in the plane, pointing halfway along the geodesic; the z''-axis will coincide with the lab frame's nE2 axis. From $\hat{x} = \hat{y} \times \hat{z}$:

$$\hat{x}'' = \hat{n}_2 \times \hat{n}_{E2} \quad \textbf{(159)}$$

The angle between x'' and n_2 is given by cos $\varphi_2 = \hat{x}'' \cdot \hat{n}_2$= 0, or:

$$\varphi_2 = \frac{\pi}{2} \quad \textbf{(160)}$$

for the antipodal case.

General case (non-antipodal)

The geodesic (great circle segment) between the second segment endpoints subtend an angle β_2 given by:

$$\beta_2 = \cos^{-1}(\hat{n}_{E2} \cdot \hat{n}_{E3}) \quad \textbf{(161)}$$

A rotation of half of this angle from $\hat{n}_{E2}$ along the great circle towards $\hat{n}_{E3}$ is the direction of the new x''-axis, which in the lab frame coordinates is:

$$\hat{x}'' = R_{n_{gc}}\left(\frac{\beta_2}{2}\right)\hat{n}_{E2} \quad \textbf{(162)}$$

where $\hat{n}_{gc} = \frac{\hat{n}_{E2} \times \hat{n}_{E3}}{sin\beta_2} = \hat{y}''$ is the normal to the great circle formed by the second and third endpoints.

$$\hat{n}_{gc} = \frac{1}{sin\beta_2}(\mathrm{n}_{E2y}\mathrm{n}_{E3z} - \mathrm{n}_{E2z}\mathrm{n}_{E3y}, \mathrm{n}_{E2z}\mathrm{n}_{E3x} - \mathrm{n}_{E2x}\mathrm{n}_{E3z}, \mathrm{n}_{E2x}\mathrm{n}_{E3y} - \mathrm{n}_{E2y}\mathrm{n}_{E3x}) \quad \textbf{(163)}$$

From x-components:

$$\sin\varphi_2 = \frac{(\hat{x}'' \times \hat{n}_2)_x}{\hat{z}''_x} \quad \textbf{(164)}$$

This is singular only if z'' is in the y-z plane of the lab frame, which occurs if x'' is on the negative x-axis; in this case, we can use y components or z components (atleast one component will be nonzero). Let $\cos\varphi_2 = \chi$; if $\sin\varphi_2 >= 0$, then $\varphi_2 = \cos^{-1}\chi$; else $\varphi_2 = 2\pi - \cos^{-1}\chi$. This keeps φ_2 in the full range $[0,2\pi)$.

4.3 Third (closing) segment

The only lab frame control parameter for the third segment is φ_3, the angle of the third rotation axis n_3 from the x'-axis, since this is all that is needed to close the loop. We want to calculate the associated lab frame parameters Ω_{03} ,φ_{L3} , and Δ_3 (and thereby β_3')

in order to use the U matrix; we also need to find β_3 in order to calculate the geometric phase contribution GP_3 from this segment's wedge.

From previous calculations, we know n_{E3} and n_{E1}. We can calculate β_3 from

$$\cos \beta_3 = \hat{n}_{E1} \cdot \hat{n}_{E3} = n_{E3x}$$

$$\beta_3 = \cos^{-1} n_{E3x} \tag{165}$$

A rotation of $\beta_3/2$ from $\hat{n}_{E3}$ along the great circle towards $\hat{n}_{E1}$ is the direction of the new x'''-axis, which in the lab frame coordinates is:

$$\hat{x}''' = R_{n_{gc}}\left(\frac{\beta_3}{2}\right)\hat{n}_{E3} \tag{166}$$

where $\hat{n}_{gc} = \frac{\hat{n}_{E3} \times \hat{n}_{E1}}{sin\beta_3} = \hat{y}''' = \hat{n}_{gc} = \frac{1}{sin\beta_3}(0, \mathrm{n}_{E3z}, -\mathrm{n}_{E3y})$.

3^{rd} segment antipodal case

In this case $\beta_3 = \beta_3' = \pi$, and $\sin \beta_3 = 0$, so the above equation for y''' is singular. Unlike the other two segments, where we choose the geodesic to be along the evolution path in the antipodal case, here we are given φ_3, the angle between $\hat{n}_3$ and x''' (both in the y-z plane, but there is ambiguity in their directions within this plane). We choose y''' to point along the z-axis, so that x''' = (0,-1,0).

The third axis of rotation is then found from the following rotation:

$$\hat{n}_3 = R_{nE3}(\varphi_3)\hat{x}''' \tag{167}$$

General (non-antipodal) case

To find the lab frame parameters, we need to first find the components of

$$\hat{n}_3 = R_{z'''}(\varphi_3)\hat{x}''' \tag{168}$$

Where the z'''-axis is found from $\hat{z}''' = \hat{x}''' \times \hat{y}'''$:

$$\hat{z}''' = \left(-\mathrm{x}'''_y \frac{\mathrm{n}_{E3y}}{sin\beta_3} - \mathrm{x}'''_z \frac{\mathrm{n}_{E3z}}{sin\beta_3}\right)\hat{\imath} + \mathrm{x}'''_x \frac{\mathrm{n}_{E3y}}{sin\beta_3}\hat{\jmath} + \mathrm{x}'''_x \frac{\mathrm{n}_{E3z}}{sin\beta_3}\hat{k} \tag{169}$$

The components of the third rotation axis are:

$$\mathrm{n}_{3x} = \cos\varphi_3 \cos\frac{\beta_3}{2}\left(n_{E3x} + 2\, sin^2\frac{\beta_3}{2}\right) \tag{170}$$

$$\mathrm{n}_{3y} = -[1 + n_{E3x}(1 - cos\varphi_3)]\frac{\mathrm{n}_{E3y}n_{E3x}}{2cos\left(\frac{\beta_3}{2}\right)} +$$

$$+ [\cos\varphi_3 + n_{E3x}(1 - cos\varphi_3)]\,\mathrm{n}_{E3y}\cos\frac{\beta_3}{2} + sin(\varphi_3)\frac{\mathrm{n}_{E3z}}{sin\beta_3} \tag{171}$$

$$\mathrm{n}_{3z} = -[1 + n_{E3x}(1 - cos\varphi_3)]\frac{\mathrm{n}_{E3z}n_{E3x}}{2cos\left(\frac{\beta_3}{2}\right)} +$$

$$+[\cos\varphi_3 + n_{E3x}(1 - cos\varphi_3)]\mathrm{n}_{E3z}\cos\frac{\beta_3}{2} - sin(\varphi_3)\frac{\mathrm{n}_{E3y}}{sin\beta_3} \tag{172}$$

3rd segment angle of rotation

The rotation angle of the third segment $\beta_3{}'$ is found from the geometry of the third segment wedge:

$$\beta_3' = 2\left|\tan^{-1}\left(\frac{\tan(\beta_3/2)}{\sin\varphi_3}\right)\right| \quad , 0 \le \varphi_3 \le \pi \tag{173}$$

$$\beta_3' = 2\left[\pi - \left|\tan^{-1}\left(\frac{\tan(\beta_3/2)}{\sin\varphi_3}\right)\right|\right] \quad , \pi \le \varphi_3 < 2\pi \tag{174}$$

which matches the equations for $\beta_1{}'$ found from the two-segments work. As a check, the following rotation should result in the x-axis:

$$R_{n3}(\beta_3{}')\mathrm{n}_{E3} = \hat{x} = (1{,}0{,}0) \quad \mathbf{(175)}$$

Where the rotation matrix is:

$$R_{n3}(\beta_3{}') =$$

$$\begin{bmatrix} \cos\beta_3' + n_{3x}^2(1-cos\beta_3') & n_{3x}n_{3y}(1-cos\beta_3') - n_{3z}sin(\beta_3') & n_{3x}n_{3z}(1-cos\beta_3') + n_{3y}sin(\beta_3') \\ n_{3x}n_{3y}(1-cos\beta_3') + n_{3z}sin(\beta_3') & \cos\beta_3' + n_{3y}^2(1-cos\beta_3') & n_{3y}n_{3z}(1-cos\beta_3') - n_{3x}sin(\beta_3') \\ n_{3x}n_{3z}(1-cos\beta_3') - n_{3y}sin(\beta_3') & n_{3z}n_{3y}(1-cos\beta_3') + n_{3x}sin(\beta_3') & \cos\beta_3' + n_{3z}^2(1-cos\beta_3') \end{bmatrix} \quad \mathbf{(176)}$$

Third segment lab frame control parameters

The third segment Rabi vector amplitude is equal to the angle amount of the third rotation:

$$|\Omega_3| = \sqrt{(\Omega_{03})^2 + \Delta_3{}^2} = \beta_3{}' \quad \mathbf{(177)}$$

where we have used $\beta_3' = |\Omega_3|\ \tau$, setting $\tau = 1$. The third axis of rotation is

$$\hat{n}_3 = \frac{1}{|\Omega_3|}(-\Omega_{03}\cos\varphi_{L3}, -\Omega_{03}\sin\varphi_{L3}, \Delta_3) \quad \mathbf{(178)}$$

The lab frame parameters Ω_{03} ,φ_{L3} , and Δ_3 are:

$$\Omega_{03} = \beta_3{}'\sqrt{\mathrm{n}_{3x}{}^2 + \mathrm{n}_{3y}{}^2} \quad \mathbf{(179)}$$

$$\Delta_3 = \beta_3{}'\mathrm{n}_{3z} \quad \mathbf{(180)}$$

$$\cos\varphi_{L3} = -\frac{\beta_3{}'\mathrm{n}_{3x}}{\Omega_{03}} \quad \mathbf{(181)}$$

$$\sin\varphi_{L3} = -\frac{\beta_3{}'\mathrm{n}_{3y}}{\Omega_{03}} \quad \mathbf{(182)}$$

If $\sin\varphi_{L3} \geq 0$,

$$\varphi_{L3} = cos^{-1}\left(-\frac{\beta_3{}'\mathrm{n}_{3x}}{\Omega_{03}}\right) \quad \mathbf{(183)}$$

else

$$\varphi_{L3} = 2\,\pi - \, cos^{-1}\left(-\frac{\beta_3{'}n_{3x}}{\Omega_{03}}\right) \tag{184}$$

The third segment's U matrix is:

$$U_3 = \begin{pmatrix} \cos\frac{\beta_3'}{2} - i\,\frac{\Delta_3}{\beta_3'}\sin\frac{\beta_3'}{2} & i\,\frac{\Omega_{03}}{\beta_3'}\sin\frac{\beta_3'}{2}\,e^{-i\varphi_{L3}} \\ i\,\frac{\Omega_{03}}{\beta_3'}\sin\frac{\beta_3'}{2}\,e^{i\varphi_{L3}} & \cos\frac{\beta_3'}{2} + i\,\frac{\Delta_3}{\beta_3'}\sin\frac{\beta_3'}{2} \end{pmatrix} \tag{185}$$

4.4 Geometric phase of segment wedges

The segment wedges are loops made by an evolution segment in the direction of evolution, and the unique associated geodesic along the direction opposite to evolution direction. For the first segment wedge, the geometric phase GP_1 is a function of β_1, β_1', and φ_1. Each wedge's geometric phase follows from the geometric phase equations for the first segment of the two segments work, where the first segment is on the great circle, with a difference caused by going in the opposite direction of evolution.

The equations for the geometric phase of each wedge depends on the quadrant of the angle φ_1 between the geodesic and the rotation axis:

For $0 \leq \varphi_1 \leq \frac{\pi}{2}$:

$$GP_1 = -cos^{-1}\left(\frac{-sin\,\varphi_1}{\sqrt{1-cos^2\frac{\beta_1}{2}cos^2\varphi_1}}\right) + \left(\frac{\beta_1{'}}{2} - \pi\right) cos\,\frac{\beta_1}{2}\,cos\,\varphi_1 \tag{186}$$

For $\frac{\pi}{2} \leq \varphi_1 \leq \pi$:

$$GP_1 = -2\pi + cos^{-1}\left(\frac{-sin\,\varphi_1}{\sqrt{1-cos^2\frac{\beta_1}{2}cos^2\varphi_1}}\right) + \left(\frac{\beta_1{'}}{2} - \pi\right) cos\,\frac{\beta_1}{2}\,cos\,\varphi_1 \tag{187}$$

For $\leq \varphi_1 \leq \frac{3\pi}{2}$:

$$GP_1 = -\pi - cos^{-1}\left(\frac{sin\,\varphi_1}{\sqrt{1-cos^2\frac{\beta_1}{2}cos^2\varphi_1}}\right) + \left(\frac{\beta_1{}'}{2} - \pi\right) cos\frac{\beta_1}{2} cos\,\varphi_1 \qquad \textbf{(188)}$$

For $\frac{3\pi}{2} \leq \varphi_1 \leq 2\pi$:

$$GP_1 = -\pi + cos^{-1}\left(\frac{sin\,\varphi_1}{\sqrt{1-cos^2\frac{\beta_1}{2}cos^2\varphi_1}}\right) + \left(\frac{\beta_1{}'}{2} - \pi\right) cos\frac{\beta_1}{2} cos\,\varphi_1 \qquad \textbf{(189)}$$

For the second (third) segment wedge, the equations that follow apply for GP_2 (and GP_3) with the “1” subscripts replaced with “2” (or “3”).

4.5 Geometric phase of the spherical triangle

For the geometric phase contribution from the spherical triangle, we need the tangent vector to each of the three great circles, taken in the direction of evolution: τ_1,τ_2, and τ_3; the spherical triangle angles A,B,C (at endpoints 1,2,3 respectively) are then:

$$A = \pi - \cos^{-1}(\tau_3 \cdot \tau_1);\ B = \pi - \cos^{-1}(\tau_1 \cdot \tau_2);\ C = \pi - \cos^{-1}(\tau_2 \cdot \tau_3) \qquad \textbf{(190)}$$

since the tangent vectors to the great circles are unit vectors; $\tau 3 \cdot \tau 1$ is evaluated at the first endpoint; $\tau 1 \cdot \tau 2$ at the second endpoint; and $\tau 2 \cdot \tau 3$ at the third endpoint. If the tangent of the segment coming into the endpoint (following evolution direction) is reversed so that it opposes the evolution direction, this equation becomes:

$$A = \cos^{-1}(\tau_3 \cdot \tau_1);\ B = \cos^{-1}(\tau_1 \cdot \tau_2);\ C = \cos^{-1}(\tau_2 \cdot \tau_3) \qquad \textbf{(191)}$$

The solid angle of the spherical triangle is then

$$\Omega_\Delta = A + B + C - \pi \qquad \textbf{(192)}$$

And the geometric phase of the spherical triangle is:

$$GP_{\Delta} = (\pm) * 1/2\ (A + B + C - \pi) \quad \textbf{(193)}$$

where the (-) sign is for outward pointing vectors given by the right hand rule along the evolution of the three segments. The sign of the GP(triangle) is negative if

$$nE3 \cdot (nE1 \text{ x } nE2) \geq 0\ , \quad \textbf{(194)}$$

unless there are antipodal segment endpoints.

In the case of an antipodal first segment (so that the second endpoint is at (-1,0,0), opposite to the first endpoint), the sign of the GP depends on the first rotation axis y', and the location of the third endpoint. The GP sign is negative if:

$$nE3 \cdot y' \geq 0\ \ (\beta_1 = \pi) \quad \textbf{(195)}$$

For an antipodal second segment (second and third endpoints opposite to each other), the GP sign is negative if:

$$nE1 \cdot y'' \geq 0\ \ (\beta_2 = \pi) \quad \textbf{(196)}$$

i.e., the x component of y'' must be nonnegative:

$$(y'')_x \geq 0\ \ (\beta_2 = \pi) \quad \textbf{(197)}$$

For an antipodal third segment (so that third endpoint is at (-1,0,0)), the sign of the geometric phase depends on the third rotation axis, y''', and the location of the 2nd endpoint. The sign of the GP(triangle) is negative if

$$nE2 \cdot y''' \geq 0\ \ (\beta_3 = \pi) \quad \textbf{(198)}$$

The coordinates of a great circle in the x-z plane are:

$$s_1 = (\cos\varphi', 0, \sin\varphi') \quad \textbf{(199)}$$

where φ' is measured from the x-axis in the z-axis direction. After rotating the great circle clockwise around the x-axis by angle γ until it coincides with the first segment, the great circle coordinates become:

$$s_1 = (\cos\varphi', \sin\varphi' \sin\gamma, \sin\varphi' \cos\gamma) \quad \textbf{(200)}$$

The tangent to the great circle is:

$$\tau_1 = \frac{ds_1}{d\varphi'} = (-\sin\varphi', \cos\varphi' \sin\gamma, \cos\varphi' \cos\gamma) \quad \textbf{(201)}$$

If the first segment tangent is evaluated at the first endpoint $\hat{n}_{E1} = (1,0,0)$, then $\varphi' = 0$.

$$\tau_1(nE1) = (0, \sin\gamma, \cos\gamma) \quad \textbf{(202)}$$

If we evaluate the great circle point's coordinates at the second endpoint, then $\varphi' = \beta_1$ and:

$$s_1 = (\cos\beta_1, \sin\beta_1 \sin\gamma, \sin\beta_1 \cos\gamma) = n_{E2} \quad \textbf{(203)}$$

so that $n_{E2x} = \cos\beta_1$; $n_{E2y} = \sin\beta_1 \sin\gamma$ and $n_{E2z} = \sin\beta_1 \cos\gamma$. The tangent to the first segment at the second endpoint becomes

$$\tau_1(nE2) = (-\sin\beta_1, \frac{n_{E2x}\, n_{E2y}}{\sin\beta_1}, \frac{n_{E2x}\, n_{E2z}}{\sin\beta_1}) \quad \textbf{(204)}$$

pointing in the direction of evolution. At the first endpoint, the first segment tangent becomes:

$$\tau_1(nE1) = (0, \frac{n_{E2y}}{\sin\beta_1}, \frac{n_{E2z}}{\sin\beta_1}) \quad \textbf{(205)}$$

also pointing in the direction of evolution.

Similarly, if we take another great circle in the x-z plane, and rotate it by a different angle γ_3 clockwise around the x-axis until it coincides with the third segment, we obtain the third segment coordinates:

$$s_3 = (\cos\varphi''' , \sin\varphi''' \sin\gamma_3 , \sin\varphi''' \cos\gamma_3) \quad \textbf{(206)}$$

The tangent of the third segment is then:

$$\tau_3 = \frac{ds_3}{d\varphi'''} = (-\sin\varphi''' , \cos\varphi''' \sin\gamma_3 , \cos\varphi''' \cos\gamma_3) \quad \textbf{(207)}$$

Evaluated at the third endpoint, the coordinates are:

$$s_3 = (\cos\beta_3 , \sin\beta_3 \sin\gamma_3 , \sin\beta_3 \cos\gamma_3) = n_{E3} \quad \textbf{(208)}$$

and the third segment tangent at the third endpoint is:

$$\tau_3(nE3) = (-\sin\beta_3 , \frac{n_{E3x}\, n_{E3y}}{\sin\beta_3}, \frac{n_{E3x}\, n_{E3z}}{\sin\beta_3}) \quad \textbf{(209)}$$

This tangent points opposite to the evolution direction.

At the first endpoint, β_3 = 0, so that

$$s_3 = (1{,}0{,}0) = n_{E1} \quad \textbf{(210)}$$

The third segment tangent at the first endpoint is:

$$\tau_3(nE1) = (0, \sin\gamma_3 , \cos\gamma_3) = (0, \frac{n_{E3y}}{\sin\beta_3}, \frac{n_{E3z}}{\sin\beta_3}) \quad \textbf{(211)}$$

which also points opposite to the evolution direction. If we now rotate the second endpoint onto the x-axis:

$$R_{-y'}(\beta_1) n_{E2} = (1{,}0{,}0) \quad \textbf{(212)}$$

then we can use the same form of equations above to find the tangents at the second endpoint, by first rotating the first and third endpoint by the matrix $R_{-y'}(\beta_1)$:

$$R_{-y'}(\beta_1) n_{E1} = (n_{E1x}{}^{(r2)}, n_{E1y}{}^{(r2)}, n_{E1z}{}^{(r2)}) \quad \textbf{(213)}$$

$$R_{-y'}(\beta_1) n_{E3} = (n_{E3x}{}^{(r2)}, n_{E3y}{}^{(r2)}, n_{E3z}{}^{(r2)}) \quad \textbf{(214)}$$

where the (r2) superscript signifies we have rotated the endpoint coordinates into the frame where the second endpoint is on the x-axis. We then have the following tangent equations:

$$\tau_2(nE2, r2\ coords) = (0, \frac{n_{E3y}{}^{(r2)}}{\sin\beta_2}, \frac{n_{E3z}{}^{(r2)}}{\sin\beta_2}) \quad \textbf{(215)}$$

which points in the evolution direction, and

$$\tau_1(nE2, r2\ coords) = \ (0, \frac{n_{E1y}{}^{(r2)}}{\sin\beta_1}, \frac{n_{E1z}{}^{(r2)}}{\sin\beta_1}) \quad \textbf{(216)}$$

which points opposite to evolution direction.

Similarly, if we rotate the third endpoint onto the x-axis:

$$R_{y'''}(\beta_3)n_{E3} \ = (1,0,0) \quad \textbf{(217)}$$

And rotate the other endpoint by the same matrix:

$$R_{y'''}(\beta_3)n_{E1} \ = (n_{E1x}{}^{(r3)}, n_{E1y}{}^{(r3)}, n_{E1z}{}^{(r3)}) \quad \textbf{(218)}$$

$$R_{y'''}(\beta_3)n_{E2} \ = (n_{E2x}{}^{(r3)}, n_{E2y}{}^{(r3)}, n_{E2z}{}^{(r3)}) \quad \textbf{(219)}$$

Where the (r3) superscript signifies we have rotated the endpoint coordinates into the frame where the third endpoint is on the x-axis. We then have the following tangent equations:

$$\tau_3(nE3, r3\ coords) = (0, \frac{n_{E1y}{}^{(r3)}}{\sin\beta_3}, \frac{n_{E1z}{}^{(r3)}}{\sin\beta_3}) \quad \textbf{(220)}$$

in the evolution direction.

$$\tau_2(nE3, r3\ coords) = \ (0, \frac{n_{E2y}{}^{(r3)}}{\sin\beta_2}, \frac{n_{E2z}{}^{(r3)}}{\sin\beta_2}) \quad \textbf{(221)}$$

opposite evolution direction.

For the special case of antipodal endpoints for a segment (any of the β's equal to π), we choose the rule that the associated geodesic should coincide with the evolution path, so that GP = 0 for that segment's wedge. The segment's geodesic in this case is determined solely by the axis y' (or y'', y''') the evolution's path rotates about. The tangent vectors of an antipodal segment are the same at both endpoints (flipping the direction of the second tangent); these tangent vectors may need to first be rotated into the same coordinates as the other tangent vector at the endpoint, in order to find the angle there.

For example, in the case of antipodal endpoints for the first segment, $\beta_1 = \beta_1' = \pi$, and the tangent vector for the first segment at the first endpoint is the cross product of the rotation axis for the first segment (y') and the coordinates of the first endpoint (nE1):

$$\tau_1(nE1, \beta_1 = \pi) = y' \times n_{E1} \qquad \textbf{(222)}$$

in the direction of evolution. The tangent to the second segment at the second endpoint is the same (with evolution opposite to evolution), but the coordinates must be rotated into the r2 coordinates before taking the dot product with $\tau_2(nE2, r2\ coords)$, in order to find angle B.

For an antipodal third segment, the tangent is:

$$\tau_3(nE1, \beta_3 = \pi) = y''' \times n_{E3} \qquad \textbf{(223)}$$

opposite to evolution direction. The third segment tangent at the third endpoint, $\tau_3(nE3, \beta_3 = \pi)$, is the same, but rotated around y''' by β_3 to get into r3 coordinates; this tangent vector is in the evolution direction.

For an antipodal second segment, the tangent is:

$$\tau_2(nE2, \beta_2 = \pi, r2\ coords) = R(\, y'' \times n_{E2}) \qquad \textbf{(224)}$$

where R is a rotation around y' by β_1 to get into r2 coordinates; this vector is in direction of evolution. At the third endpoint, $\tau_2(nE3, \beta_2 = \pi)$ must first be rotated back to lab frame coordinates, and then to the r3 coordinates; this tangent vector is opposite to the evolution direction.

The full geometric phase of the three segments can now be calculated as:

$$\mathrm{GP} = \mathrm{GP}_1 + \mathrm{GP}_2 + \mathrm{GP}_3 + \mathrm{GP}_\Delta \qquad \textbf{(225)}$$

If this value of GP is positive, we then use

$$\mathrm{GP} = \mathrm{GP} - 2\,\pi \qquad \textbf{(226)}$$

to keep the geometric phase in the range (-2π, 0].

4.6 Dynamic phase of the three segments

The dynamic phase is a sum of these three-segment dynamic phases; the first two segments' dynamic phases are calculated as before. For the third segment, we use the known coordinates of the third endpoint:

$$n_{E3} = \left(n_{E3x}, n_{E3y}, n_{E3z}\right) = (\cos\alpha\ \sin\theta, \sin\alpha\sin\theta\,, \cos\theta) \qquad \textbf{(227)}$$

Where the polar and azimuthal angles θ and α define the general qubit state:

$$|\psi_+(\mathrm{t}_2)> = \sin\frac{\theta}{2}|0> + e^{-i\alpha}\cos\frac{\theta}{2}|1>$$

$$= C_{03}|0> + C_{13}|1> \qquad \textbf{(228)}$$

To find this state in terms of the endpoint, we calculate:

$$\theta = \cos^{-1} n_{E3z} \qquad \textbf{(229)}$$

$$e^{-i\alpha} = \frac{n_{E3x}}{\sin\theta} - i\,\frac{n_{E3y}}{\sin\theta} \quad \textbf{(230)}$$

setting $\alpha = 0$ if $\theta = 0$ or π. The third segment dynamic phase is:

$$DP_{+}(3) = -\int_{t2}^{T} < \psi_{+}(t_2)|H_3|\psi_{+}(t_2) > dt \quad \textbf{(231)}$$

$$= \frac{1}{2}\left[\Omega_{03}\left\{C_{03}^{*}C_{13}\,\mathrm{e}^{i\varphi_{L3}} + C_{13}^{*}\,C_{03}\,\mathrm{e}^{-i\varphi_{L3}}\right\} + \Delta_3(C_{03}^{*}C_{03} - C_{13}^{*}C_{13})\right] \quad \textbf{(232)}$$

$$= \Omega_{03}C_{03}\{Re\,(C_{13})\cos\varphi_{L3} - Im(C_{13})\sin\varphi_{L3}\} + \frac{\Delta_3}{2}\{(C_{03})^2 - C_{13}^{*}C_{13}\} \quad \textbf{(233)}$$

on setting the time interval to 1. The total dynamic phase is: $DP_{+} = DP_{+}(1) + DP_{+}(2) + DP_{+}(3)$.

CHAPTER 5- TWO-SEGMENT ROTATION RESULTS

This chapter contains the results of our research into the design of rotation paths for quantum gates, using two-segment rotations. We have calculated the dynamic, geometric and total phases for all possible two-segment rotations on the Bloch sphere.

Purely geometric rotations can be built from rotations where β_1' (the angle amount of the first segment) is set to π (this forces the first segment unto a great circle), and the control variable φ_2 is allowed to vary. In this case, β_2' (the angle amount of the second segment) is constrained to also be π; since both segments are on great circles, the dynamic phase vanishes.

To build purely dynamic gates using two segments, we must use the paths where the both rotation axes are along the first endpoint (along the positive or negative x-axis). In this case, the two endpoints coincide and there is no loop. The only other place where the geometric phase is zero for two-segment paths is along a retraced path, on which the dynamic phase is also zero.

5.1 Geometric gates versus direct rotations

Gaussian noise on phase

When Gaussian noise was put on the phase control parameter (φ_L), the 2-segment composite rotations were seen to have much lower error rates than direct rotations. From

Figure 15, it can be seen that the highest fidelity 2-segment geometric gates performed much better than the direct rotations over the full spectrum of rotation angles.

Our research showed that the design of the best paths may involve using a small Rabi frequency in the rotation. A correlation between small Rabi frequency and high fidelity was seen for all two-segment geometric gates (Figure 16).

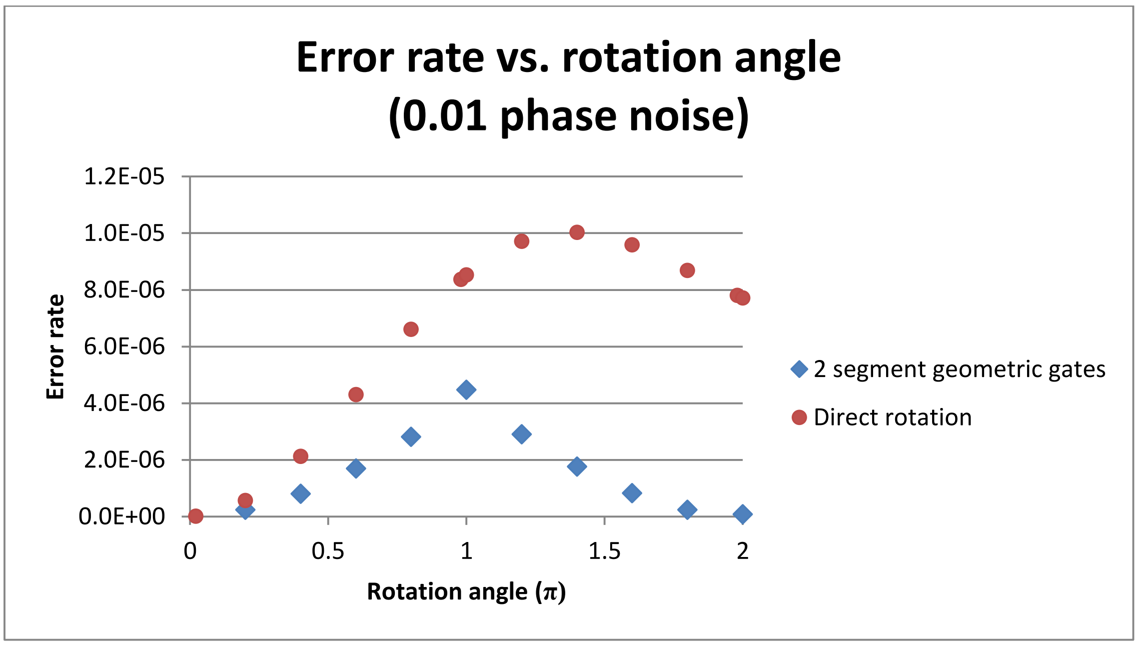

Figure 15- Error rate vs. rotation angle, Gaussian noise on φ_L.

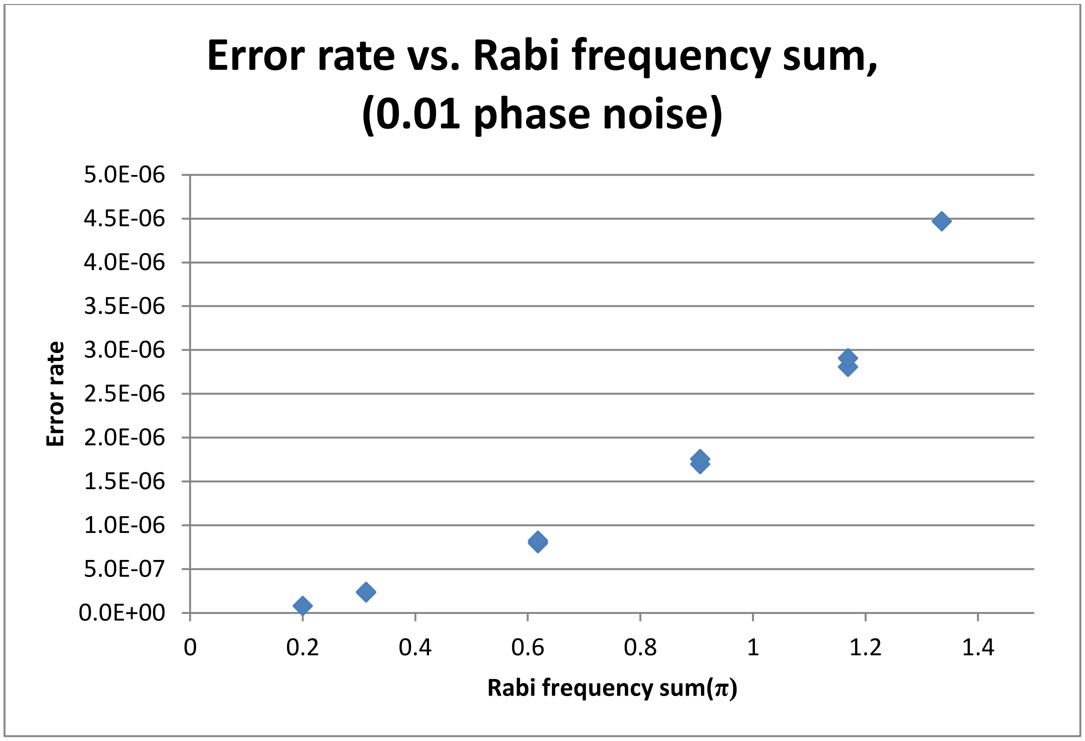

Figure 16-Error rate vs. sum of the Rabi frequencies of both segments, for 2-segment geometric gates.

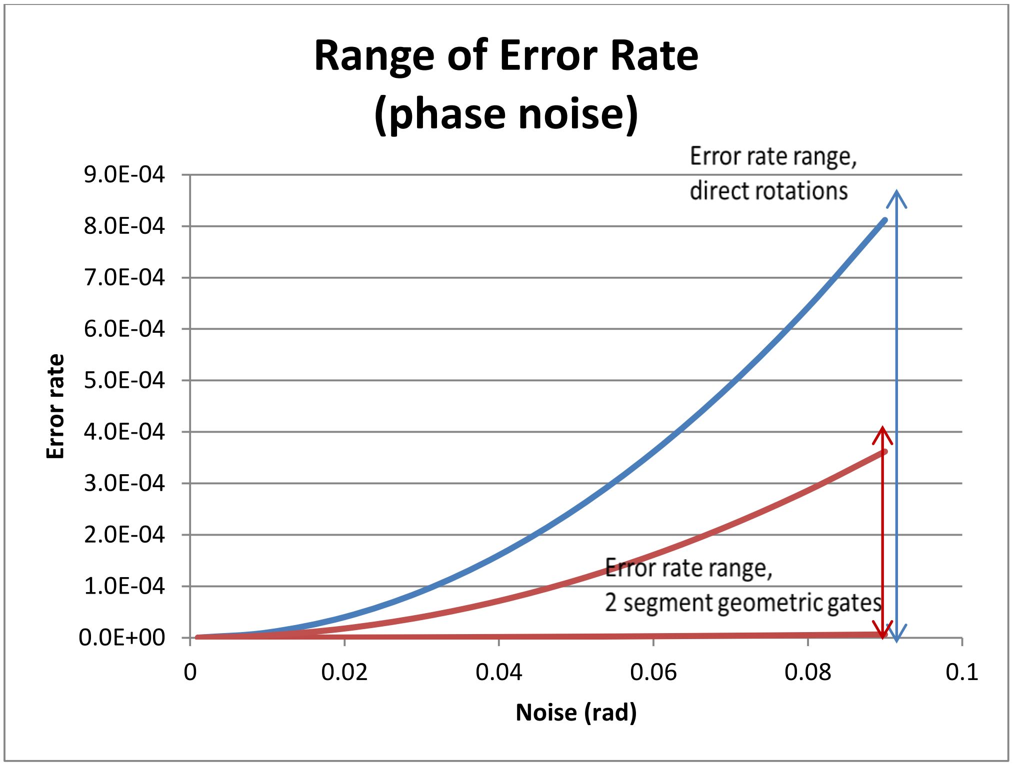

Figure 17-Range of error rate for geometric gates and direct rotations, over spectrum of phase noise level.

Geometric gates also had lower error rates than direct rotations across a range of levels of phase noise (Figure 17). In the direct rotation case, the best error rate occurred for total phase = 0; the worst occurred for total phase = - 0.7 π. For geometric gates, the best error rate occurred for total phase = - 1.0 π; the worst occurred for total phase = - 0.5 π.

Random percentage noise on Rabi frequency

In contrast to the phase noise plots, the direct rotations actually perform better than the 2-segment geometric gates at the lower half of rotation angles when there is a 10% Rabi frequency noise, whereas there is a drastic improvement in error rates for the

2-segment geometric gates over the direct rotation for higher rotation angles (Figure 18). Under this noise, there was the same correlation between high fidelity and small Rabi frequencies for the two-segment geometric gates (Figure 19).

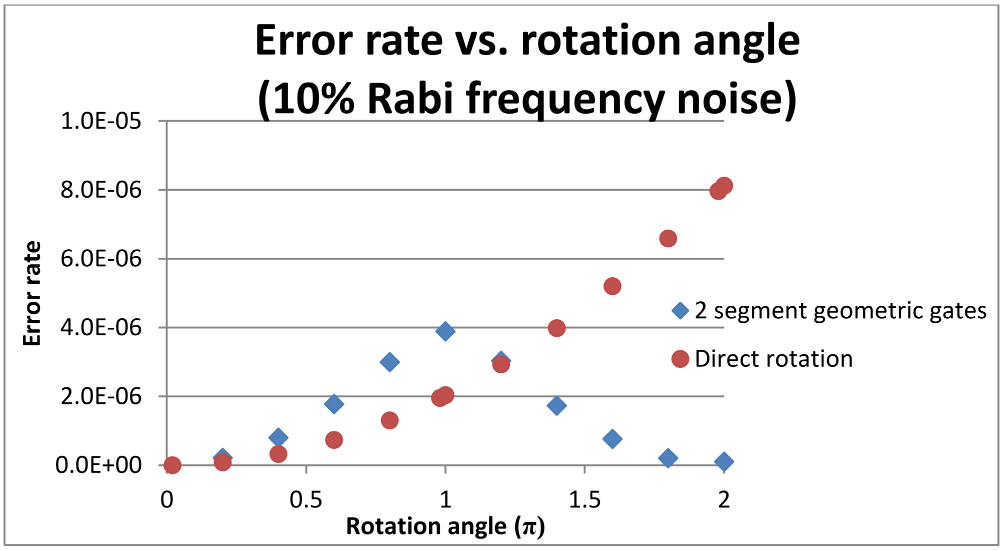

Figure 18-Error rate vs. rotation angle, 10% noise on Rabi frequency.

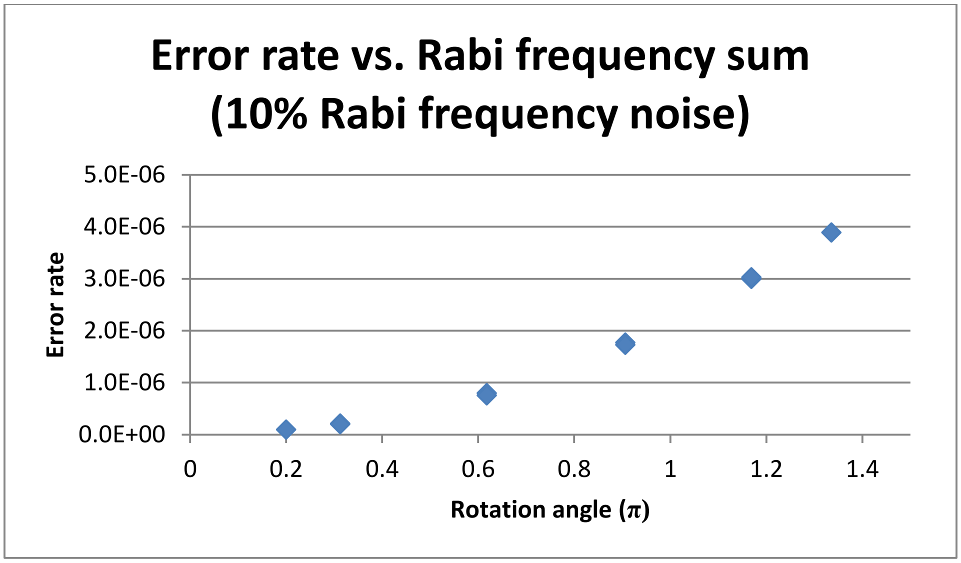

Figure 19-Error rate vs. sum of Rabi frequencies of both segments, with 10% Rabi frequency noise, for 2-segment geometric gates.

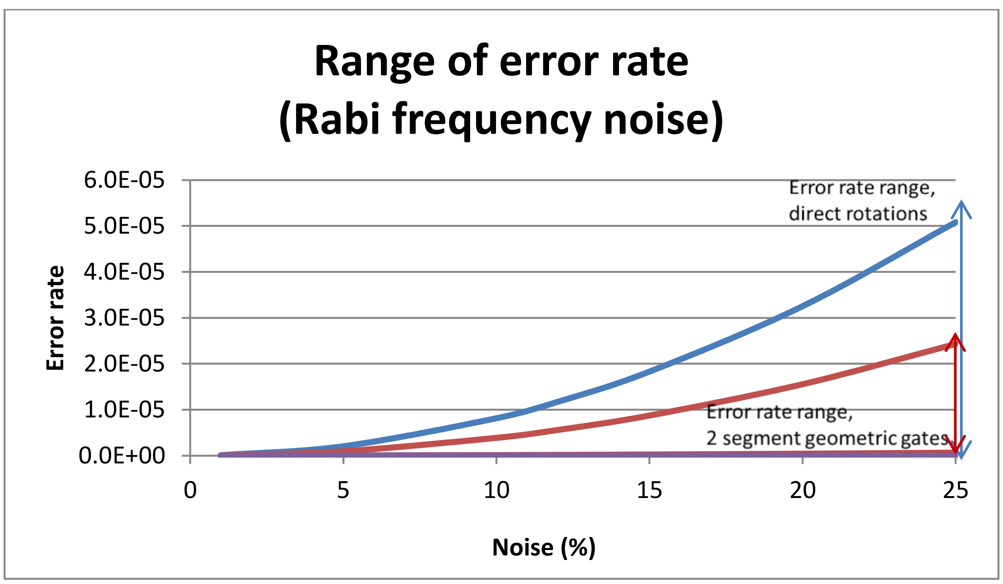

Figure 20-Range of error rates, with different levels of Rabi frequency noise.

The range of error rates for Rabi frequency noise on the paths were similar for this noise model as for the noise on the phase, with the 2-segment geometric gates having a lower error rate range than the direct rotation over the spectrum of noise levels (Figure 20).

Noise on both phase and Rabi frequency

When noise was put on both the phase and Rabi frequency control parameters, the direct rotations were seen to perform almost as well (similar error rates) as the geometric gates for the lower half of the rotation angle spectrum; for the higher rotation angles, geometric gates performed much better than the direct rotations (on the order of 1E-6 error rate instead of on the order or 1E-5; see Figure 21). Once again, there was a correlation between low error rate (high fidelity) and small Rabi frequency (Figure 22), showing that choosing small Rabi frequency for design of geometric gates is optimal for these two types of noise.

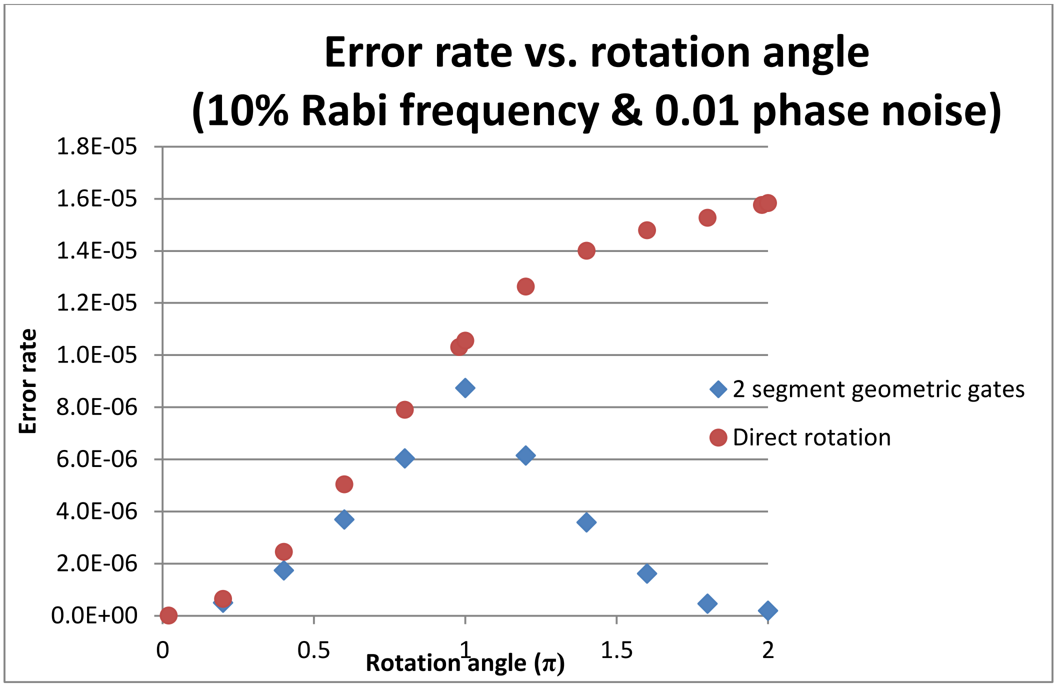

Figure 21-Error rate vs. rotation angle for combination noise: 10% Rabi frequency and 0.01 phase noise.

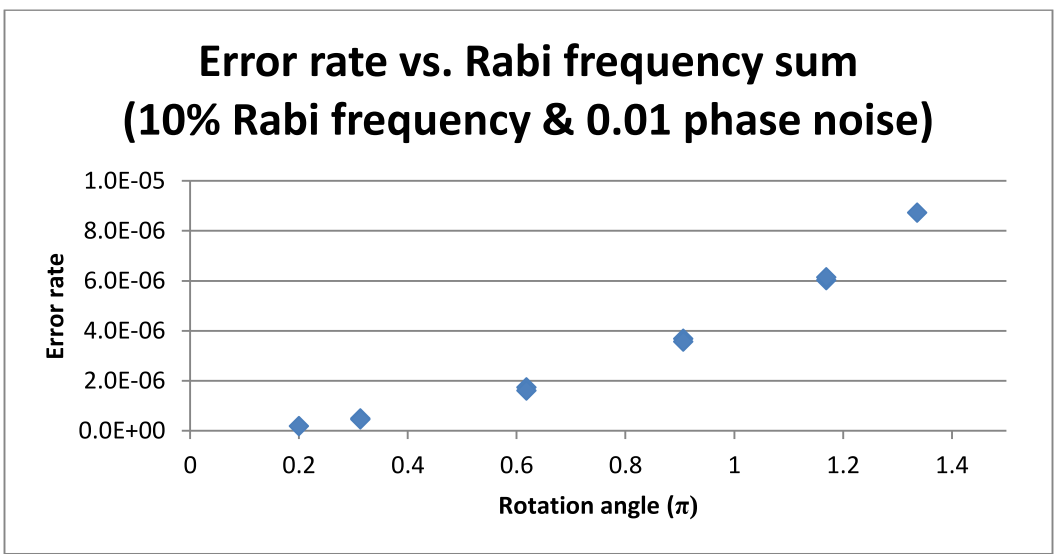

Figure 22- Error rate vs. sum of Rabi frequencies on both segments for geometric gates, combination noise.

Bounds on geometric gates

From our data, we have found that there are both upper and lower bounds on the error rate of the geometric gates (Figure 23), so that increasing increment size when searching for geometric paths will not result in higher (or lower) fidelity geometric gates than found here. This shows that our conclusions when comparing geometric gates to the direct rotations will not change based on a different set of chosen paths.

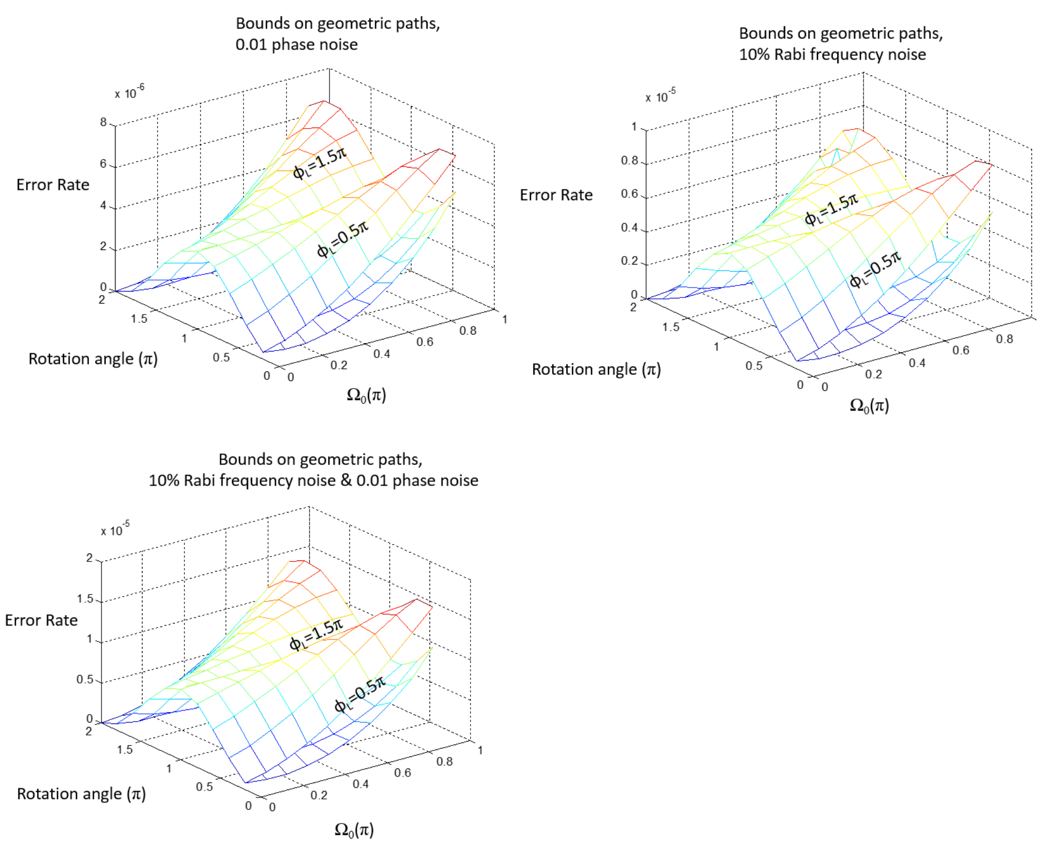

Figure 23-Upper and lower bounds on geometric paths: a) 0.01 noise on phase control parameter, b) 10% noise on Rabi frequency, c) 0.01 phase and 10% Rabi frequency combination noise.

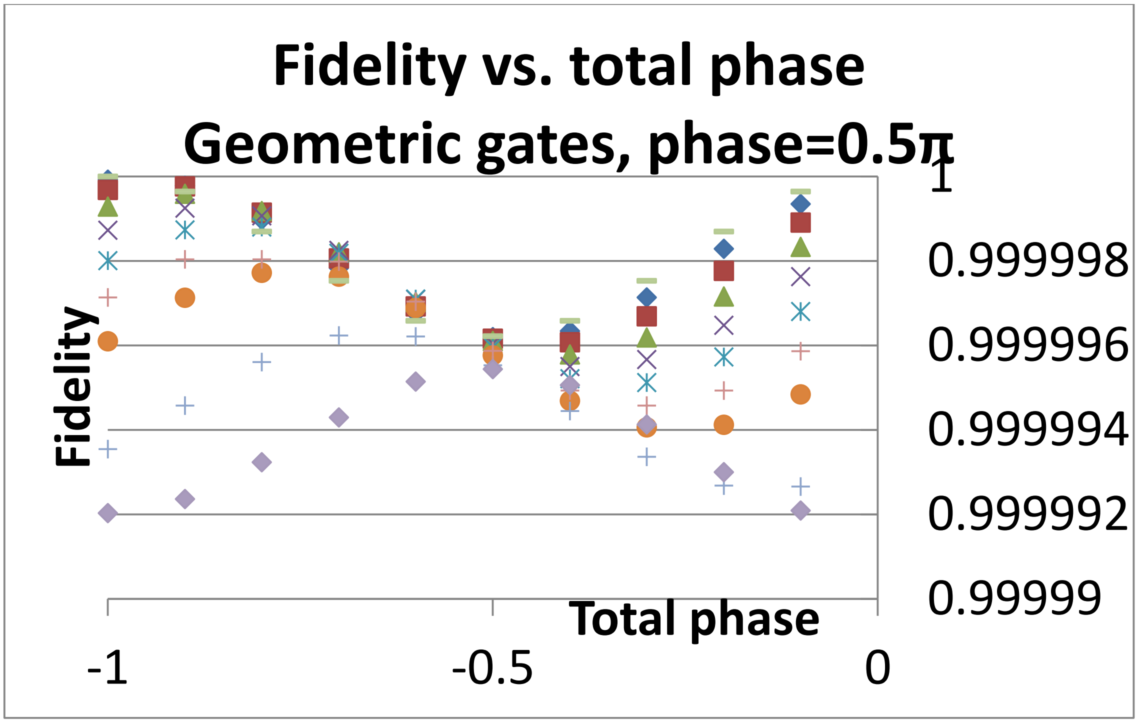

Figure 24- Fidelity vs. total phase for geometric gates of different Rabi frequency values.

Each series in Figure 24 is in 0.1 π increments of the Rabi frequency. This shows that the geometric phase is bounded: if we decrease the increment size that we scan the Rabi frequency with, we expect the fidelities to fall between these curves.

Illustration of geometric and dynamic gates on the Bloch sphere

Since our initial endpoint is on the x-axis, both rotation axes for 1- and 2-segment geometric gates will be in the y-z plane (so that the lab frame phases φ_L and φ_{L2} are 0.5 or 1.5 π). One-segment geometric gates are a full rotation (forming a great circle) around any axis in the x-y plane; an equivalent two-segment geometric gate is shown in Figure 25. One-segment dynamic gates are rotations around the positive or negative x-axis, so that there is no loop (just a point on the x-axis); these are also the only dynamic gates for 2 segments.

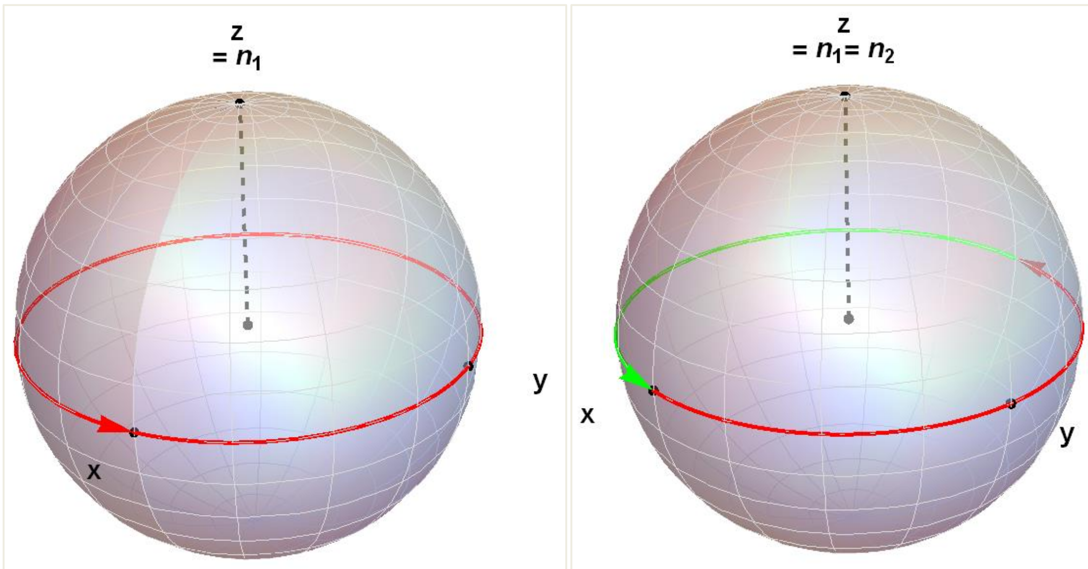

Figure 25- Geometric gates, both with geometric phase = - π: a) one-segment gate; b) 2-segment gate: red = 1st segment; green = 2nd segment; both rotation axes n_1 and n_2 are on dashed line along z-axis.

One of the simplest 2-segment geometric gates is formed by a rotation of π around the z-axis, followed by a rotation of π around the y-axis (see Figure 26a). To make this gate, the control parameters for the first segment would be $\Omega_0 = 0$, $\Delta = \pi$, and φ_L = anything; for the second segment $\Omega_{02} = \pi$, $\Delta_2 = 0$ and $\varphi_{L2} = 1.5\pi$; the angle between bisector of the geodesic and the second rotation axis is $\varphi_2 = 0$. This gate cannot be made in the two-level atom system, since $\Omega_0 = 0$ means that the laser field would be turned off. However, this gate can be made in NMR, since setting Ω_0 to 0 causes the first z-direction magnetic field to vanish, but the nonzero Δ represents a contribution from the second, rotating magnetic field.

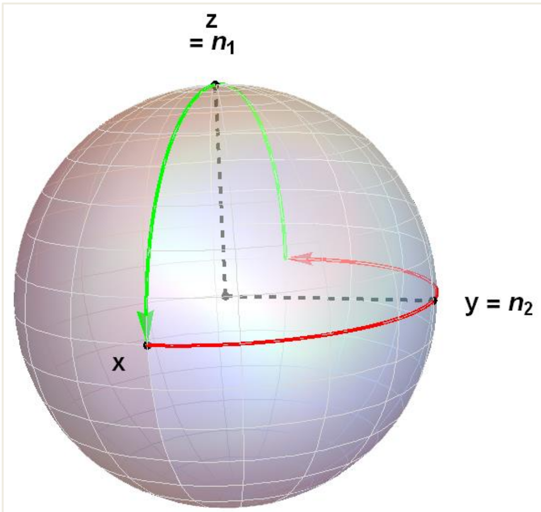

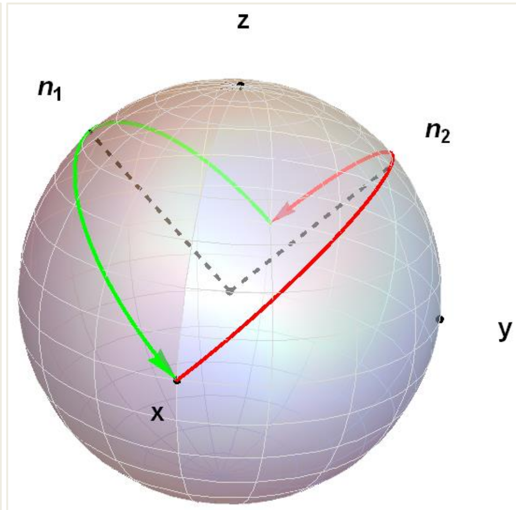

Figure 26- Geometric gates, both with geometric phase = -0.5π: a) first rotation axis n_1 has vanishing Rabi frequency; b) both paths mirrored in x-z plane. First segments are red; second segments are green.

The angle between the two segments of the geometric gates is equal to the geometric phase of the gate. The geometric gates can be made so that both paths are mirrored in the x-z plane: if we choose $\varphi_L = 0.5\pi$, and $\varphi_{L2} = 1.5\pi$, and want to create a gate of total phase = - 0.5π for instance, then our other control parameters will be: $\Omega_0 = \Delta = \Omega_{02} = \Delta_2 = \frac{\pi}{\sqrt{2}}$, and $\varphi_2 = 0$ (see Figure 26b). This gate can be made by all of our 6 physical systems.

Examples of our actual highest fidelity 2-geometric gates are shown in Figure 27, covering the whole range of total phase needed to create any rotation angle gate.

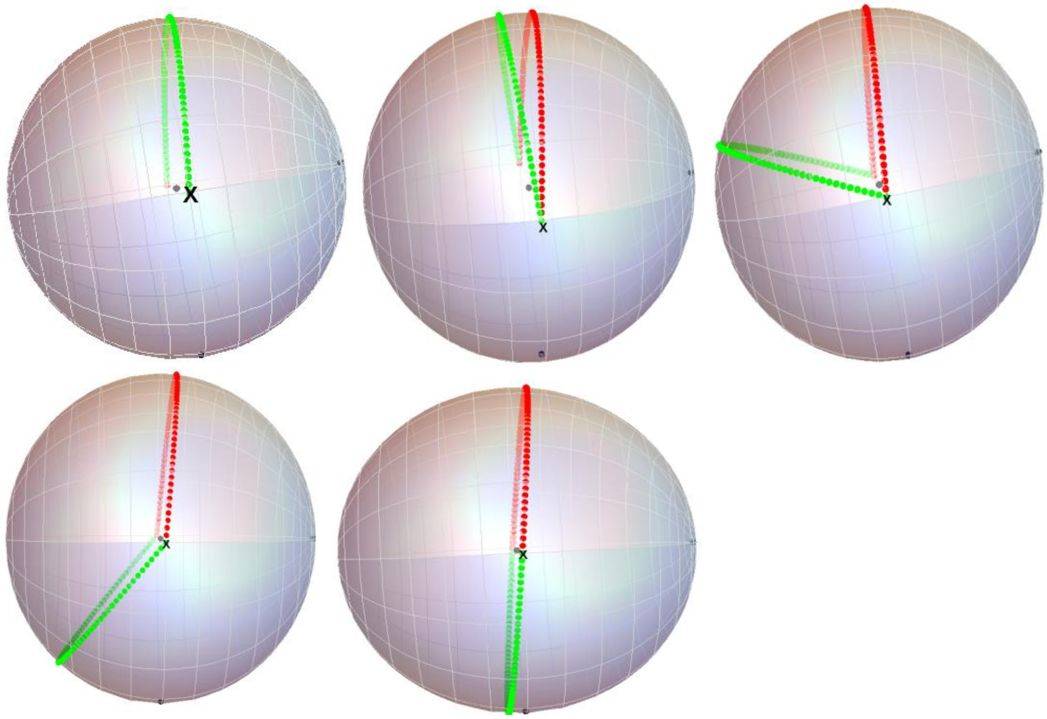

Figure 27-Two-segment geometric gates, showing geometric phase decreasing from 0 to $-\pi$ (first segment (red), second segment (green); second segment of the first gate retraces the first segment).

5.2 Hybrid gates

Gaussian noise on phase

The highest fidelity 2-segment gates across the rotation angle spectrum were hybrid gates; a comparison with geometric gates, with both under 0.01 phase noise, is in Figure 28.

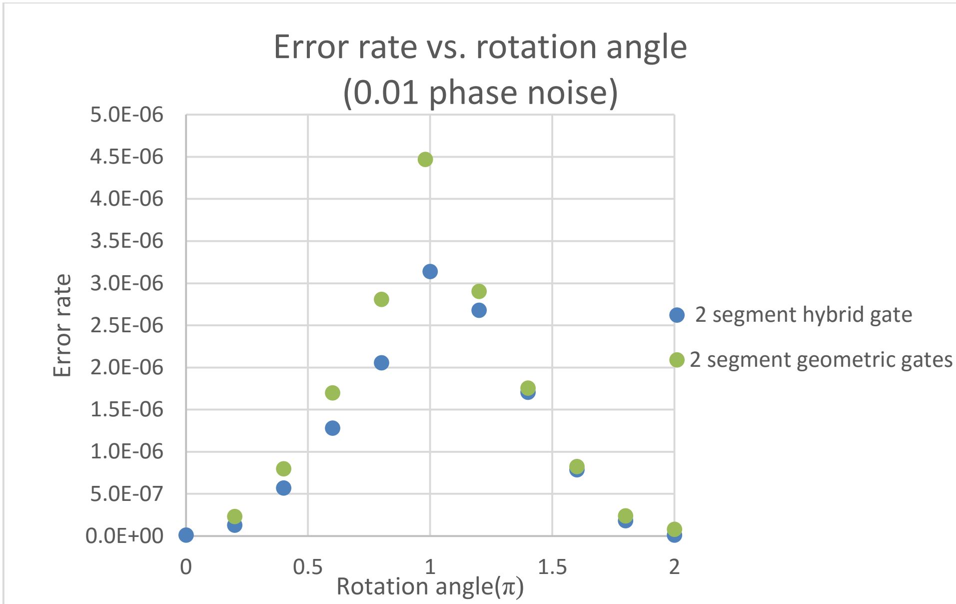

Figure 28- Error rate vs. rotation angle, comparison of hybrid and geometric gates.

Rabi frequency noise

The highest fidelity 2-segment gates across the rotation angle spectrum were again hybrid gates under 10% random noise on the Rabi frequency (Figure 29), with an even more marked improvement over geometric gates.

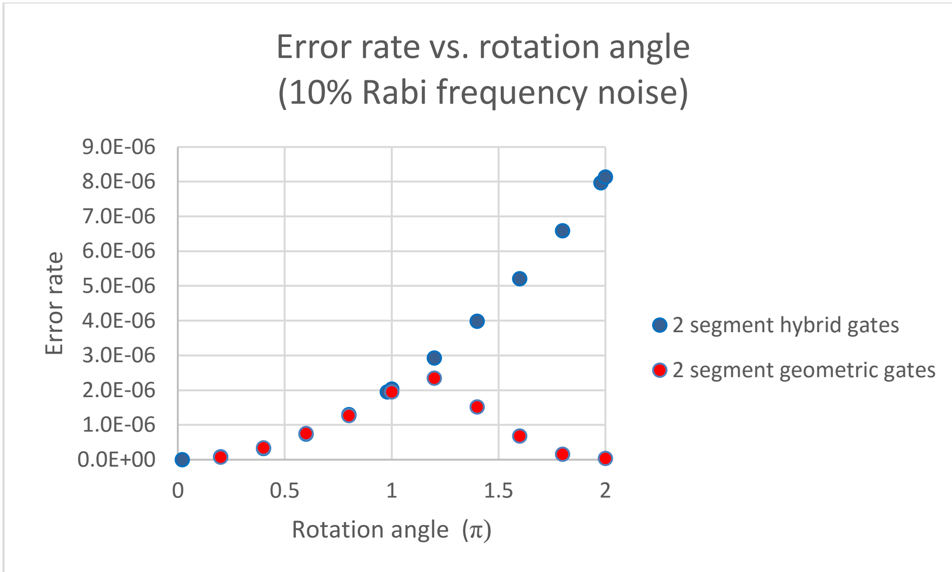

Figure 29- Hybrid vs. geometric gates, for 2-segment rotations and 10% noise on the Rabi frequency.

Combination Rabi frequency and phase noise

When the Rabi frequency noise was combined with the phase noise on our 2-segment gates, we found the hybrid gates to have slightly lower error rates (Figure 30). This improvement seemed to be most similar to the noise only on Rabi frequency, atleast for this noise level.

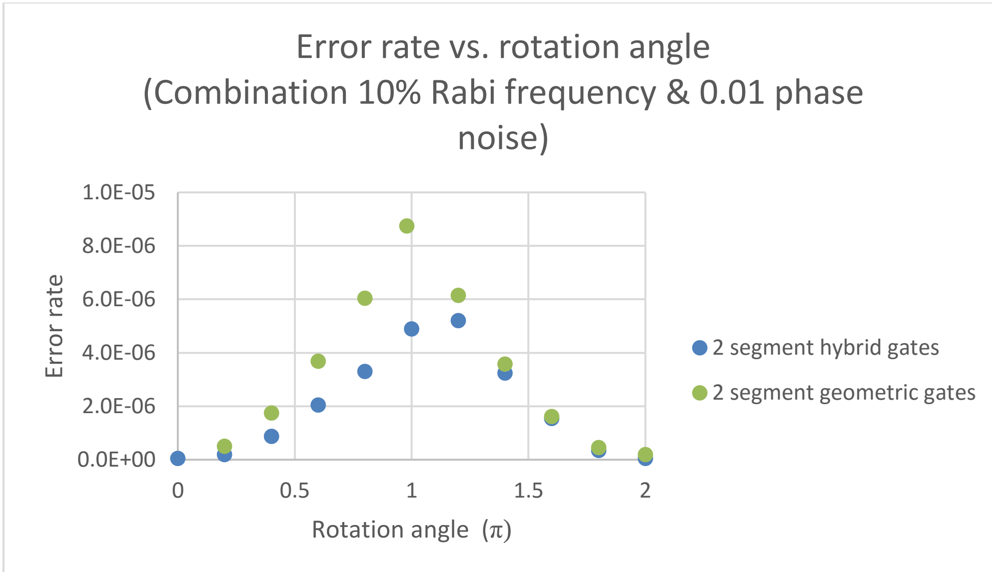

Figure 30- Combination noise on 2-segment gates, 10% Rabi frequency noise and 0.01 phase noise.

Illustration of 2-segment hybrid gates

An illustration of a 1-segment hybrid gates is in Figure 31; this rotation has both a dynamic phase (since the evolution path is not on a great circle) and a geometric phase (since the path encloses a solid angle). A 2-segment hybrid gate is similarly any 2-segment rotation that has atleast 1 non-great circle segment. Examples of the top fidelity (hybrid) gates with 10% Rabi frequency noise are shown in Figure 32; for the first half of total phases (-0.1 π to -0.5 π) the geometric phase is almost 0, and the dynamic phase has the largest contribution to the total phase; this flips for the second half of total phases (-0.6 π to -1.0 π), where the geometric phase is a large contribution to the total phase. Examples of the top fidelity gates with 0.01 phase noise are shown in Figure 33.

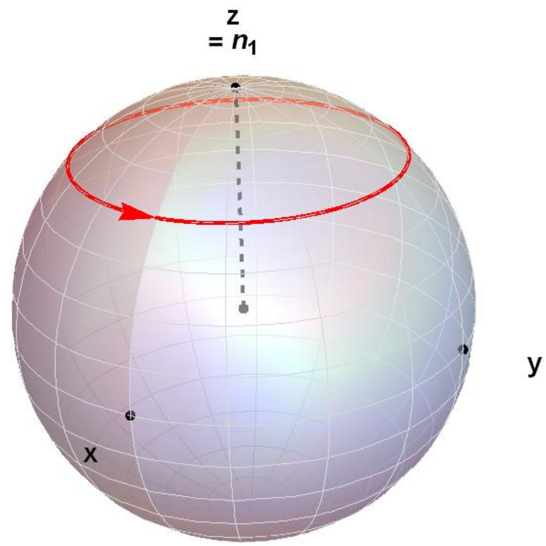

Figure 31- Hybrid gate example: one-segment rotation around z-axis.

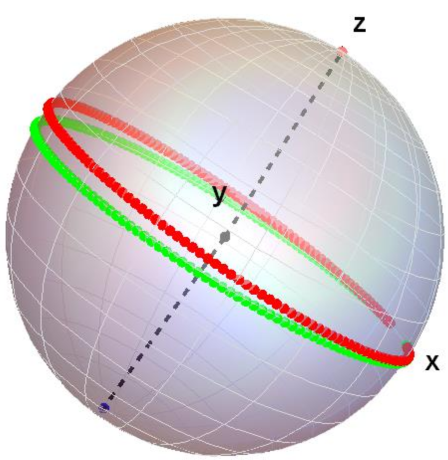

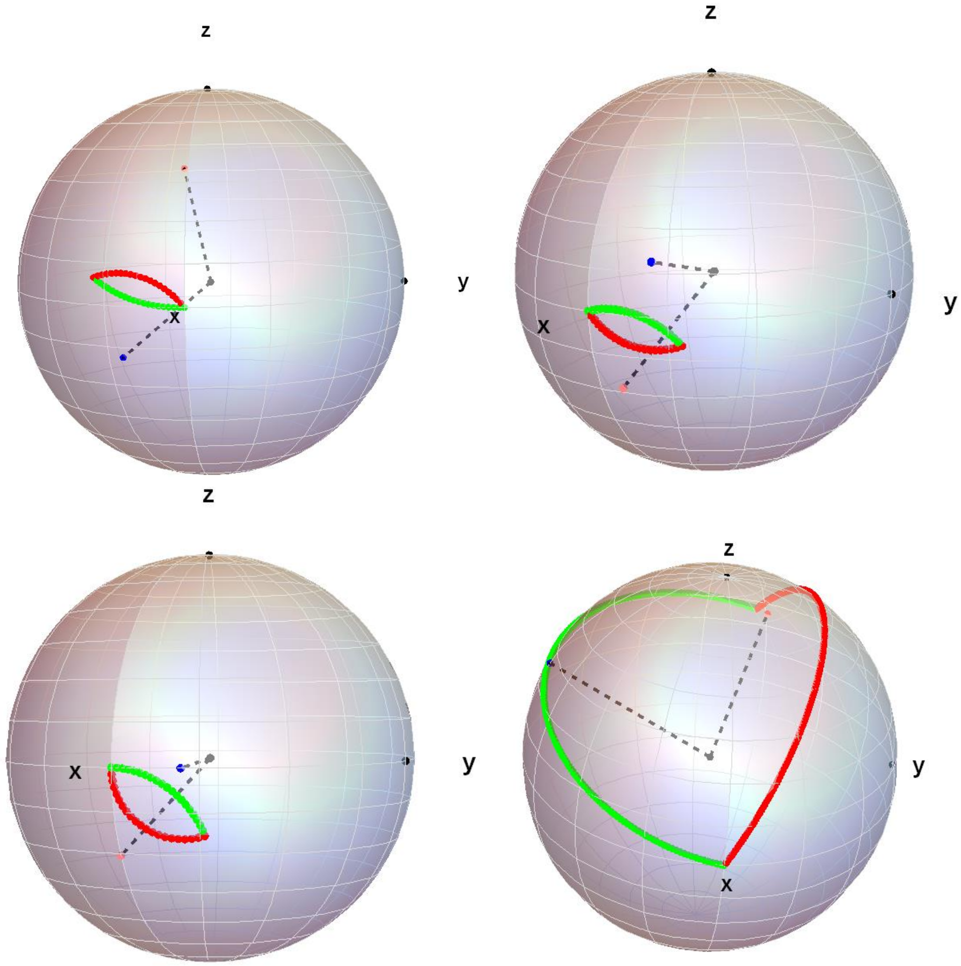

Figure 32-Top fidelity (hybrid) gates for total phase = 0 and -0.3 to -0.6π (in -0.1π increments), 10% Rabi frequency noise. First segment (red), second segment (green); first rotation axis ends at blue dot, second at pink dot.

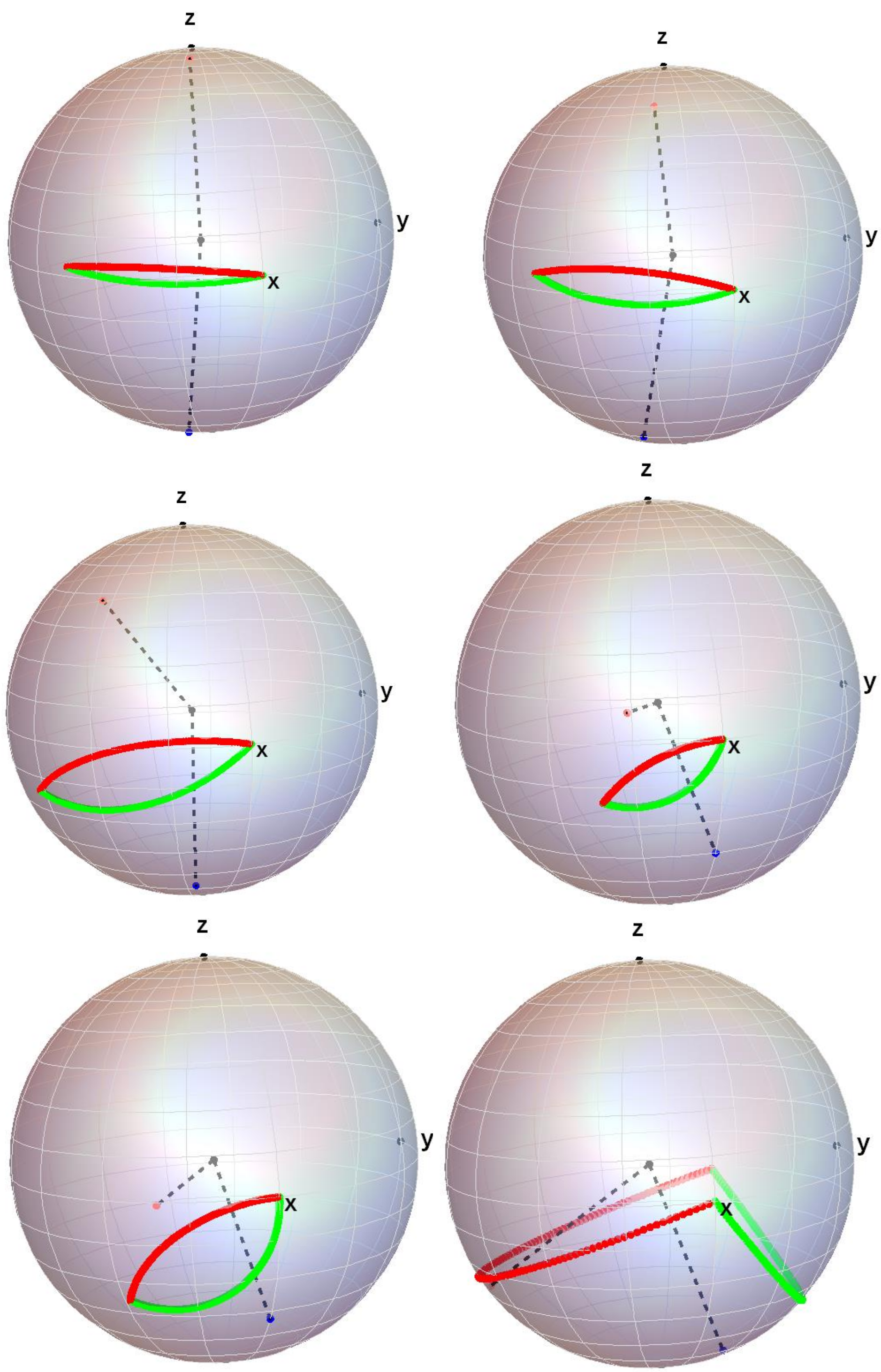

Figure 33- Top fidelity (hybrid) gates under 0.01 phase noise, for total phase = -0.1 π to -0.6π (in -0.1π increments).

5.3 Systematic error

Phase noise

The 2-segment gates and direct rotation performed virtually the same under systematic error on the phase noise, which was created by adding 0.001π to the ideal phase value on each segment (Figure 34). The hybrid gates performed better than the geometric gate under this systematic noise just at π rotation angle, corresponding to a total phase of $-\frac{\pi}{2}$.

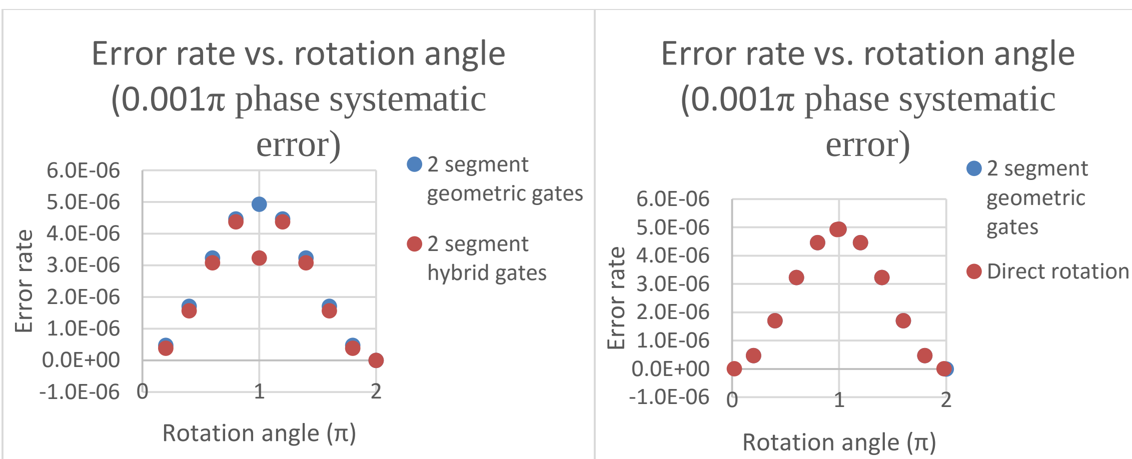

Figure 34-Systematic error, phase noise: a) comparison of hybrid and geometric gates; b) direct rotation vs. geometric gates.

Rabi frequency noise

Under Rabi frequency 1% systematic error, the 2-segment geometric gates again had slightly higher error rates than the hybrid gates; the 2-segment gates had much better error rates than direct rotations over large rotation angles (Figure 35).

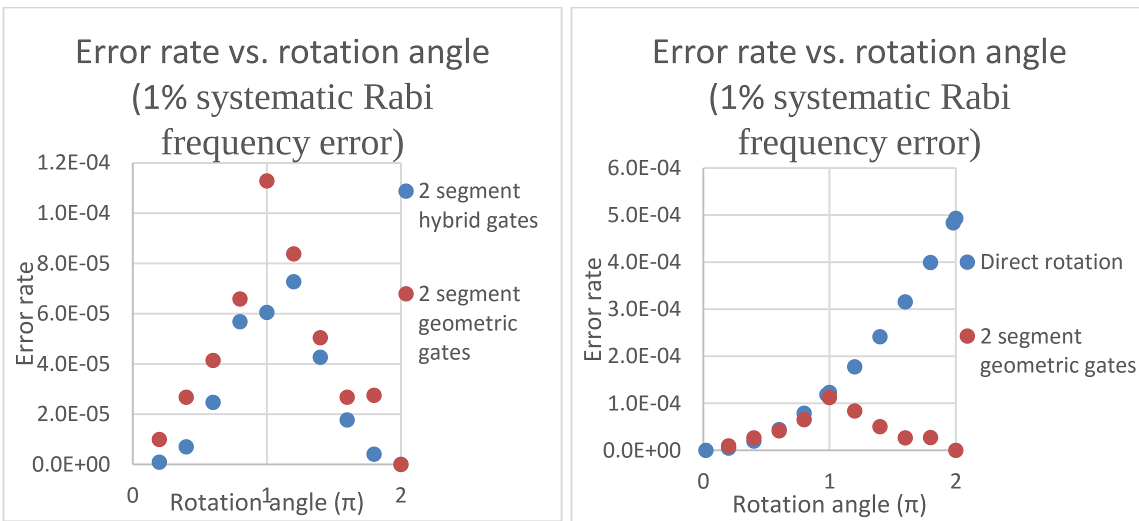

Figure 35-Error rate vs. rotation angle, 10% systematic error on Rabi frequency: a) comparison of hybrid and geometric gates; b) comparison of direct rotation to 2-segment geometric gates.

CHAPTER 6- THREE-SEGMENT ROTATION RESULTS

This section presents our data results when we create the gates for a given total phase using 3-segment rotations on the Bloch sphere.

6.1 Noise on phase

The 3-segment rotations were scanned in a small region of the control parameter space, assuming that there will be symmetries in the control parameter quadrants. Under 0.01 phase noise, we found significant improvement in error rates for the highest fidelity 3-segment (hybrid) gates compared to 2-segment (highest fidelity, hybrid) gates (Figure 36), over the spectrum of rotation angles. The 3-segment hybrid gates again had lower error rates than the highest fidelity 3-segment geometric gates (Figure 37); 3-segment geometric gates performed better than the 2-segment geometric (Figure 38).

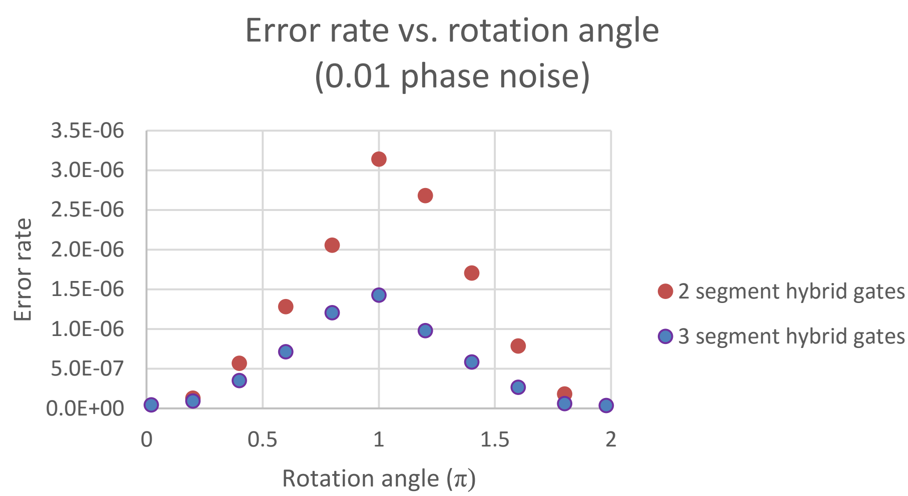

Figure 36-Comparison of 2- and 3-segment highest fidelity hybrid gates, under 0.01 phase noise.

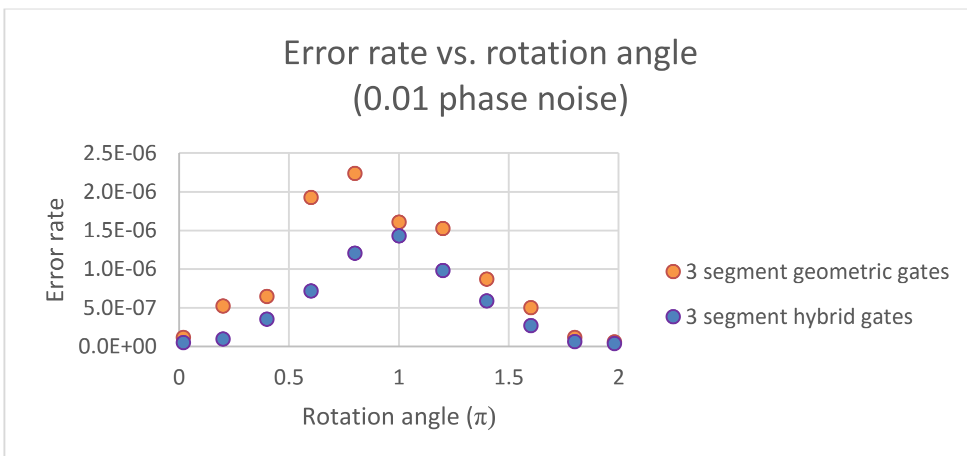

Figure 37- Comparison of 3-segment hybrid and geometric gates.

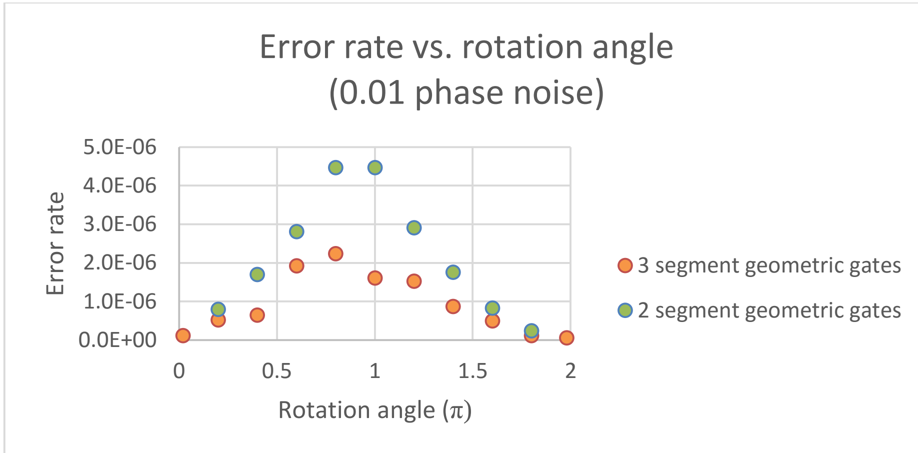

Figure 38-Comparison of 2- and 3-segment geometric gates.

There was again a correlation between small Rabi frequency and the highest fidelity gates for 3 segments (Figure 39).

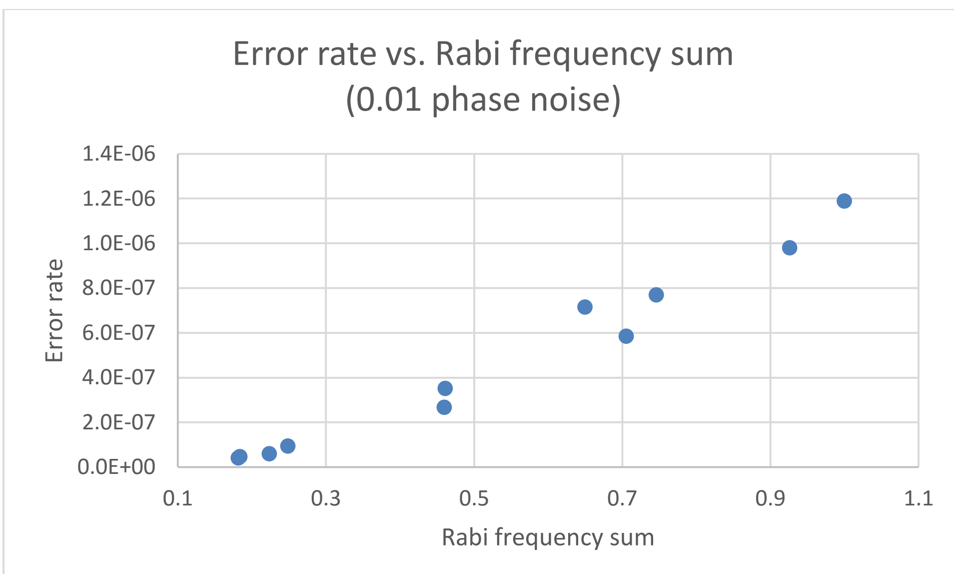

Figure 39-Error rate vs. sum of Rabi frequencies for 3 segments, using 0.01 phase noise.

6.2 Rabi frequency noise

Just as in the 2-segment case, 3-segment hybrid gates have better error rates than geometric gates (Figure 40). When comparing the highest fidelity (hybrid) 2- and 3-segment gates under this noise, the 2-segment gates perform better for the lower half of rotation angles, and vice versa for the higher rotation angles (Figure 41).

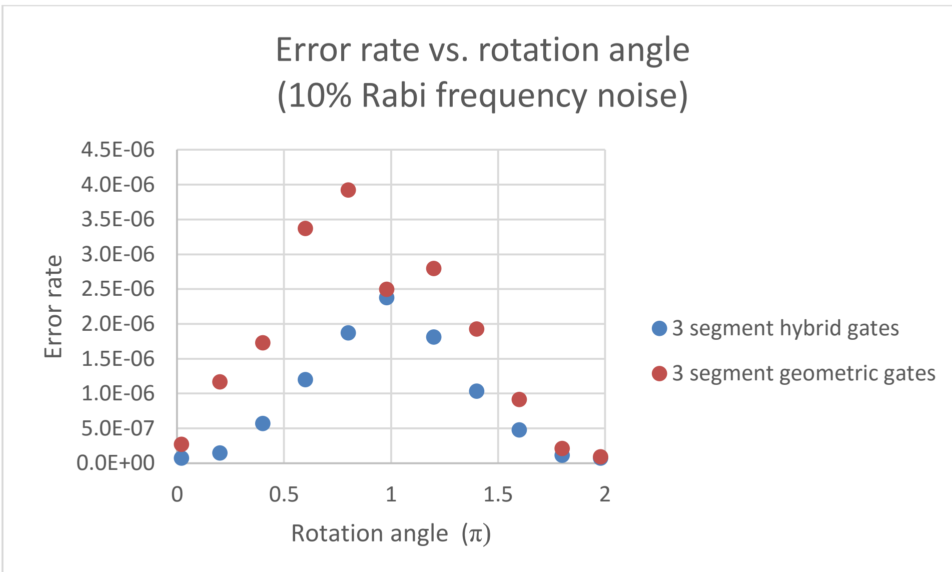

Figure 40- Error rate vs. rotation angle, 10% noise on Rabi frequency: comparison of hybrid and geometric gates for 3-segment rotations.

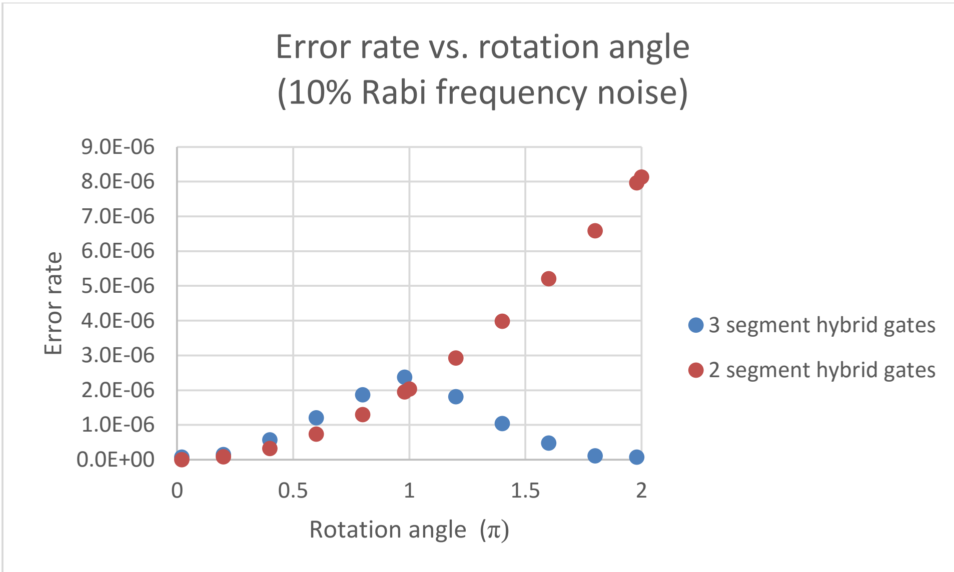

Figure 41- Comparison of 2- and 3-segment highest fidelity (hybrid) gates, with 10% noise on Rabi frequency.

The correlation between small Rabi frequency (summed over all 3 segments) and a lower error rate again held in this case (Figure 42).

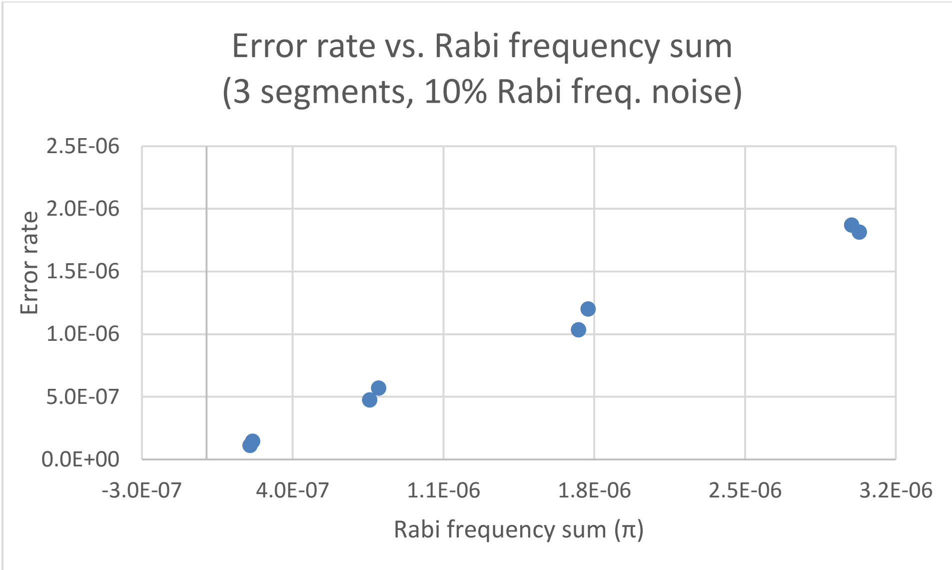

Figure 42- Correlation of small Rabi frequencies and error rate, 3-segment rotations and 10% Rabi frequency noise.

6.3 Combination noise

The 3-segment gates under a combination of 10% Rabi frequency and 0.01 phase noise are shown in Figure 43 and Figure 44, with basically the same features. The phase noise acts to lift the error rate of other gates compared to our 3-segment highest fidelity hybrid gates, whereas the Rabi frequency noise effectively shifts the error rate pattern so that the peak is at lower rotation angles.

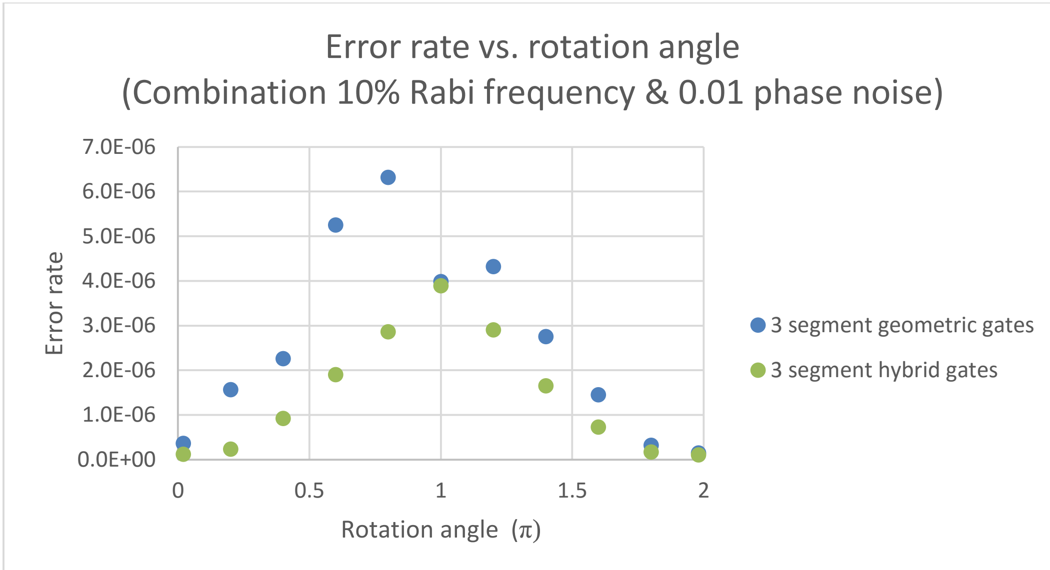

Figure 43- Combination noise on 3 segments.

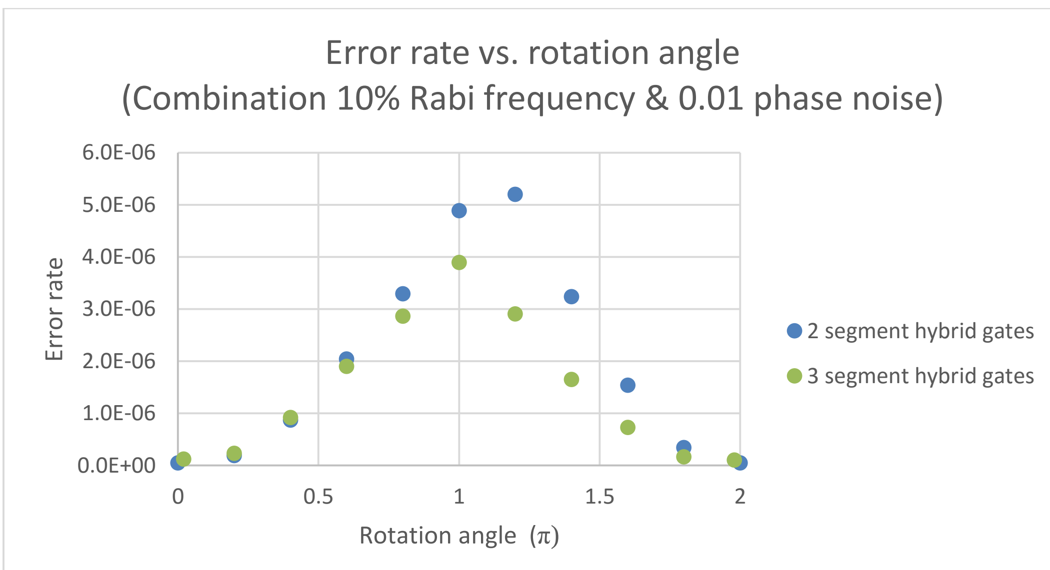

Figure 44- Comparison of 2- and 3-segment gates under combination noise.

6.4 Systematic error

Phase noise

Unlike in the 2-segment case, the 3-segment rotations under 0.001π systematic phase error showed a significant improvement in error rates for hybrid gates compared to geometric gates, and for 3-segment hybrid gates compared to 2-segment hybrid gates (Figure 45). This may have to do with the fact we are placing the systematic error on each segment, but if there are more segments, there will be some gates that have the final endpoint less far from the initial endpoint under systematic noise, if some segments' systematic noise partially compensate for the other segment noise.

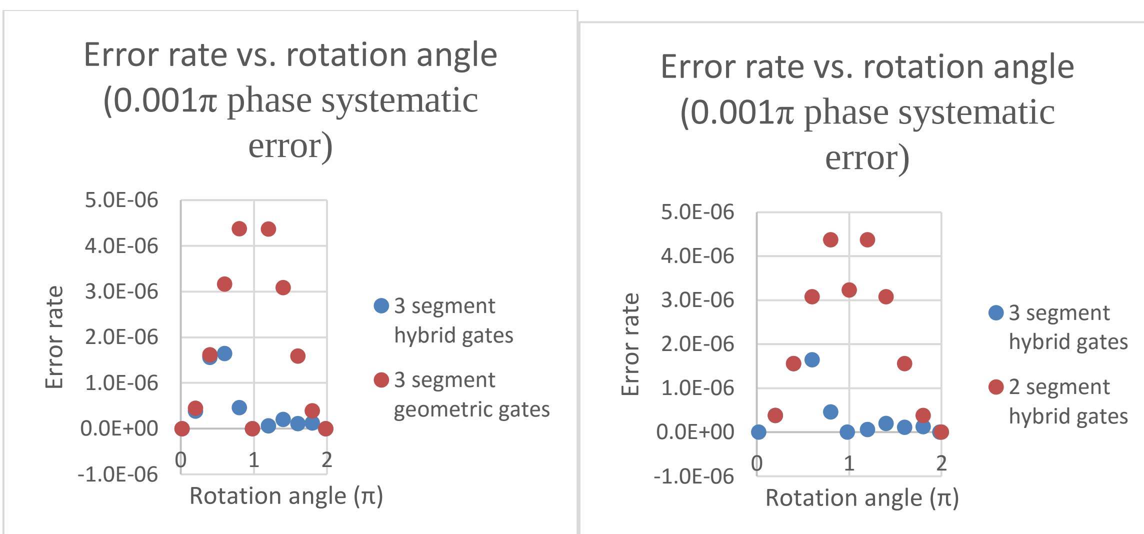

Figure 45- Systematic error of 0.001π on phase: a) comparison of 3-segment hybrid and geometric gates; b) comparison of 2- and 3-segment highest fidelity (hybrid) gates.

Rabi frequency noise

The 3-segment gates with 1% systematic Rabi frequency noise showed the same trend as in the 2-segment case: the hybrid gates had lower error rates than the geometric gates, as well as the 2-segment maximum fidelity (hybrid) gates (Figure 46).

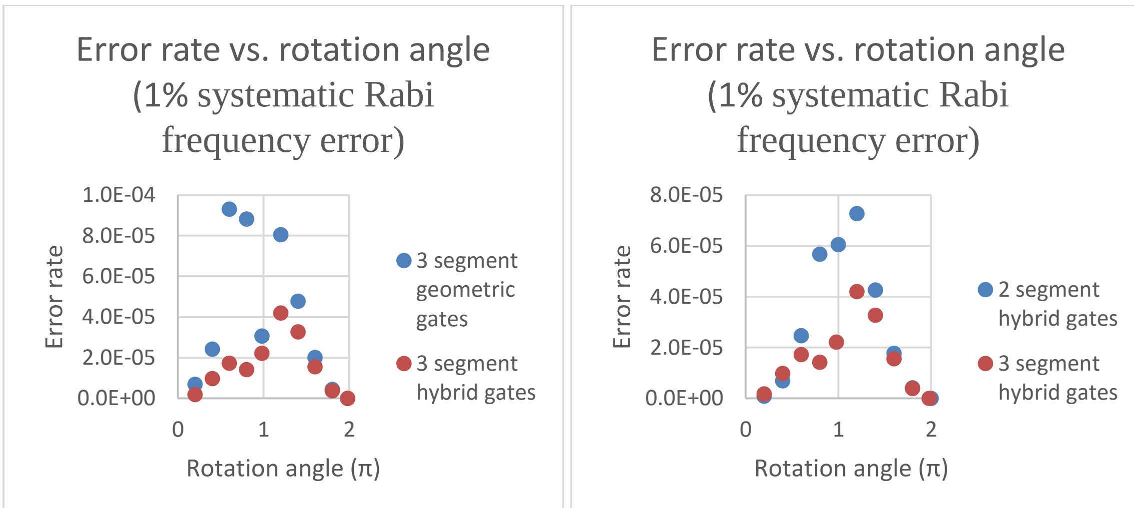

Figure 46-Systematic error of 1% on Rabi frequency: a)comparison of 3-segment hybrid and geometric gates; b) comparison of 2- and 3-segment hybrid gates.

6.5 Illustration of 3-segment hybrid, dynamic and geometric gates

A 3-segment geometric gate is illustrated in (Figure 50), which has a geometric phase of -$\frac{\pi}{4}$. It is created by a $\frac{\pi}{2}$ rotation around the z-axis, followed by a $\frac{\pi}{2}$ rotation around the x-axis, and finally a $\frac{\pi}{2}$ rotation around the y-axis. Similarly, any N-segment geometric gate can be made from N segments on great circles.

For 3 and higher segments, there is the possibility of paths that cross each other: an example of a 3-segment hybrid gate is in Figure 47. The loop on the left side has a (-) geometric phase due to the counterclockwise orientation of the segments; the loop on the right side has a (+) geometric phase. If the areas (+) and (-) are equal, then the geometric phases cancel each other (since the counterclockwise path has negative geometric phase, and the clockwise has positive geometric phase), and the gate becomes a purely dynamic gate.

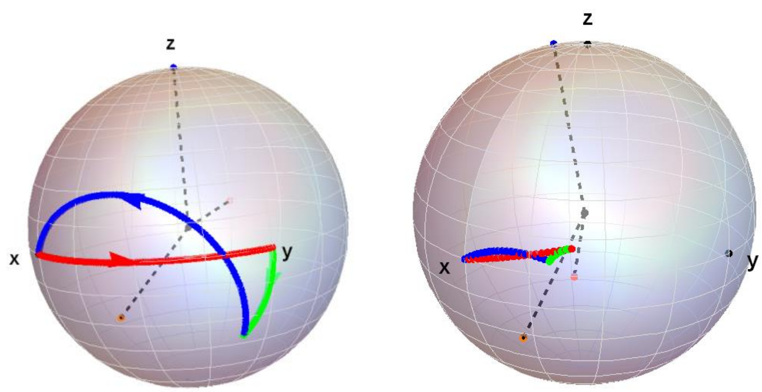

Figure 47- a) Example of a 3-segment hybrid gate: first segment (red), second segment (green), third segment (blue); b) actual 3-segment gate: the geometric phase almost completely vanishes, making this an almost purely dynamic gate.

Other highest fidelity 3-segment gates for a couple total phase values are shown in Figure 48; the paths tended to be very small rotations for lower absolute value total phase, and had larger enclosed geometric areas starting at total phase of -0.4π and for all larger absolute values. For lower values of (absolute value) total phase the dynamic phase was almost equal to the total phase, with the geometric phase almost vanishing; this reversed for higher total phase values.

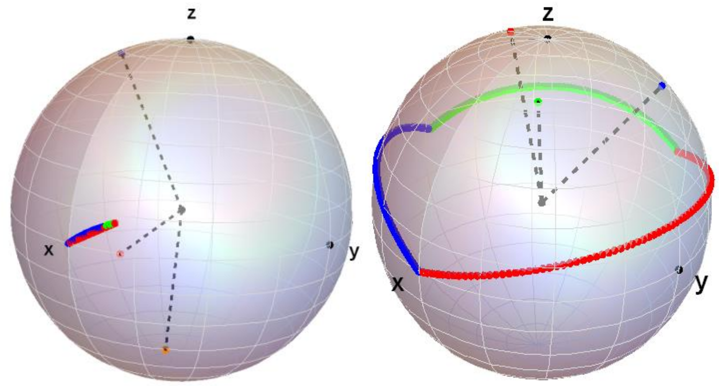

Figure 48- Highest fidelity 3-segment gates, 10% Rabi frequency noise: total phases shown are (l-r): -0.1 and -0.6 π.

Examples of our highest fidelity three-segment geometric gates are in Figure 49.

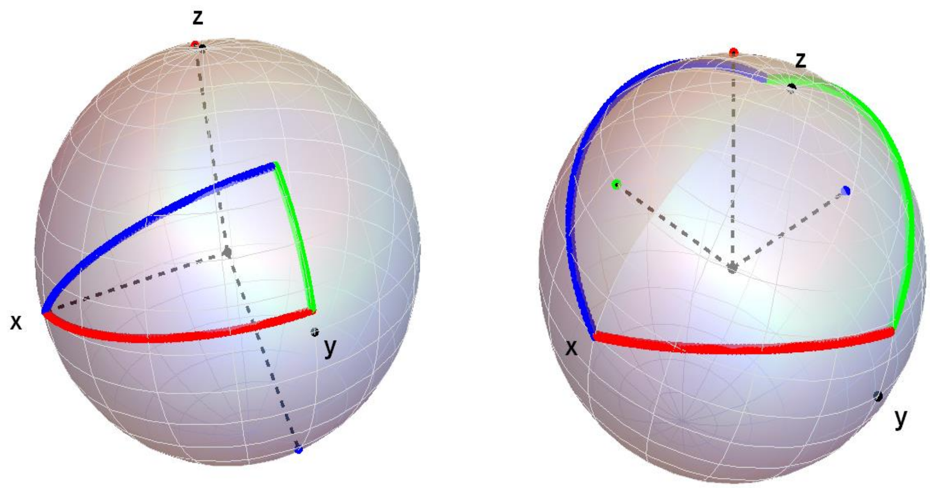

Figure 49- Three-segment geometric gates: a) total phase = -0.2 π; b)total phase = -0.5 π.

CHAPTER 7- CONCLUSIONS

7.1 Highest fidelity gates from composite hybrid gates

Our research has shown that hybrid gates have higher fidelity under random noise than geometric or dynamic gates. The composite (multiple segment) rotations had significantly higher fidelities than the direct (single segment) rotations. This was true for all types of random noise studied here, and for both two- and three-segment gates.

For systematic error on the Rabi frequency, hybrid gates again have higher fidelity than geometric or dynamic gates, and 3-segment hybrid gates performed better than 2-segment hybrid gates. For 2 segments, systematic error on the phase produced virtually the same fidelities for the different types of gates. But at 3-segment phase systematic error, the hybrid gates have much higher fidelities than the 2-segment hybrid gates or the 3-segment geometric gates. Therefore, for large systematic error, it appears to be better to use a higher N hybrid gate.

7.2 Improvements with 3 and higher segment paths

Under phase noise, the maximum fidelity three-segment gates had higher fidelities than the maximum fidelity two-segment gates, which leads us to suspect that high N-segment rotations will lead to higher fidelities.

However, under Rabi frequency noise, the 3-segment gates had higher fidelities only on the largest half of rotation angles, with 2-segment gates having higher maximum fidelities on the smaller half of rotation angles (Figure 41). In that figure, the form of the error rate across the rotation angle spectrum is like an upside down V for both 2- and 3-segments, with the 3-segment peak shifted to left (at lower rotation angle). For further work, it would be interesting to see if this trend continues into higher N-segment rotations: if so, under this type of noise, the number of segments in the best designed path may depend on the rotation angle (i.e. total phase) of the particular gate.

7.3 Small Rabi frequencies

The highest fidelity paths tended to have very small Rabi frequencies. This was seen to be true across all different noise types and levels, and for both 2- and 3-segment rotations. The reason for this result is that the Rabi frequency multiplies the cosine and sine of the phase in the Rabi vector; if the Rabi frequency is small, then the phase noise is not amplified as it would be otherwise. And similarly, when the noise is on the Rabi frequency itself, if the Rabi frequency is small, then the percentage noise is also small.

APPENDIX A- MAZONKA'S EQUATIONS

This appendix contains some of the key results needed from Mazonka (2011), which are used to derive the equations for two-segment rotations on the Bloch sphere.

A conical surface is made by drawing a cone inside a sphere, with the cone's apex at the sphere's origin. The sphere can be projected onto the unit sphere. The intersection of the cone and the sphere forms a closed parametric curve, parameterized by l, which can be thought of as the length along the curve from the point where l=0. A curve on the sphere is given by $\vec{s}(l)$, which is a vector from the origin to a point on the curve. The speed this point moves along the curve is given by

$$\vec{\tau} = \frac{d\vec{s}}{dl} \quad \textbf{(234)}$$

and the acceleration is given by

$$\vec{u} = \frac{d^2\vec{s}}{dl^2} \quad \textbf{(235)}$$

These two vectors are not defined at corners between segments.

We call δ_i the turn angle of corner i, which is the outside angle formed from the evolution path of two segments. Two tangent vectors are defined at the corner: one tangent to the 1st segment traversed (τ-), and one tangent to the 2nd segment traversed (τ+). These tangent vectors can be used to find the turn angle:

$$\tan \delta_i = \sin \delta_i / \cos \delta_i = |\tau^+_i \text{ X } \tau^-_i| / \tau^+_I * \tau^-_I \quad \textbf{(236)}$$

(taking the cross product of the tangent vectors and dividing by the dot product (*) of the tangent vectors gives the tangent of the turn angle), since by definition of the cross and dot products:

$$\tau^+_i \, X \, \tau^-_i = |\tau^+_i| \, |\tau^-_i| \sin \delta_i \, \hat{n} \tag{237}$$

$$\tau^+_I * \tau^-_i = |\tau^+_i| \, |\tau^-_i| \cos \delta_i \tag{238}$$

and solving for the turn angle:

$$\sin \delta_i = |\tau^+_i \, X \, \tau^-_i| / (|\tau^+_i| \, |\tau^-_i|) \tag{239}$$

$$\cos \delta_i = (\tau^+_I * \tau^-_i) / (|\tau^+_i| \, |\tau^-_i|) \tag{240}$$

Dividing the two above equations gives the equation above for the tangent of the turn angle.

The equation for the solid angle of a conical surface is:

$$\Omega = 2\pi - \sum_i \delta_i - \oint dl \sqrt{\vec{u}^2 - (\vec{s} \cdot \vec{u})^2} \tag{241}$$

where the sum is over all "i" corners (outside angle of the traversed curves), and the line integral is along the closed curve except at corners. The integral term above vanishes along great circle, i.e.

$$\oint dl \sqrt{\vec{u}^2 - (\vec{s} \cdot \vec{u})^2} = 0 \tag{242}$$

If s is made of n great circles, then we have a spherical polygon, and the solid angle is

$$\Omega = 2\pi - \sum_i^n \delta_i \; = \sum_i^n \{(\pi - \delta_i) - (n-2)\pi\} \tag{243}$$

There are an infinite number of spherical polygons that give the same solid angle (and therefore the same geometric phase).

Another result used in our work is Girard's Theorem for the area of a spherical triangle. This is found by summing the angles, and subtracting π (where we have used that the radius of the Bloch sphere = 1). The angle between 2 great circles was found from the angle between tangents to the great circles. For spherical polygons of N segments, the area is given by the sum of the angles, subtracted by (N-2) π.

APPENDIX B- GEOMETRIC PHASE

Quantum geometric phase occurs when the quantum state vector evolves around a loop on a curved surface representing all the possible states. The final quantum state vector is then equal to the initial vector multiplied by a phase factor that includes a geometric phase depending only on the global geometry of the space. Whenever quantum system evolution leads to a geometric phase, the state vector in effect holds a memory of the evolution taken. By exploiting this memory, geometric phase can be used to construct quantum gates for quantum computation.

Berry phase

Berry was the first to discover quantum geometric phase in 1984. Berry's phase requires adiabaticity, in which the evolution of the state is slow enough that the system stays in an eigenstate of the Hamiltonian.

Berry's phase occurs under the condition of slow evolution, so that the adiabatic theorem holds: a system initially in an eigenstate of the static Hamiltonian remains in an eigenstate of the Hamiltonian if the Hamiltonian is varied slowly. Using the Schrodinger equation,

$$H\psi = i\hbar\frac{\partial\psi}{\partial t} \quad \textbf{(244)}$$

where H depends on parameters R: H = H(R(t)). The system is driven around a closed path in the parameter space by varying the parameters R in time.

The eigenvalue equation is

$$H(R)|n> = E_n (R)|n> \quad \textbf{(245)}$$

where R = R(t) and |n> = |n(R(t))>are the instantaneous eigenstates of the Hamiltonian.

The state evolves with both a dynamic phase and a geometric phase:

$$|\psi(t)>= \exp\left[\frac{-i}{\hbar}\int_0^{t'} dt' E_n(R(t'))\right]\exp\{i\gamma_n(t)\}|n(R(t))> \quad \textbf{(246)}$$

Inserting this expression for the state into the Schrodinger equation, we can solve for the geometric phase in terms of the eigenstates |n>. The final result is that the geometric phase is

$$\gamma_n(C) = i\oint < n(R)|\nabla_R n(R)> \cdot dR \quad \textbf{(247)}$$

which shows that the geometric phase depends only on the geometry of the loop in parameter space (R-space), and is independent of time.

This result can be extended to degenerate eigenstates |n(R)> by using Stokes theorem to eliminate the dependence on $|\nabla n>$. The Berry phase becomes

$$\gamma_n(C) = -\operatorname{Im}\iint_C dS \cdot \sum_{m\neq n}\frac{< n|\nabla H|m> \times < m|\nabla H|n>}{\left(E_n - E_m\right)^2} \quad \textbf{(248)}$$

where dS is an element of area in parameter space.

The special case of a two-level system with an evolution loop C close to a degeneracy at R = 0 has a simple form for the calculation of the Berry phase. If there are two degenerate states |+> and |->, both having energy E =0 at R = 0, then |+> and |-> replace |n> and |m> in equation (248). The Berry phases for the orthogonal states are opposite: $\gamma_+(C) = -\gamma_-(C)$. The standard Hamiltonian for this 2-level system with parameter vector **R** = (a, b, c) is

$$H(R) = \frac{1}{2}\begin{pmatrix} c & a-ib \\ a+ib & -c \end{pmatrix} = \frac{1}{2}(a\sigma_X + b\sigma_Y + c\sigma_Z) \tag{249}$$

where σ_X, σ_Y, σ_Z are the Pauli matrices. The gradient of H is

$$\nabla H = \frac{\partial H}{\partial a} + \frac{\partial H}{\partial b} + \frac{\partial H}{\partial c} = \frac{1}{2}(\sigma_X + \sigma_Y + \sigma_Z) = \frac{1}{2}\vec{\sigma} \tag{250}$$

and the energy eigenvalues are

$$E_+(R) = -E_-(R) = ½\,(a^2 + b^2 + c^2)^{½} = ½\,R \tag{251}$$

For any two-level system, the Berry phase is given by

$$\gamma_+ = -½\,\Theta \tag{252}$$

where Θ is the solid angle enclosed by the curve that the parameter vector **R** traces out in parameter space, subtending the degeneracy or **R** = 0 point. This is the effect on the positive or up basis state; the negative or down basis state obtains a phase equal to + ½ Θ.

Aharonov-Anandan phase

Aharonov-Anandan (AA) phase is a nonadiabatic geometric phase; evolutions of the quantum state can occur quickly (unlike in the adiabatic, Berry phase). The possibility of creating fast quantum gate times makes AA phase more desirable for quantum computing than Berry phase.

In contrast to Berry phase, where an eigenstate evolves adiabatically on a closed loop made in parameter space, the Aharonov-Anandan (AA) phase, or nonadiabatic geometric phase, occurs when a state vector makes a closed loop in the projective Hilbert space. AA phase is critical for making high quality quantum gates, since the need for the slow-varying (adiabatic) condition is eliminated.

As before with the Berry phase, the state evolution follows the Schrodinger equation, and the wavefunction at the end of the evolution is a phase factor times the initial wavefunction. The evolution of the state |ψ(t)> defines a curve C in the Hilbert space. The projection of this curve to the projected Hilbert space is a closed curve $\hat{C}$.

A phaseless state can be defined as

$$|\tilde{\psi}(\mathrm{t})> = \exp\{-\mathrm{if}(\mathrm{t})\}|\,\psi(\mathrm{t})> \tag{253}$$

where f(τ) –f(0) = φ = total phase, so that the phaseless state is cyclic: $|\,\tilde{\psi}(t)>=|\,\tilde{\psi}(0)>$. Substituting the wavefunction in terms of the new phaseless wavefunction into the Schrodinger equation, we get

$$-\frac{df}{dt} = \frac{1}{\hbar} < \psi(t)\,|\,H\,|\,\psi(t) > - < \tilde{\psi}(t)\,|\,i\frac{d}{dt}\,|\,\tilde{\psi}(t) > \tag{254}$$

Removing the dynamical phase from the total phase results in the Aharonov-Anandan (AA) phase (geometric phase):

$$\gamma \equiv \phi + \frac{1}{\hbar}\int_0^{\tau} < \psi(t)\,|\,H\,|\,\psi(t) > dt \tag{255}$$

Combining the above two equations, the AA phase becomes

$$\gamma \equiv \int_0^{\tau} < \tilde{\psi}\,|\,i\frac{d}{dt}\,|\,\tilde{\psi} > dt \tag{256}$$

For 2-level systems such as a spin-1/2 particle, the projective Hilbert space is the Bloch sphere and the evolution of the state can be represented by a Bloch vector evolving on the Bloch sphere (see Figure 50). For a cyclic evolution, the tip of the state vector traces a closed loop on the sphere. The value of the AA phase is minus half of the solid angle enclosed by the loop:

$$\gamma \equiv -\frac{\Theta}{2} \quad \textbf{(257)}$$

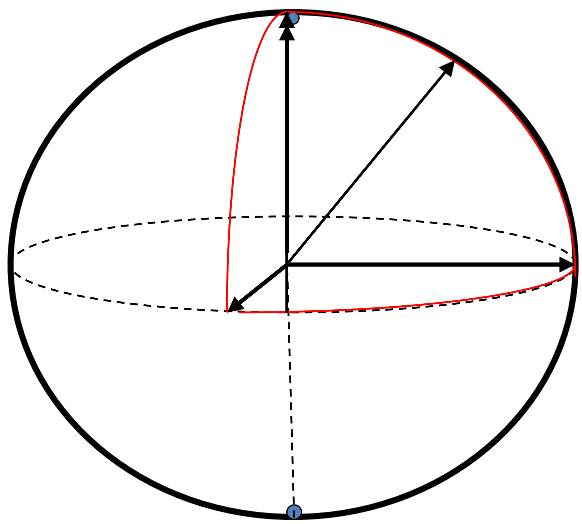

Figure 50- Bloch sphere with state vector |ψ> undergoing cyclic evolution (in red), making a solid angle Θ = ½ π.

In the example of Figure 50, the state vector is driven around a loop that subtends 1/8th the volume of the sphere. Since the solid angle of the entire sphere is 4π, the solid angle of this evolution is π/2. Therefore, the geometric phase is γ = -1/2 Θ = - π/4.

APPENDIX C- PUBLICATION ON GEOMETRIC GATES

PHYSICAL REVIEW A 84, 042335 (2011)

Robustness of single-qubit geometric gate against systematic error

J. T. Thomas, Mahmoud Lababidi, and Mingzhen Tian
School of Physics, Astronomy and Computational Sciences, George Mason University, Fairfax, Virginia 22030, USA
(Received 30 June 2010; revised manuscript received 4 August 2011; published 24 October 2011)

Universal single-qubit gates are constructed from a basic Bloch rotation operator realized through nonadiabatic Abelian geometric phase. The driving Hamiltonian in a generic two-level model is parameterized using controllable physical variables. The fidelity of the basic geometric rotation operator is investigated in the presence of systematic error in control parameters, such as the driving pulse area and frequency detuning. Compared to a conventional dynamic rotation, the geometric rotation shows improved fidelity.

DOI: 10.1103/PhysRevA.84.042335 PACS number(s): 03.67.Pp, 03.67.Lx, 03.65.Vf

I. INTRODUCTION

In the implementation of scalable quantum information processing, a key challenge is to achieve controlled quantum state preparation and manipulation with high fidelity in the presence of imperfections. In the commonly adapted quantum computing circuit model [1], this requires a set of robust universal quantum gates. Quantum gates degrade due to both imperfections in the control Hamiltonian and decoherence in the physical qubit system during the gate operation. When the operation time is kept much shorter than the qubit coherence time, the systematic error and random noise in the control Hamiltonian become the dominant causes for the operation error [2]. The quality of a quantum gate is usually characterized by gate fidelity or error rate per gate. A scalable computation can be achieved through quantum error correction [3], provided the error rate is smaller than a certain threshold, usually 10^{-4}, or a fidelity above 99.999% [2,4].

In recent years various all-geometric schemes based on quantum holonomy have been considered effective ways to minimize the operation errors caused by random noise. A control Hamiltonian is designed to drive a qubit along a specific path so that the resulting state transformation is affected only by the global geometry of the quantum system, not by the details of the evolution paths that are usually fluctuating due to noises in the control Hamiltonian [5–13]. The all-geometric approaches existing so far utilize either Abelian- or non-Abelian holonomy, which results in the state transformation expressed as a phase change or a unitary matrix, respectively. The non-Abelian geometric approach, usually called holonomic quantum computation [5], has been considered as a novel quantum computation model and proven fault tolerant under the adiabatic condition [14]. In the circuit model, holonomic quantum gates have been investigated for robustness against random parametric noise, most of them in adiabatic cases [15], which requires a long operation time. Breaking the adiabatic limit to shorten the operation time brings the quantum gates into no pure-geometric regimes [16]. Non-Abelian quantum gates have not been experimentally demonstrated mainly due to the difficulties in manipulation and measurement of multiple degenerate quantum states. On the other hand, the Abelian all-geometric approach is relatively simple since the gate operations are performed on nondegenerate two-level qubits through either Berry's phase [17] in an adiabatic evolution or Aharonov-Anandan (A-A) phase [18] in a nonadiabatic process. Abelian geometric gates have been proposed and demonstrated in almost all viable qubit systems so far, including [8–13] NMR, cold atoms or ions, photons, superconducting circuits, quantum dots, cavity QED, and atomic ensembles in solids. The fault tolerance against errors in the control Hamiltonian is still under investigation, and fidelity analysis has been focused on the effect of the random error [19–22]. The results, however, are still less conclusive for a general two-level system. In addition, the effects from seemingly simple systematic errors have not yet been addressed.

In this paper we focus on the robustness of a type of nonadiabatic Abelian geometric gates against systematic errors in the control parameters. Based on A-A phase, two noncommutable basic Bloch rotations were previously proposed and experimentally demonstrated, which can be used to compose any universal single-qubit gate [12]. The Hamiltonians controlling the rotations are made of a special type of composite pulses that drive the eigenvectors of the system through closed paths in the projective Hilbert space (a Bloch sphere), eliminating the dynamic phase. This paper generalizes the basic rotations as a rotation operator that suffices for making any single-qubit gates. Since the two-level qubit and the driving Hamiltonian are parameterized as a Bloch vector and a torque vector, respectively, evolving on the Bloch sphere this scheme is applicable to a generic two-level qubit. We are able to use the rotation operator to analyze the gate fidelity, which is independent of the qubit state. The fidelity is calculated in the presence of systematic errors in the control parameters, such as pulse area and frequency detuning. The geometric rotation is compared with conventional dynamic rotation. The link between the geometricity and high operation fidelity is discussed.

II. UNIVERSAL QUANTUM GATES AND BASIC BLOCH ROTATION

The quantum state of a qubit $|\psi\rangle = \cos\frac{\alpha}{2}|0\rangle + e^{i\beta}\sin\frac{\alpha}{2}|1\rangle$ can be represented by a Bloch vector $\vec{r} = (\sin\alpha\cos\beta, \sin\alpha\sin\beta, \cos\alpha)$ on the Bloch sphere as shown in Fig. 1(a). The polar angle α varies from 0 to π and the azimuthal angle β from 0 to 2π. A rotation on the Bloch sphere represents a universal quantum gate that can be expressed as

$$U_{\vec{n}}(\theta) = \exp(-i\vec{\sigma}\cdot\vec{n}\theta/2) = \cos(\theta/2)I - i\sin(\theta/2)\vec{\sigma}\cdot\vec{n}, \tag{1}$$

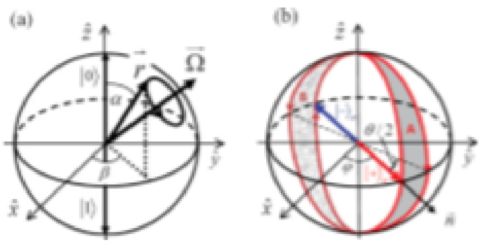

FIG. 1. (Color online) (a) Bloch vector $\vec{r}$ rotates around Rabi vector $\vec{\Omega}$ on the Bloch sphere. (b) Geometric paths A and B for basis vectors $|+\rangle_\varphi$ and $|-\rangle_\varphi$, respectively, to accomplish rotation $U(\theta,\varphi)$ in Eq. (2), where $\vec{n}$ is the rotation axis and θ the rotation angle.

where θ is the angle of rotation around axis $\vec{n}$, and I and $\vec{\sigma} = (\sigma_x,\sigma_y,\sigma_z)$ are the identity and Pauli matrices, respectively.

Since a rotation around an arbitrary axis can be made by rotations around two unparallel axes in the x-y plane, the problem of making a universal set of single-qubit gates reduces to making rotations around $\vec{n} = (\cos\varphi, \sin\varphi, 0)$ in the x-y plane, where φ is the angle between the x axis and the rotation axis $\vec{n}$. The rotation operator becomes

$$U(\theta,\varphi) = \cos(\theta/2)I - i\sin(\theta/2)(\cos\varphi\sigma_x + \sin\varphi\sigma_y), \quad (2)$$

where φ defines the rotation axis and θ the rotation angle. Any single-qubit gate can be made of at most three rotations characterized by such an operator with controllable φ and θ [23].

In a generic two-level model, the motion of the Bloch vector obeys the Bloch equation [24], $d\vec{r}/dt = \vec{\Omega} \times \vec{r}$, where the Bloch vector represents the quantum state and the driving Hamiltonian $H = (\hbar\Delta/2)\sigma_z + (\hbar\Omega_0/2)(\cos\varphi\sigma_x + \sin\varphi\sigma_y)$ in the rotating frame is parameterized by the torque given by the Rabi vector $\vec{\Omega}$. As shown in Fig. 1(a), the Bloch vector rotates around the driving torque by an angle of the pulse area $\theta = \Omega\tau$, where τ is the duration for a constant torque acting on the Bloch vector. The evolution of a two-level system, such as an atom or spin-1/2 particle, can be modeled as an effective dipole moment driven by an effective field near the resonance of the transition between the two energy levels of the qubit [24]. The driving field, $F(t) = \Omega_0\cos(\omega t + \phi)$, determines the Rabi vector to be $\Omega = (-\Omega_0\cos\phi, -\Omega_0\sin\phi, \Delta)$. The field amplitude Ω_0 is defined as Rabi frequency and takes into account the effective dipole moment; ϕ is the phase of the field; and Δ is the frequency detuning between the driving field and the resonance of the two-level system. These are the parameters that define the quantum gate operation and control the motion of the Bloch vector.

Conventionally, to make the rotation around an axis $\vec{n} = (\cos\varphi, \sin\varphi, 0)$ in the x-y plane as in Eq. (2), a pulse of an on-resonance field with constant amplitude Ω_0, phase $(\varphi + \pi)$, and duration τ is applied. A pulse with such parameters sets the Rabi vector $\Omega = (\Omega_0\cos\varphi, \Omega_0\sin\varphi, 0)$ along the desired rotation axis and the pulse area to the rotation angle $\theta = \Omega_0\tau$. The dynamic evolution driven by a simple pulse is ideal with 100% operation fidelity if the control parameters, including the Rabi frequency, phase, pulse length, and detuning, are perfect. However, when there is systematic error or random noise in the control parameters, this conventional simple pulse scheme may result in a high error rate and low fidelity.

III. SYSTEMATIC ERROR AND GATE FIDELITY

In the presence of error in the control parameters, an ideal operator U, such as in Eq. (2) turns into an imperfect operator V with erroneous rotation axis, angle, or both. Fidelity, usually used to evaluate the closeness of the two operators, is defined as [23,25,26]

$$F = |\mathrm{Tr}(VU^\dagger)|/2. \quad (3)$$

This allows us to study the fidelity of any quantum gate independent of the qubit state.

Systematic errors in the control parameters that affect the operation in Eq. (2) can be mainly categorized as pulse area error and frequency detuning error. The error in the pulse area $\theta = \Omega\tau$ is usually caused by inaccuracy in the Rabi frequency and the pulse duration. These result in an erroneous rotation angle. The detuning error due to the frequency difference between the driving pulse and the qubit resonance causes errors in the rotation axis and angle. Similar to the treatment for the composite pulse in NMR [27–29], we consider the pulse area and detuning errors separately.

The pulse area $\theta_\varepsilon = \theta(1+\varepsilon)$ with a percentage error ε corresponds to the operator $V(\theta,\varphi) = \exp(-i\vec{\sigma}\cdot\vec{n}\theta_\varepsilon/2)$. Using Eq. (3) the fidelity of such an operator is calculated to be

$$F_{ae} = \cos(\varepsilon\theta/2), \quad (4)$$

in which the fidelity degrades with the pulse area error and the rotation angle in the range of $[-\pi,\pi]$. The error affects a large rotation angle more than a small angle. The fidelity is uniform for all rotation axes at a given error level and rotation angle.

In most of the cases the percentage error in pulse area is expected to be small, where $|\varepsilon| \ll 1$ holds and the fidelity approximates to

$$F_{ae} \approx 1 - \frac{1}{2}\left(\frac{\theta}{2}\right)^2\varepsilon^2. \quad (5)$$

In the presence of the frequency detuning Δ, the Rabi frequency is generalized as $\Omega = \sqrt{\Omega_0^2 + \Delta^2} = \Omega_0\sqrt{1+f^2}$, where Ω_0 is on-resonance Rabi frequency and $f = \Delta/\Omega_0$ is the relative detuning with respect to Ω_0. The detuning affects both the rotation angle and the direction of the rotation axis. The ideal rotation angle θ turns into $\theta\sqrt{1+f^2}$ and the rotation axis $\vec{n} = (\cos\varphi, \sin\varphi, 0)$ shifts to $\vec{n}_f = (\frac{1}{\sqrt{1+f^2}}\cos\varphi, \frac{1}{\sqrt{1+f^2}}\sin\varphi, \frac{f}{\sqrt{1+f^2}})$. The rotation operator becomes

$$V(\theta,\varphi) = \cos\left(\frac{\theta\sqrt{1+f^2}}{2}\right)I - i\sin\left(\frac{\theta\sqrt{1+f^2}}{2}\right)\vec{\sigma}\cdot\vec{n}_f. \quad (6)$$

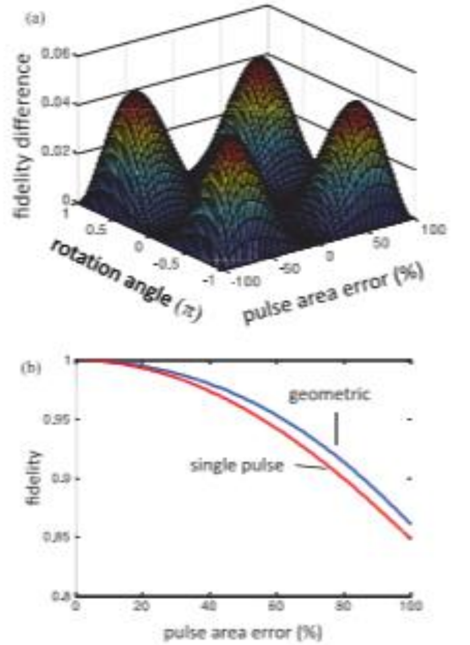

FIG. 2. (Color online) (a) Fidelity difference between geometric and simple pulse operators as a function of pulse area error and rotation angle. (b) Fidelities affected by pulse area error for geometric and simple pulse operators averaged over rotation angles from $-\pi$ to $-\pi$.

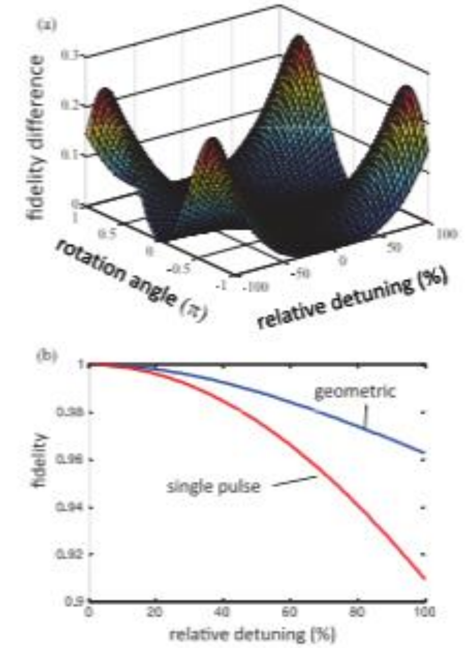

FIG. 3. (Color online) (a) Fidelity difference between geometric and simple pulse operators as a function of frequency detuning and rotation angle. (b) Fidelities affected by frequency detuning for geometric and simple pulse operators averaged over rotation angles from $-\pi$ to $-\pi$.

Under the condition $|f| << 1$, we compare the simple pulse operator in (8) and geometric operator in (15). For the rotation angle in the range of $0 < |\theta| < \pi$, $F_{gd} > F_{sd}$ holds true with the maximum fidelity $F_{gd} = F_{sd} = 1$ at $\theta = 0$, and the minimum fidelity $F_{gd} = F_{sd} = 1 - \frac{1}{2}f^2$ at $|\theta| = \pi$. The comparison of the two operators for large detuning range is presented in Fig. 3. The fidelity difference $F_{gd} - F_{sd}$ is plotted in Fig. 3(a). F_{gd} from Eq. (14) and F_{sd} from Eq. (7) averaged over all rotation angles are plotted in Fig. 3(b). The results show that the geometric operator holds equal or higher fidelity compared to the simple pulse operator against the frequency detuning for all rotation angles.

The geometric operator, however, is not entirely immune to the systematic errors in the pulse area and detuning: the fidelity decreases when an error increases. Two consequences of a system error are noncyclic paths for the eigenvectors and nonvanishing dynamic phases. For practical reasons we keep to the small error regime so that the evolution paths for the eigenvectors $|\pm\rangle_\varphi$ can still be approximated as closed loops. As a result, the degradation of the operation fidelity caused by the erroneous Hamiltonian should be attributed to the dynamic phase. We calculated the dynamic phase according to $\alpha_d = -\frac{1}{\hbar}\int \langle\chi(t)|H|\chi(t)\rangle_\varphi dt$, where $|\chi(t)\rangle_\varphi$ represents the states evolving from the initial state $|+\rangle_\varphi$ on path A shown in Fig. 1(b). Under small pulse area error, $|\varepsilon| \ll 1$, the dynamic phase was calculated to be

$$\alpha_{de} \approx \left(\frac{\pi}{2}\right)^2 \varepsilon \sin\frac{\theta}{2}\left(2 - \cos\frac{\theta}{2}\right). \tag{16}$$

This adds an extra angle $2|\alpha_{de\pm}|$ to the desired rotation. Comparing Eqs. (13) and (16) reveals the relationship between the fidelity degradation and the dynamic phase as,

$$F_{ge} = 1 - \frac{2}{\pi^2}\frac{1 - \cos\frac{\theta}{2}}{\left(1 + \cos\frac{\theta}{2}\right)\left[2 - \cos\frac{\theta}{2}\right]^2}\alpha_{de}^2. \tag{17}$$

The second term shows the fidelity decreases quadratically with the dynamic phase caused by the pulse area error. A fidelity of 100% is achieved for a pure geometric operator, corresponding to a vanishing dynamic phase.

The fidelity degradation caused by the detuning was studied in a similar way. Under small error approximation, we calculated the dynamic phase as a function of the detuning and the rotation angle as

$$\alpha_{df} \approx \frac{\pi}{2} f \left(\cos\frac{\theta}{2} - 1\right)^2. \tag{18}$$

Comparing the dynamic phase in (18) and the fidelity in (15), one can see the fidelity degradation is linked to the dynamic phase as

$$F_{gd} = 1 - \frac{2}{\pi^2}\frac{1}{\left(\cos\frac{\theta}{2} - 1\right)^2}\alpha_{df}^2, \tag{19}$$

which shows a similar relationship: the fidelity degrades quadratically with the dynamic phase caused by the frequency detuning.

While the rotation operator in Eq. (10) is all geometric under the ideal condition, systematic errors cause the eigenvectors to evolve on non-purely geometric paths. This is manifested as a nonvanishing dynamic phase. As a result, the operation fidelity decreases. This is consistent with the conclusion that the geometric path yields the highest fidelity.

V. CONCLUSION

A Bloch rotation operator based on nonadiabatic Abelian geometric phase has been designed and analyzed using a general model for a two-level qubit driven by a parameterized Hamiltonian. This operator is sufficient to make a set of universal single-qubit gates by setting the parameters such as pulse area, frequency, and phase of the effective control field. The fidelity of the geometric operator was analyzed against the systematic errors in the pulse area and the frequency detuning. An operator-based fidelity definition was used so that the results are independent of the qubit state. The geometric rotation operator was compared with the conventional simple pulse dynamic rotation. The systematic error degrades both types of operations with low fidelity at large rotation angle. The geometric operator shows overall improved fidelity over the simple pulse rotation. The reason for the degradation of the geometric operation is that the operator is no longer purely geometric when the systematic errors in both pulse area and frequency detuning cause the evolution path to deviate from the geometric path. As a result, the decrease in the fidelity is related to a nonvanishing dynamic phase. Further investigation is needed on the origin of the robustness of the geometric rotation against systematic errors compared with the dynamic operator.

Since our analysis is based on a generic nondegenerate two-level qubit model, the method and results in this paper are applicable to a variety of physical qubit systems, such as: NMR, atoms, ions, photons, superconducting circuits, and quantum dots. The model is suitable for both single-entity and ensemble qubits. When the inhomogeniety exists in the pulse area error or the frequency detuning in an ensemble, the fidelity calculation should be averaged over the entire ensemble. Geometric two-qubit gates, such as controlled-not and controlled-phase gates, can be analyzed in a similar way by introducing a qubit-qubit coupling term to the driving Hamiltonian.

While systematic control errors that can be parameterized into effective pulse area and frequency detuning errors exist in realistic systems, stochastic random fluctuation in the Hamiltonian is equally important. Both the dynamic and geometric operators discussed in this paper can be studied through numerical calculation of the fidelity according to Eq. (3), which is quite straightforward. However, the results will depend on the noise model, which could be quite different for the parameterized effective field in different physical systems and needs further investigation.

Our results on systematic errors are obtained for the simplest geometric path driven by an on-resonance effective field. More geometric paths can be designed by including off-resonance fields. For the practical purpose of achieving maximal gate fidelity, the path design should be optimized against both systematic and stochastic errors. The composition of the set of universal gates could play an important role as well in the optimization process.

ACKNOWLEDGMENTS

The authors gratefully acknowledge grant support from National Institute of Standards and Technology (Contract No. 70NANB7H6138, Am 001) and from the Office of Naval Research (Contract No. N00014-09-1-1025A). M.L. would like to thank Dr. Sophia Economou for fruitful discussions.

[1] D. Deutsch, Proc. R. Soc. London A 425, 73 (1989).
[2] E. Knill, Nature 434, 39 (2005).
[3] P. W. Shor, Phys. Rev. A 52, R2493 (1995); A. M. Steane, Phys. Rev. Lett. 77, 793 (1996).
[4] C. M. Dawson, H. L. Haselgrove, and M. A. Nielsen, Phys. Rev. Lett. 96, 020501 (2006); R. Li, M. Hoover, and F. Gaitan, Quant. Info. Camp. 9, 290 (2009).
[5] P. Zanardi and M. Rasetti, Phys. Lett. A 264, 94 (1999).
[6] A. Recati, T. Calarco, P. Zanardi, J. I. Cirac, and P. Zoller, Phys. Rev. A 66, 032309 (2002).
[7] J. Pachos and S. Chountasis, Phys. Rev. A 62, 052318 (2000).
[8] X.-B. Wang and M. Keiji, Phys. Rev. Lett. 87, 097901 (2001); J. A. Jones, V. Vedral, A. Ekert, and G. Castagnoli, Nature 398, 305 (2002); Y. Ota, Y. Goto, Y. Kondo, and A. M. Nakahara, Phys. Rev. A 80, 052311 (2009).
[9] L.-M. Duan, J. I. Cirac, and P. Zoller, Science 292, 1695 (2001); F. Schmidt-Kaler, H. Haffner, M. Riebe, S. Gulde, G. P. T. Lancaster, T. Deuschle, C. Becher, C. F. Roos, J. Escher, and R. Blatt, Nature 422, 408 (2003); D. Leibfried *et al.*, *ibid.* 422, 412 (2003).
[10] J. J. Garcia-Ripoll and J. I. Cirac, Philos. Trans. R. Soc. London A 361, 1537 (2003).
[11] G. Falci, R. Fazio, G. M. Palma, J. Siewert, and V. Vedral, Nature 407, 355 (2000).
[12] M. Tian, Z. W. Barber, J. A. Fischer, and W. R. Babbitt, Phys Rev. A 69, 050301(R) (2004); M. Tian, I. Zafarullah, T. Chang, R. K. Mohan, and W. R. Babbitt, *ibid.* 79, 022312 (2009).
[13] S. E. Economou and T. L. Reinecke, Phys. Rev. Lett. 99, 217401 (2007); S. Yin and D. M. Tong, Phys. Rev. A 79, 044303 (2009).
[14] O. Oreshkov, T. A. Brun, and D. A. Lidar, Phys. Rev. Lett. 102, 070502 (2009); O. Oreshkov, *ibid.* 103, 090502 (2009).
[15] G. De Chiara and G. M. Palma, Phys. Rev. Lett. 91, 090404 (2003); P. Solinas, P. Zanardi, and N. Zanghi, Phys. Rev. A 70, 042316 (2004); C. Lupo, P. Aniello, M. Napolitano, and G. Florio, *ibid.* 76, 012309 (2007).

[16] G. Florio, P. Facchi, R. Fazio V. Giovanetti, and S. Pascazio, Phys. Rev. A 73, 022327(2006).
[17] M. V. Berry, Proc. R. Soc. London A 392, 45 (1984).
[18] Y. Aharonov and J. Anandan, Phys. Rev. Lett. 58, 1593 (1987).
[19] A. Nazir, T. P. Spiller, and W. J. Munro, Phys. Rev. A 65, 042303 (2002).
[20] A. Blais and A. M. S. Tremblay, Phys. Rev. A 67, 012308 (2003).
[21] S-L Zhu and P. Zanardi, Phys. Rev. A 72, 020301(R) (2005).
[22] S. Fillipp, Eur. Phys. J. **160**, 165 (2008).
[23] M. A. Neilsen and I. L. Chuang, *Quantum Computation and Quantum Information* (Cambridge University Press, Cambridge, 2000).
[24] L. Allen and J. H. Eberly, *Optical Resonance, and Two-Level Atoms* (Dover Publications, Inc., New York, 1987).
[25] M. Nielsen, Phys. Lett. A 303, 249 (2002); C. M. Dawson, H. L. Haselgrove, and M. A. Nielsen, Phys. Rev. A 73, 052306 (2006).
[26] X. Wang, C-S. Yu, and X. X. Yi, Phys. Lett. A 373, 58 (2008).
[27] M. H. Levitt, Prog. NMR Spectrosc. 18, 61 (1986).
[28] R. Tycko, Phys. Rev. Lett. 51, 775 (1983).
[29] J. A. Jones, Philos. Trans. R. Soc. London A 361, 1429 (2003).
[30] E. Sjoqvist, Physics 1, 35 (2008).

REFERENCES

Abdumalikov, A. A. et. al. (2013). Experimental realization of non-Abelian non-adiabatic geometric gates. Nature 496, 482. http://arxiv.org/abs/1304.5186

Aharonov, Y and J.Anandan (1987). Phase change during a cyclic quantum evolution. Phys Rev Lett, v.58, n.16, p.1593.

Berger, S. et. al. (2013). Exploring the effect of noise on the Berry phase. Physical Review A 87, 060303(R). http://arxiv.org/abs/1302.3305

Berry, M.V.(1984). Quantal phase factors accompanying adiabatic changes. Proc R. Soc. Lond. A 392, 45-57, reprinted in *Geometric Phases in Physics*, ed. Shapere & Wilczek, p.124.

Blais, A. and A.M.S.Tremblay (2003). Effect of noise on geometric logic gates for quantum computation. Phys. Rev. A 67, 012308.

Carollo, A.C.M. and V.Vedral (2005). Holonomic quantum computation. http://arxiv.org/PS_cache/quant-ph/pdf/0504/0504205v1.pdf

Chiao, R Y and Wu Y S(1986). Phys. Rev. Lett. ,57, 93.

Duan, L.M., J.I. Cirac and P. Zoller (2001). Geometric manipulation of trapped ions for quantum computation. Science 292, 1695.

Ekert, A, M.Ericsson, P. Hayden, et. al.(2000). Geometric quantum computation. http://arxiv.org/PS_cache/quant-ph/pdf/0004/0004015v1.pdf

Falci, G, Fazio R, Palma G M, Siewert J and Vedral V (2000). Detection of geometric phase in superconducting nanocircuits. Nature, 407, 355.

Filipp, Stefan (2014). Exploring geometric phases and gates with superconducting quantum circuits. http://aip2014.org.au/cms/uploads/presentation/stefanfilipp.pdf

Jones, JA et al. (2000). Geometric quantum computation using nuclear magnetic resonance. Nature, 403, 869-871.

Kai-Yu, Y. et. al. (2003). Universal quantum gates based on both geometric and dynamic phases in quantum dots. Chinese Phys Lett, v20, no.7, 991.

Kloefel, Christoph and Daniel Loss (2012). Prospects for spin-based quantum computing. http://arxiv.org/pdf/1204.5917v1.pdf

Leek, P.J. et. al. (2007). Observation of Berry's phase in a solid-state qubit. Science, vol. 31, no. 5858, p. 1889.

Lemmer, A. et. al. (2013). Driven geometric phase gates with trapped ions. http://arxiv.org/abs/1303.5770

Li, XQ and LX Cen, et. al.(2003). Nonadiabatic geometric quantum computation with trapped ions. Phys Rev A, 66, 042320.

Manini, N (2009). Berry's geometric phase: a review. http://www.mi.infm.it/manini/berryphase.html

Mazonka, Oleg (2011). "Solid angle of conical surfaces, polyhedral cones, and intersecting spherical caps." http://arxiv.org/ftp/arxiv/papers/1205/1205.1396.pdf or http://arxiv.org/pdf/1205.1396v1.pdf

Mitskievich, N.V. and Nesterov, A.I. (2004). Geometric phase shift for detection of gravitational radiation.

Mostafazadeh, A(2000). Cosmological adiabatic geometric phase of a scalar field in a Bianchi spacetime. Turk.J.Phys,24, p.411.

Mukunda, N and R. Simon (1993). Quantum kinematic approach to the geometric phase: 1-General formalism. Annals of Physics, v.228, i.2, p.205-268.

Nielsen, M. A. and I.L.Chuang (2000). Quantum Computation and Quantum Information. Cambridge University Press, New York, NY.

Pachos, J and S.Chountasis(2000). Optical holonomic quantum computer. Phys Rev A, 62, 052318, (2000).

Pancharatnam, S (1956). Generalized theory of interference, and its applications. Part 1-Coherent pencils. The Proceedings of the Indian Academy of Sciences, vol. XLIV, no. 5, sec. A, p.247.

Pechal, M. et. al. (2012). Geometric phase and nonadiabatic effects in an electronic harmonic oscillator. Phys Rev Lett 108, 107401. http://arxiv.org/abs/1109.1157

Pei,P., FY Zhang, C Li, and HS Song (2010). Nonadiabatic geometric rotation of electron spin in a quantum dot by 2Pi hyberbolic secant pulses. J Phys B: At. Mol. Opt. Phys., 43, 125504.

Peng, Z. H. et.al.(2007). Implementation of adiabatic Abelian geometric gates with superconducting phase qubits. http://arxiv.org/PS_cache/quant-ph/pdf/0610/0610120v3.pdf

Prabhakar, Sanjay, Roderick Melnik and Akira Inomata(2014a).Geometric spin manipulation in semiconductor quantum dots.

Prabhakar, Sanjay, Roderick Melnik and Akira Inomata(2014b). Modeling and control of Berry phase in quantum dots. Proceedings 28th European Conference on Modeling and Simulation. http://www.scs-europe.net/dlib/2014/ecms14papers/eee_ECMS2014_0102.pdf

Puri, Shruti, Na Young Kim and Yoshihisa Yamamoto (2012). Two-qubit geometric phase gate for quantum dot spins using cavity polariton resonance. http://arxiv.org/ftp/arxiv/papers/1201/1201.3725.pdf

Quantum Device Lab at ETH Zurich (2014). http://www.qudev.ethz.ch/node/49618

Samuel, J. and R.Bhandari (1988). General setting for Berry's phase. Phys Rev Lett, v.60, n.23, p.2339.

Samuel, Joseph and Supurna Sinhi (1997). Thomas rotation and polarized light: A non-Abelian geometric phase in optics. Pramana, v.48, n5,p969. http://dspace.rri.res.in/bitstream/2289/1022/1/1997%20Pramana%20V48%20p969.pdf

Scully, Marlan O. and M. Suhail Zubairy (1997). Quantum Optics. Cambridge University Press.

Simon, B (1983). Holonomy, the quantum adiabatic theorem, and Berry's phase. Phys Rev Lett, 51, p.2167.

Simon, R, H.J.Kimble, and E.C.G. Sudarshan(1988). Evolving geometric phase and its dynamical manifestation as a frequency shift: an optical experiment. Phys. Rev. Lett., v61, n1.

Solina, P. et. al.(2003). Holonomic quantum gates: a semiconductor-based implementation. Phys Rev A 67, 062315.

Suter, D et.al (1987). Berry's phase in magnetic resonance. Mol. Phys.,61,p.1327, (1987).

Suter,D, KT Mueller, and A.Pines (1988). Study of the Aharonov-Anandan quantum phase in NMR interferometry. Phys Rev Lett, 60, p.1218.

Thomas, JT, Mahmoud Lababidi and Mingzhen Tian (2011). Robustness of single qubit geometric gate against systematic error. Physical Review A 84, 042335.

Thomson, Andrew (2005). 3-dimensional geometry: Solid angles and Girard's Theorem. http://www.math.ubc.ca/~cass/courses/m308/projects/thomson/Andrew_Thomson-Math_308-Final_Project.ps

Tian,M et. al.(2004). Geometric manipulation of the quantum states of two-level atoms. Phys Rev A 69, 050301.

Tomita, A. and R.Chiao (1986). Observation of Berry's topological phase by use of an optical fiber. Phys Rev Lett, 57,p.937.

Wang, ZS, C Wu, et. al.(200 7). Nonadiabatic geometric quantum computation. Phys Rev A, 76, 044303.

Zhu, S.L. and Z.D.Wang (2003). Unconventional geometric quantum computation. Phys Rev Lett. 91, 187902.

Zhu, Shi-Liang and Paolo Zanardi(2005). Geometric quantum gates that are robust against stochastic control errors. Phys Rev A 72, 020301R.

Zu, C. et. al. (2014). Experimental realization of universal geometric quantum gates with solid-state spins. Nature 514, 72 and http://arxiv.org/pdf/1411.3157v1.pdf

CURRICULUM VITAE

JT Thomas, of Michigan and Ohio, received a Bachelor of Science in Physics from University of Maryland, College Park, Maryland and a Master of Science in Applied Physics and Engineering from George Mason University. JT recently wrote the winning proposal and was the Principal Investigator on a gravitational wave detector and generator contract, DARPA #ST13A-003.

Publication:

Thomas, JT, Mahmoud Lababidi and Mingzhen Tian (2011). Robustness of single qubit geometric gate against systematic error. Physical Review A 84, 042335.